

Scientific Report No. 27-2008

Validation of MSU Tropospheric and Stratospheric Temperature Records with GPS Radio Occultation Climatologies

Thomas Schöngaßner

November 2008

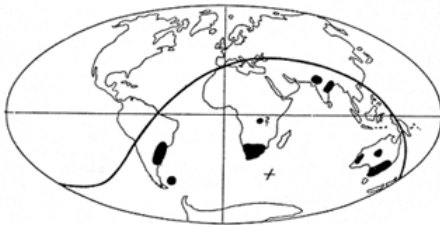


Wegener Center
www.wegcenter.at



The **Wegener Center for Climate and Global Change** combines as an interdisciplinary, internationally oriented research center the competences of the University of Graz in the research area „Climate, Environmental and Global Change“. It brings together, in a dedicated building close to the University central campus, research teams and scientists from fields such as geo- and climate physics, meteorology, economics, geography, and regional sciences. At the same time close links exist and are further developed with many cooperation partners, both nationally and internationally. The research interests extend from monitoring, analysis, modeling and prediction of climate and environmental change via climate impact research to the analysis of the human dimensions of these changes, i.e., the role of humans in causing and being effected by climate and environmental change as well as in adaptation and mitigation. The director of the center, hosting about 35 researchers, is the geophysicist Gottfried Kirchengast, the lead partner and deputy director is the economist Karl Steininger. (more information at www.wegcenter.at)

The present report is the result of a M.Sc. thesis work completed in July 2008.



Alfred Wegener (1880-1930), after whom the Wegener Center is named, was founding holder of the University of Graz Geophysics Chair (1924-1930) and was in his work in the fields of geophysics, meteorology, and climatology a brilliant, interdisciplinary thinking and acting scientist and scholar, far ahead of his time with this style. The way of his ground-breaking research on continental drift is a shining role model — his sketch on the relationship of the continents based on traces of an ice age about 300 million years ago (left) as basis for the Wegener Center Logo is thus a continuous encouragement to explore equally innovative scientific ways: *ways emerge in that we go them* (Motto of the Wegener Center).

Wegener Center Verlag • Graz, Austria

© 2008 All Rights Reserved.

Selected use of individual figures, tables or parts of text is permitted for non-commercial purposes, provided this report is correctly and clearly cited as the source. Publisher contact for any interests beyond such use: wegcenter@uni-graz.at.

ISBN 978-3-9502615-5-4

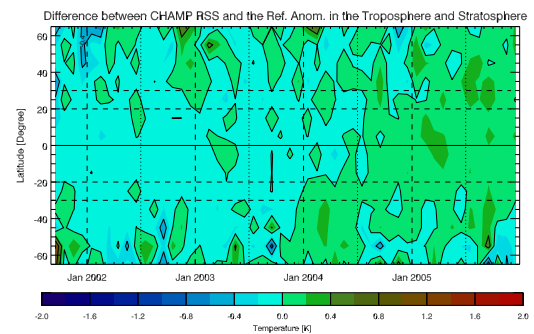
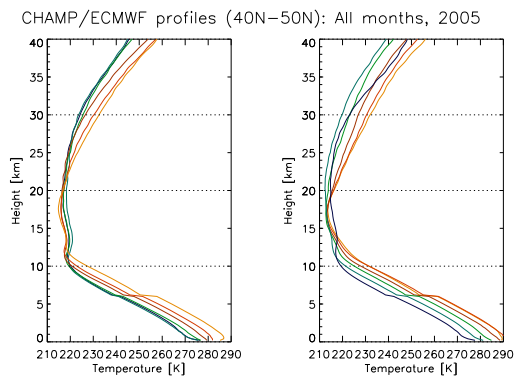
November 2008

Contact: *Thomas Schöngaßner, M.Sc.*
thomas.sch@gmx.at

Wegener Center for Climate and Global Change
University of Graz
Leechgasse 25
A-8010 Graz, Austria
www.wegcenter.at

Validation of MSU tropospheric and stratospheric temperature records with GPS radio occultation climatologies

Thomas Schöngaßner



Diplomarbeit

zur Erlangung des akademischen Grades eines
Magisters der Naturwissenschaften
an der Naturwissenschaftlichen Fakultät
der Karl-Franzens-Universität Graz

Betreuer:

Univ-Prof. Dr. Gottfried Kirchengast

Mitbetreuerin:

Dr. Andrea Steiner

Wegener Zentrum für Klima und Globalen Wandel und
Institutsbereich Geophysik, Astrophysik und Meteorologie, Institut für Physik
Karl-Franzens-Universität Graz

Acknowledgments

Here I would like to thank all people, who have helped me during my study with either personal assistance or financial support. Without that it would have been hard to manage the study in that way.

My biggest thank is directed to my family, especially my parents. They have primarily financed my study and have always supported me with their confidence and trust that I can carry out and finish my study. Also my grandmother is thanked for her financial support. I also want to thank my brothers and all my friends. They have helped me out when I had problems with my computer or questions related to my study and to other topics. They advised me whenever I had personal worries and made it possible for me to gain experience beside the study and to have nice hours.

Furthermore I thank Univ.-Prof. Dr. Gottfried Kirchengast very much, that I could write the diploma thesis at the Institute for Geophysics, Astrophysics, and Meteorology and at the Wegener Center in Graz. He advised me in many questions related to the topic of my work. I also thank Dr. Andrea Steiner for her personal support to improve my results and outputs from start to end. She also checked my thesis for format style deficiencies and expression shortcomings. Additionally, I thank all my colleagues of the Wegener Center and especially those of the ARSCliSys research group for the good working atmosphere. They always helped me out when I had scientific questions or problems with the data or the programs. At this point I want to mention Dr. Michael Borsche for his untiring support to create a fully functional and well working Latex file and regarding the format and the design of my thesis. Mag. Susanne Schweitzer helped me out whenever I had questions about the topic. I also thank her very much for proof reading my thesis. An important part of my thesis is based on the heritage of the Ph.D. thesis of Dr. Andreas Gobiet. Therefore I thank him that I could use his work for describing the radio occultation measurement procedure.

Finally, I want to thank all data providers. Thanks are directed at the MSU processing centers, the University of Alabama, Huntsville, USA (UAH) and the Remote Sensing System, Santa Rosa, USA (RSS). They provided their retrieved MSU time series and weighting functions for public use in the web. Many thanks are also directed at the GeoForschungsZentrum (GFZ) Potsdam, which is responsible for the CHAMP radio occultation measurements. Also the European Centre for Medium-Range Weather Forecasts (ECMWF) is thanked for their analysis data and the Wegener Center, Graz, is thanked for the radio occultation climatologies.

Abstract

Although surface temperature measurements showed a trend of $+0.17\text{ K/decade}$ between 1979 and 2005, the climate warming has long been discussed. The problem was the difference in temperature trend results between the free atmosphere and the surface.

Since 1979 weather satellites are applied to observe the atmosphere providing global homogeneously distributed temperature, pressure, and humidity measurements of several atmospheric layers. The NOAA polar orbiting satellites carry (Advanced) Microwave Sounding Units (MSU/AMSU), which measure the Earth's radiation at several frequencies using the oxygen emission line around 60 GHz. The pressure layer at which bulk temperatures are observed depends on the respective frequency channel. But the calibration of the instruments is not error-free, biases like diurnal drift had to be corrected, and measurement series of different satellites needed to be merged together to climate records. Therefore different trends resulted from different retrieval schemes, depending on the processing center. In this context MSU is compared to Radio Occultation (RO) observations. The RO technique is applied since a couple of years and uses radiowaves which are transferred by a GPS satellite to a low Earth orbiter. The radiowaves are refracted in the atmosphere. From the measured phase delays profiles related to the bending angle, refractivity, pressure, and dry temperature are retrieved. The main advantages in contrast to MSU are the high vertical resolution and high data quality. The calibration is long-term stable and independent of receiver type and instrument due to precise time measurements with atomic clocks. But in the lower and mid troposphere limitations arise because of the moist-dry ambiguity inherent in refractivity. This can only be resolved with background information.

In this validation study, we used RO climatologies of dry temperature, which were replaced with ECMWF (European Centre for Medium-Range Weather Forecasts) analysis data in moist tropospheric regions. Global weighting functions were applied to compute synthetic MSU temperatures for CHAMP-RO. The monthly mean zonal mean climatologies were compared to the MSU measurement series in terms of absolute temperatures and temperature anomalies for the period September 2001 to December 2005.

The measured brightness temperatures agree quite well in the lower stratosphere, where the temperature ranges between 198 K and 227 K. On global average, the RO measurements are about 0.4-0.8 K warmer than the MSU ones in the annual cycle. The difference raises up to 3 K in the troposphere-stratosphere (TTS) and up to 1.0-1.2 K in the mid troposphere (TMT). The brightness temperature ranges between 211 K and 230 K for TTS and between 234 K and 258 K for TMT. Interesting is that the anomaly differences are not constant and change over time from 2001 to 2005. RO shows, e.g., slightly colder TTS anomalies than MSU in the beginning and warmer ones at the end of the observation period.

Zusammenfassung

Obwohl Bodenbeobachtungen einen Temperaturtrend von $+0.17$ K/Dekade zwischen 1979 und 2005 ergaben, lösten die unterschiedlichen Messergebnisse in der freien Atmosphäre relativ zum Boden eine Debatte über den Klimawandel an sich aus. Seit 1979 sorgen Wetter-satelliten für global homogen verteilte Messungen von Temperatur, Druck und Feuchtigkeit in verschiedenen atmosphärischen Schichten. Dabei werden unter anderem NOAA Satel-liten verwendet, welche mit einem (ausgereiften) Mikrowellendetektor (MSU/AMSU) aus-gestattet sind und die terrestrische Mikrowellenausstrahlung an mehreren Frequenzen um die Emissionslinie vom Sauerstoff (60 GHz) messen. Das Druckniveau der beobachteten Temperatur hängt hierbei vom Frequenzkanal ab. Allerdings ist die Kalibrierungsmethode nicht fehlerfrei. Weiters müssen Unsicherheiten wie die Tageszeitdrift korrigiert und die Messreihen der einzelnen Satelliten zu einer Temperaturzeitreihe zusammengesetzt werden. Dabei resultierten je nach Herleitungsmethode unterschiedliche Ergebnisse.

Im Vergleich dazu wird die Radio Okkultations (RO) Technik erst seit einigen Jahren angewendet. Sie basiert auf Radiowellen, welche von einem GPS Satelliten gesendet und von einem zweiten Satelliten empfangen werden. Die Radiowellen werden von der dazwis-chen liegenden Atmosphäre gebrochen. Von der gemessenen Phasenverschiebung wer-den dann Profile von Brechungswinkel, Refraktivität, Druck und Trockenlufttemperatur berechnet. Die Vorteile gegenüber MSU liegen in der hohen vertikalen Auflösung und in der hohen Qualität der Daten. Die Kalibrierung beruht auf präzisen Zeitmessungen mit Atomuhren und ist daher nicht vom Empfängertyp und Instrument abhängig. Allerdings ergeben sich in der unteren bzw. mittleren Troposphäre Einschränkungen aufgrund des hohen Wasserdampfgehaltes, weshalb dort auf andere Quellen zurückgegriffen wird.

In dieser Vergleichsstudie wurden die betreffenden Temperaturen mit Analysedaten des ECMWF (Europäisches Zentrum für Mittelfristige Wettervorhersagen) ersetzt. Um MSU-synthetische Temperaturzeitreihen zu erhalten, wurden die GPS-RO Profile mit globalen Gewichtungsfunktionen gewichtet und anschließend die zonalen Monatsmitteltemperaturen von MSU und RO für die Periode September 2001 - Dezember 2005 miteinander verglichen. Im Wesentlichen zeigen MSU und RO ähnliche Temperaturen in der unteren Stratosphäre (198-227 K). Im globalen Durchschnitt sind die RO Messungen im Jahrgang um etwa 0.4-0.8 K wärmer als die von MSU. Die Differenz erhöht sich in der oberen Troposphäre (TTS) auf 3 K und in der mittleren Troposphäre (TMT) auf 1.0-1.2 K. Die Temperaturen bewegen sich zwischen 211 K und 230 K (TTS) und zwischen 234 K und 258 K (TMT). Er-wähnenswert ist, dass die Differenz zwischen den MSU und RO Anomalien nicht konstant ist und sich mit der Zeit ändert. RO zeigt beispielsweise leicht kältere TTS Anomalien als MSU am Anfang und wärmere am Ende des Beobachtungszeitraumes.

Contents

1	Introduction	1
2	The Climate System	3
2.1	The Energy Balance	4
2.2	The Components	7
2.2.1	Atmosphere	7
2.2.2	Hydrosphere	11
2.2.3	Cryosphere	12
2.2.4	Lithosphere	12
2.2.5	Biosphere	13
2.3	Climate Variability	13
2.3.1	Anthropogenic Climate Change	16
2.4	Climate Monitoring	18
3	Microwave Emission Measurements	23
3.1	Physical Concept	23
3.1.1	Microwave Sounding of the Atmosphere	23
3.1.2	The Microwave Absorption Spectrum	25
3.1.3	Line Broadening	25
3.1.4	Derivation of the Weighting Functions	26
3.2	First Satellite-based Observations	28
3.3	Temperature Retrieval	31
3.4	Merging Procedure and Data Quality	33
3.5	Trend Results and Discussion	36
3.5.1	Received Temperature Trends	36
3.5.2	Stratospheric Influence on TMT	37
3.5.3	Diurnal Drift Correction	40
3.6	RSS Temperature Retrieval	41
4	Radio Occultation Measurements	43
4.1	Development of this Technology	43
4.2	Signals, Constellation and Resolution	45
4.3	Data Processing	47
4.3.1	Data Acquisition	48
4.4	Physical Concept	49

Contents

4.5	Temperature and Pressure Profiles	52
4.5.1	The Optical Path	52
4.5.2	Bending Angle	54
4.5.3	Refractivity	57
4.5.4	Temperature and Pressure	58
4.5.5	Ambiguous Water Vapor Signal	59
4.6	Benefits from RO Observations	60
5	Validation Process	63
5.1	Problem Formulation	63
5.2	Description of the Data Sets	63
5.2.1	Radio Occultation Data	63
5.2.2	Microwave Sounding Unit Data and Weighting Functions	67
5.3	Calculation of MSU Equivalent Temperatures	70
5.4	Regridding of MSU Data	75
5.5	Calculation of Temperature Average and Anomalies	76
6	Results and Discussion	79
6.1	Brightness Temperature	79
6.2	Monthly Mean Reference Temperatures	87
6.2.1	Comparison between the MSU Means	88
6.2.2	Comparison between CHAMP and MSU	91
6.3	Comparison of Temperature Anomalies	98
7	Summary and Conclusions	109
	List of Symbols	113
	List of Abbreviations	115
	List of Figures	117
	List of Tables	119
	Bibliography	121

1 Introduction

This thesis considers the climate system and the changes of the past twenty years. Of prime interest will be two methods of space based temperature observations of the atmosphere. The first one exploits the radiation output of the Earth, which increases with temperature. The second one exploits refraction of electromagnetic radiation by molecules. Both principles relate to temperature and many other atmospheric properties. Here, I will give a short overview on these methods, and compare and validate the temperature measurements between 2001 and 2005. The focus lies on the discrepancies between the results, the absolute differences, and on first interpretations of them.

The motivation arises from the observed surface warming and environmental changes, which have caused a big discussion about the climate state. People became worried about the glaciers which melt with a high velocity, and about the increasing frequency of extreme weather events like droughts, floods, and severe storms. Some measurements have already confirmed those observations. 11 of the 12 warmest years since 1000 AD have occurred after 1995. Southern Europe for instance has experienced hot and extremely dry summers, which have triggered serious droughts and wood fires.

Is our climate changing and if yes, what does drive it? Is this only a warm phase of the natural climate variability? In the last million years the global surface temperature has varied by more than four degrees on global and hemispherical scales. Sometimes the changes occurred with a quite high amplitude within a few decades. 5000 years ago it was about 1-2°C warmer than nowadays. Trees could grow in regions, which are nowadays covered by glaciers and the inner tropical convergence zone may have extended much further into the north during summer (vegetation in the Sahara).

Probably we experience an unusual climate change, as it has already occurred several times after gigantic volcano eruptions, cosmic meteorite impacts, and after sudden shifts of the thermohaline ocean streams? The difference to those is that the actual climate change is not natural. It is very likely that it was triggered by the observed increase of the anthropogenic greenhouse gas concentrations [Solomon *et al.*, 2007]. Here I give some statements of the IPCC WGI Fourth Assessment Report [2007] of the main changes.

"Eleven of the last twelve years (1995-2006) rank among the 12 warmest years in the instrumental record of global surface temperature (since 1850). The updated 100-year linear trend for 1906-2005 (0.74 ± 0.16 °C) is therefore larger than the corresponding trend for 1901-2000 given in the TAR of (0.6 ± 0.2 °C)." The earlier trend was received from the IPCC Third Assessment Report [TAR, 2001].

1 Introduction

"Carbon dioxide is the most important anthropogenic greenhouse gas. The global atmospheric concentration of CO₂ has increased from a preindustrial value of 280 ppm to 379 ppm in 2005. The atmospheric concentration of carbon dioxide exceeds by far the natural range over the last 650000 years (180 ppm - 300 ppm) as determined from ice cores...." [Solomon et al., 2007].

In the first chapter, I try to describe the climate components, the forces, which drive the terrestrial climate system, and some changes, which have occurred in the past centuries. The following two chapters give a short introduction into space based microwave and radio occultation observations, their physical concepts and uncertainties. Chapter 5 gives a description of the investigated data sets and explains the procedure applied to compare them. The results are presented and discussed then in chapter 6.

"Global average sea level in the last interglacial period (about 125000 years ago) was likely 4 to 6 m higher than during the 20th century, mainly due to the retreat of polar ice. Ice core data indicate that average polar temperatures at that time were 3-5 K higher than present, because of differences in the Earth's orbit" [Solomon et al., 2007].

The focus lies on the observed temperature and pressure observations between September 2001 and December 2005. The differences between the results will be discussed in terms of global, hemispheric and zonal scales, which may give some information about accuracy and uncertainty of the remote sensing techniques. It is important to get familiar with the actual climate state and the environmental changes, which arise due to shifts of e.g., temperature and precipitation on spatial and temporal scales. Humans need to supply themselves with enough food, water and energy. Since the population has increased to a maximum absorption of the agricultural productivity, a climate drift might cause serious risks for life, environment and productivity. Therefore it is important to provide observations of the climate elements like temperature, pressure, water vapor pressure, and wind speed with maximum precision. This may give necessary information about trends and developments in the climate system.

2 The Climate System

A specific climate arises from a homogeneous sequence of weather events, while each of them are described by a manifestation of single climate elements. Climate elements are measurable quantities like temperature, pressure and precipitation. Their variability, average, and other statistical properties (e.g. frequency of extreme values) over a longer time period define a climate [Hartmann, 1994]. The area, on which a statistical analysis is carried out, depends on the purpose. It might be a single valley, a continent or even the total globe. The corresponding time period extends from a single day to several decades or centuries. In this thesis, e.g., I investigate temperature records of the troposphere and stratosphere between 2001 and 2005 on a hemispheric and global scale. This in fact gives only a rough insight into the atmospheric climate system.

Generally temperature decreases from the tropics toward the poles, while precipitation increases from drought deserts to humid rain forests and from the interior of continents toward the coasts. Winds develop due to pressure gradients and transport air masses and clouds from one place to another. They mix air masses and are responsible for the special

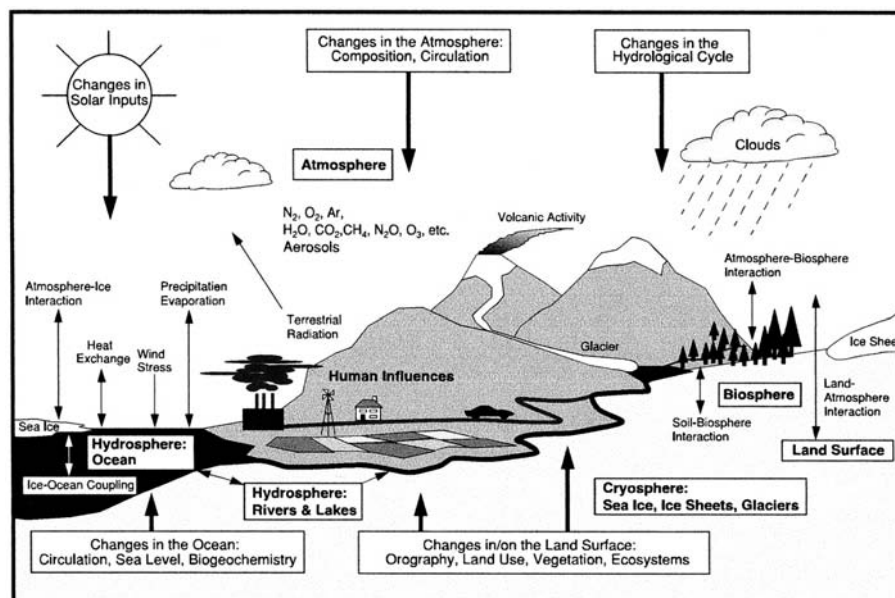


Figure 2.1: This figure shows the Earth's climate system with the components (bold), the interactions (thin arrows) and some internal and external forces (bold arrows) [Baede *et al.*, 2001].

2 The Climate System

temperature and precipitation pattern of the Earth. Another climate element, the relative humidity, results from temperature and water vapor pressure. It is a measure for the probability of cloud and fog formation, which develop in supersaturated air masses. That in turn is very important for the radiation balance because clouds reflect solar radiation in high altitudes, where they mainly consist of ice crystals. Lower parts absorb terrestrial radiation. Also important for the climate are snow, ice, and vegetation because they influence the albedo (i.e., reflectivity) of the Earth [Hartmann, 1994].

The combination of these climate elements defines a specific climate zone, which changes with latitude and longitude. A climate variation is the natural dynamic behavior of the elements on all spatial and temporal scales. Single weather events are not relevant, since a climate results from the combination of all events. But such a sample may show a significant statistical trend (e.g., a positive temperature trend over several decades). This is defined as a climate change or drift, which in turn occurs on a larger time scale than the climate variability, and is induced by internal and external forces, which are described below and visualized in Figure 2.1. The climate variability describes continuous changes on all spatial and temporal scales beyond that of individual weather events.

The sun is actually the main driver of weather events and ocean currents. Without it, the Earth would freeze down to space temperatures. Therefore, at first I discuss the energy balance of the Earth, then the components of the climate system, afterward the variability of the climate system and finally the observed temperature drifts and environmental changes.

2.1 The Energy Balance

This section consists primary of information from the textbook of *Hartmann* [1994, pp. 20]. To build up an energy balance of an object, it is important to consider all the inputs and outputs. Generally heat and energy can be conducted, convected, and radiated.

1. *Conduction*: Molecules transfer heat during collisions with other molecules. Thereby, energy is conducted from one point of a substance to another one.
2. *Convection*: Convection can only occur within fluid and gaseous materials, because they mix with each other and transport energy over large distances.
3. *Radiation*: Contrary to conduction and convection, radiation is a sample of electromagnetic waves which are normally distributed over the total spectrum and transport heat also through vacuum space. Intensity and frequency are proportional to the surface temperature of a black body, which is a closed cave in a thermodynamic equilibrium. The black body radiation is described with the Stefan-Boltzmann law $E = \sigma T_e^4$, where E is the energy output and T_e the emission temperature.

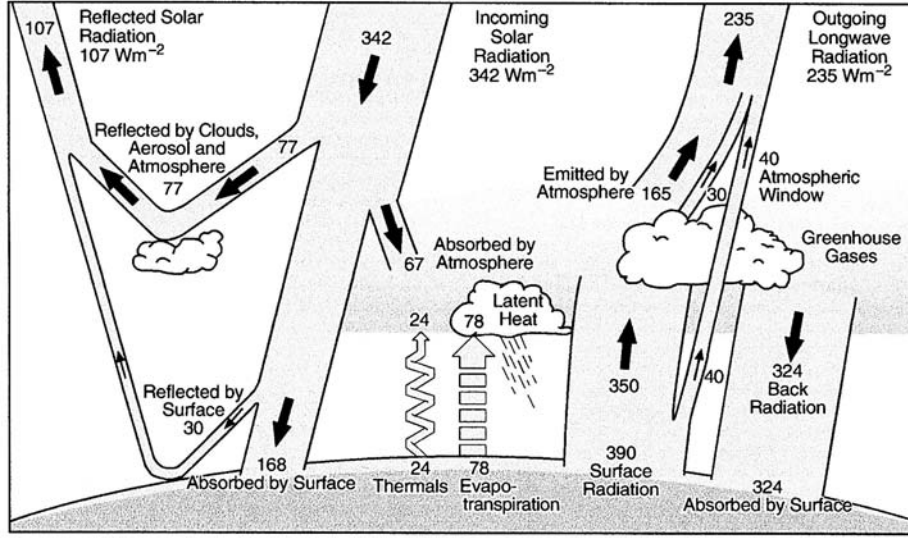


Figure 2.2: Earth’s annual global mean energy balance in Wm^{-2} [Kiehl and Trenberth, 1997].

The sun can be treated as a black body. It is Earth’s primary energy source and predominates over all other ones¹. Since conduction and convection work only within matter, the solar energy is only received by radiation (therefore the energy balance is also called the radiation balance). The sun produces energy of $3.9 \times 10^{26} \text{ W}$ due to nuclear fusion of hydrogen to helium in its core. The Energy decreases with the square of the distance and produces a surface temperature of 6000 K at the solar surface. The magnitude of received radiation depends on the astronomical distance to a star, on the eccentricity² of the orbit of the planet and on the obliquity³. They define the magnitude and the seasonal variability of the solar insolation. To achieve a thermal equilibrium the absorbed solar radiation must equal the planetary emission. The emitted energy increases with the fourth power of the emission temperature T_e , which is described by the Stefan-Boltzmann Law. At the top of the atmosphere the Earth receives 1367 W/m^2 , which is known as the solar constant S_0 (Figure 2.2). The incoming radiation is distributed on a circular shape ($r^2\pi$), where r is the Earth’s radius. Generally the radiation balance is established in the tropopause, because the stratosphere above adjusts radiation imbalances much faster than the troposphere below [Gobiet, 2005]. Since Earth consists of different materials (water, vegetation, ice, rock, and clouds) radiation is absorbed and reflected in various proportions. The average terrestrial reflection is about 31 %, which is called the planetary albedo α_p .

$$\underbrace{\pi r^2 S_0 (1 - \alpha_p)}_{\text{absorbed energy}} = \underbrace{4\pi r^2 \sigma T_e^4}_{\text{emitted radiation}} \quad (2.1)$$

¹Other energy sources are conducted heat from the interior, backscattered sunlight, and radiation from other stars.

²Measure for the departure from a perfect circular orbit.

³Maximum angle between the rotation axes and the normal of the planetary plane 23.45° .

2 The Climate System

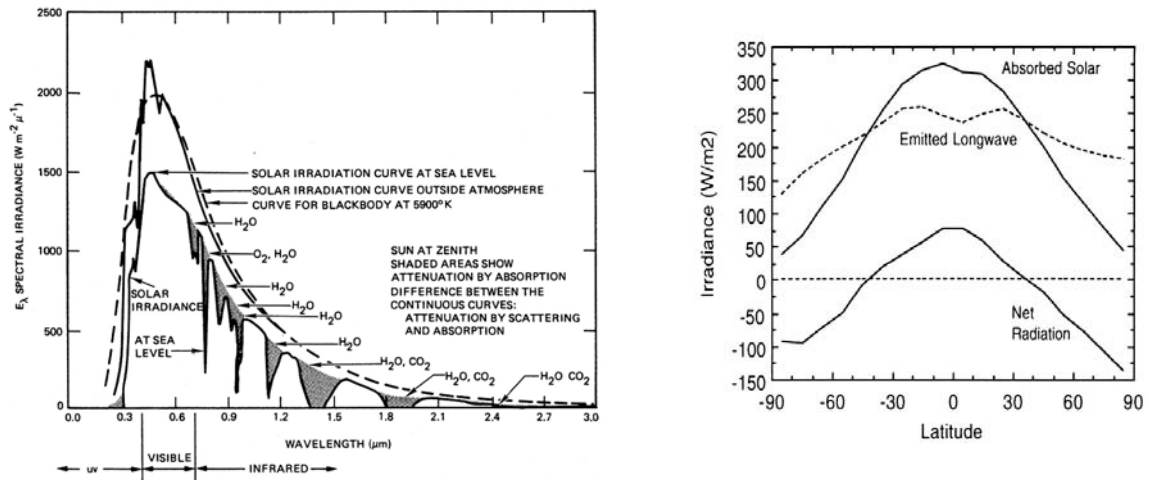


Figure 2.3: The left figure shows the received solar energy as a function of frequency at the top of the atmosphere and at sea level. Furthermore it shows the discrepancy between black body and actual solar radiation [Chahine, 1983]. The Earth's radiation balance as a function of latitude at the top of the atmosphere is plotted on the right side [Hartmann, 1994].

This gives an emission temperature of 255 K at the top of the atmosphere, which is much lower than the actual global average of 288 K⁴. Responsible for that are the well known greenhouse gases. These are air molecules with three atoms. They develop a permanent or temporal dipole moment, absorb infrared radiation, which is transformed in rotational and vibrational energy, and reemit it back in all directions. CO₂ for instance is spherically symmetric and develops a dipole moment only during vibrations. Greenhouse gases have dominant rotational and vibration-rotational absorption lines close to the frequency of the Earth's maximum radiation output at 11 μm⁵ in the infrared spectrum. H₂O has a broad vibration-rotation band near 6.3 μm and a densely spaced strong rotation line at about 12 μm, CO₂ produces a strong vibration-rotation band near 15 μm and O₃ one at 9.6 μm, as pictured in Figure 2.4.

The warming effect, which arises due to absorption of terrestrial long-wave radiation in the atmosphere, is known as the natural greenhouse effect. Water vapor plays the most dominant role here.

The greenhouse gases are responsible for the most part of the heat exchange at the surface. As shown in Figure 2.2, it receives 324 W/m² of 492 W/m² from the atmosphere. Clouds, aerosols, and greenhouse gases reflect the outgoing terrestrial radiation. Aerosols are liquid or solid particles, stemming from biological, chemical and mechanical processes. Their impact depends on the shape, size and specific albedo. The influence of clouds primary depends on the altitudes of them. In sum they have a net cooling effect [Baede et al., 2001, pp. 90].

⁴The average value since about 1850

⁵This value results from the Wien's displacement law, which gives the wavelength λ at which the maximum energy is emitted $\lambda = 0.002898 \text{ mK}/T_e$

High clouds, especially if they contain ice crystals, reflect much of the sunlight, while the cloud droplets in lower layers absorb and reemit long-wave radiation. Clouds are responsible for the biggest part of Earth's reflectivity. Only one quarter is contributed by the surface, which shows a net radiation win of 102 W/m^2 . This net radiation is primarily convected upward either as sensible or as latent heat (Figure 2.2). Water evaporates at the surface and releases heat in higher altitudes, if it condenses to cloud droplets.

Therefore the troposphere receives over five times more energy from the surface than from the sun. This is obviously due to the greenhouse gases and the clouds. A similar behavior develops in the stratosphere due to the ozone layer, which raises the equilibrium temperature and decreases the lapse rate (Figure 2.5). Generally, at the top of the atmosphere the terrestrial radiation peaks in the subtropical regions at about 25°N/S and decreases toward the equator due to the convective cloud cover. The insulation mainly depends on the zenith-angle⁶, which increases with latitude due to the elliptical shape of the Earth. But the albedo increases as well and causes a net radiation loss poleward of 35°N and 45°S respectively, as visible in Figure 2.3. This has to do with the more frequent cloud and snow cover on the one hand and the bright arid regions, on the other hand. Furthermore, the reflectivity of sea-water raises with increasing zenith-angles. Therefore the tropical oceans, where clouds are rare as well, provide the lowest albedo.

The net radiation in the southern high latitudes is higher than in the northern ones due to the large difference between the emitted terrestrial radiation. The Antarctica is covered by km-thick glaciers in comparison to the partly ice-free Arctic Ocean, which results in different surface temperature and emission properties.

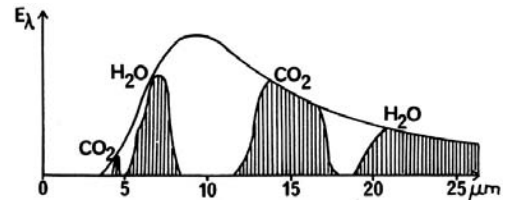


Figure 2.4: Atmospheric absorption in the longwave spectrum, around the Earth's maximum radiation output [Malberg, 1997].

2.2 The Components

2.2.1 Atmosphere

The atmosphere plays a fundamental role in the climate system because it is responsible for the amount of radiation which can pass and exit. 99% of the atmospheric mass are concentrated in the lowest 30 km above the surface. In comparison to the rest of the Earth this is relative small but nevertheless fundamental for life. The atmosphere prevents the creatures from harmful ultraviolet radiation, increases the mean surface temperature above the melting point of water and damps the diurnal temperature variability. Generally, the

⁶Angle between the vertical axis and the incoming radiation

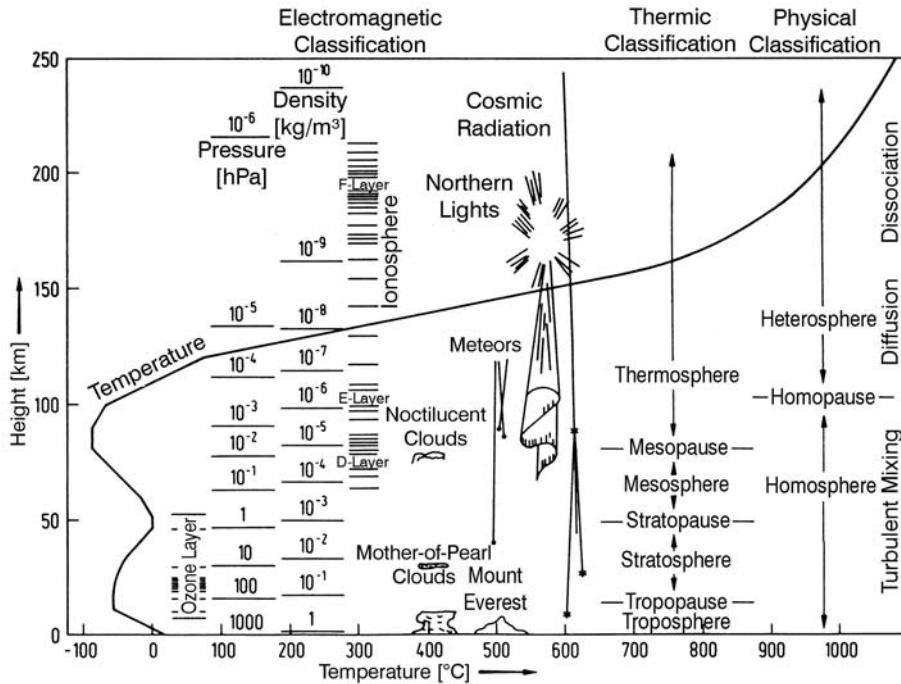


Figure 2.5: The vertical structure of the terrestrial atmosphere, considering temperature, pressure and density. Furthermore the name of the layers and their physical processes are shown [Liljequist and Cehak, 1984].

atmosphere is divided into several layers, which are characterized by specific temperature, pressure and stability properties. Due to small variations in the composition, the lapse rate changes the sign several times, as visible in Figure 2.5. Turbulences and air movements on all scales mix the ingredients up to a height of 100 km. Above that height, the movements become too small to prevent molecular diffusion. There, in the heterosphere, the molecular density of each constituent decreases with its specific scale height. Therefore,

Constituent	Symbol	Molecular Weight	Fraction
Nitrogen	N_2	28.02	78.08 %
Oxygen	O_2	32.00	20.95 %
Argon	A	39.95	00.93 %
Water Vapor	H_2O	18.02	variable
Carbon Dioxide	CO_2	44.01	380 ppmv
Neon	Ne	20.18	18 ppmv
Ozone	O_3	48.00	10 ppmv
Helium	He	04.00	5 ppmv

Table 2.1: Composition of Earth’s atmosphere and a summary of the most common ingredients [Salby, 1995].

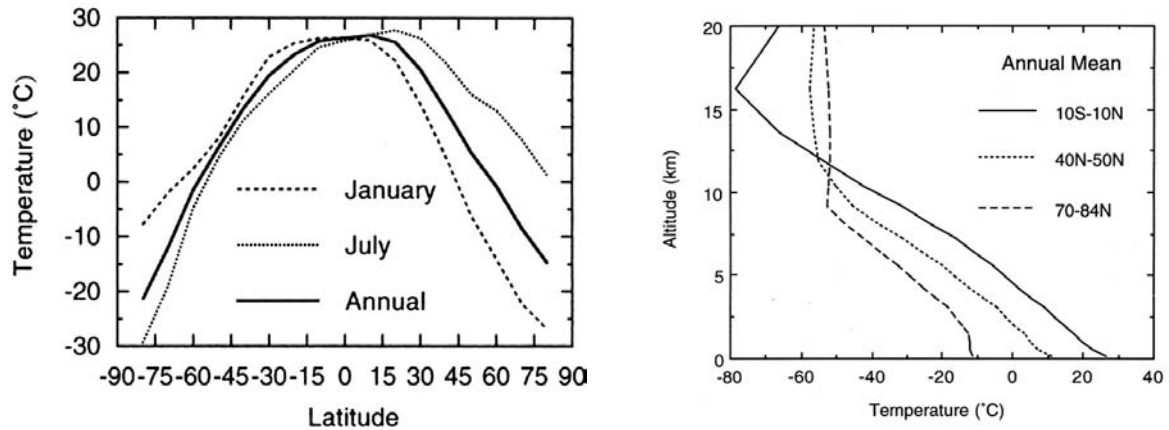


Figure 2.6: The left figure shows the global mean surface temperature as a function of latitude for January, July and the total year. The right one shows the annual average temperature profiles for three zonal means from the surface up to 20 km [Hartmann, 1994].

the heavier molecules dominate the lower parts while the lighter ones are mainly found in upper altitudes. The scale height, which defines the height in which the density drops to about 37 %, decreases with molecular specific scale heights.

In the homosphere, the dry air primary consists of nitrogen 78.08 %, oxygen 20.95 % and argon 0.93 %. They are neutral and do not interact with radiation. The main atmospheric constituents are listed in Table 2.1. Although, only less than 0.1 % are greenhouse gases, their effect is high enough to increase the surface temperature by 33 K, which is known as the natural greenhouse effect. The most important ones are water vapor (62 %), carbon dioxide (22 %), ozone (7 %) and methane together with nitrous oxide (6 %) [Malberg, 1997, pp. 296]. There also exists a large number of other trace gases (≤ 1 ppmv), which develop during chemical, biological and physical processes.

Ozone plays an unique role since it decreases with height in the troposphere, where it is known as an air pollutant and increases again in the stratosphere, where it reaches the maximum density between 20 km and 30 km due to several chemical processes in which ultraviolet radiation photo-dissociates molecular oxygen and becomes absorbed [McIlveen, 1998]. The result is a warming and the change in the sign of the lapse rate.

Water vapor is much more variable in space and time than ozone. It appears as vapor, cloud droplets or as ice crystals. The mixing ratio⁷ highly depends on the weather state. In average, water contributes with 1 % and in extreme cases with 3 % and decreases by a tenth between low and high latitudes. Water is very important for the climate system during feedback mechanisms and cloud formations.

⁷proportion of water vapor in comparison to dry air

Temperature

The temperature defines the single layers of the atmosphere. The lowest part is the troposphere, where temperature decreases with altitude, due to expanding cooling of rising air masses. The average lapse rate Γ is 6.5 K/km ($\Gamma \equiv -\partial T/\partial z$) and varies with latitude, season, and altitude. It is positive up to the tropopause, which is at about 17 km in the tropics and at 7 km at the poles [Gobiet *et al.*, 2005], and negative up to 50 km (Figure 2.5). Then, in the Mesosphere, the temperature decreases to about 170 K (at 90 km). The thermosphere above it is characterized by a sharp increase of the temperature, which is caused by photo-dissociation of nitrogen and oxygen and additional ionization of atmospheric gases [Hartmann, 1994].

The lapse rate close to the surface decreases with latitude and becomes negative up to several 100 m in high-latitude winter and springtime. This arises due to radiative cooling of the surface. The troposphere above it emits radiation not that efficiently and gains heat from lower latitudes. Therefore it cools down slower and shows a smaller annual and diurnal variability than the surface. The behavior in the troposphere and stratosphere is quite different. In high and mid latitudes the temperature of the lower stratosphere remains almost constant with height. But during winter, the temperature decreases again between 15 km and 20 km (Figure 6.19) and shows a wave-like pattern, which has to do with the natural ozone depletion. At the equator, where the troposphere extends up to 17 km, the lapse rate decreases rapidly with height up to the tropopause, as visible in Figure 2.6.

Pressure

Pressure is beside temperature and composition, a further main atmospheric parameter. It is highest at sea level and decreases exponentially with height z . Generally pressure p is the force, which acts on an unit area. It arises from collisions between molecules, which we assume to be in an arbitrary box, and the walls of the box. With increasing temperature T , the velocity of the elements increases as well and therefore raises also the pressure. This is described with the ideal-gas law, where R_{mol} is the molar gas constant and R the universal gas constant. Additionally the pressure increases with the number of elements, which corresponds to the density ρ .

$$p = \rho R T = \frac{\rho}{M_d} R_{\text{mol}} T \quad (2.2)$$

A positive force would to expand the box like a balloon, which means that the walls are pushed with a higher frequency from inside than from outside. If this box is opened on one side, the molecules are accelerated into that direction and air streams out with a magnitude, which corresponds to the pressure gradient. Molecules with a higher molecular weight need less acceleration to provide the same force than lighter ones. To restrain the air from streaming out it needs a force which acts into the opposite direction. In the terrestrial

atmosphere exists a vertical pressure gradient, which is balanced by the gravity g .

$$g = -\frac{1}{\rho} \frac{\partial p}{\partial z} \quad (2.3)$$

The replacement of the density with the ideal gas law and the integration over pressure and height gives the hydrostatic equilibrium of the atmosphere [Hartmann, 1994], where p_s is the pressure at sea level, $p(z)$ the pressure at height z and H the scale height, which determines the height in which the pressure falls to $1/e$ ($\cong 0.37$). At the surface (T is 288 K), this is 8426 m.

$$p(z) = p_s e^{-\frac{z}{H}} = p_s e^{-z \frac{g}{RT}} \quad (2.4)$$

Pressure decreases exponentially with height, while the temperature alters the scale height. About 88 % of the sea level value are available at a height of 1000 m, 50 % in 5840 m, 17 % in 15000 m and not more than 3 % are left in 30000 m. Those values are only simple estimates of the real pressure curve. In fact the temperature varies with height (as well as gravity) and creates a continuously changing scale height.

2.2.2 Hydrosphere

All available liquid and gaseous water above, on, and below the surface belong to the hydrosphere. About 71 % of the Earth's surface are covered by oceans [Hartmann, 1994]. From the total water content are 96.5 % salt-water and the rest fresh water. Glaciers, snow, and ice belong to the Cryosphere and make 68.7 % of the available fresh water. They play a different role in the climate system and are therefore treated separately. Further 31 % of the available fresh water are groundwater and permafrost. Those are located far below the surface and influence the climate system indirectly, when they supply vegetation with liquid. Only 0.3, % of the fresh water is stored in rivers, lakes, and swamps on the surface [Gleick, 1996, pp. 817].

Oceans play a fundamental role as heat storage and transporters [Baede *et al.*, 2001, pp. 88]. They transport heat from low latitudes toward higher latitudes and increase the mean temperature of high latitudes and damp the annual variability. Ocean currents are generated by winds and density gradients, which arise due to temperature and salinity differences. A good example gives the climate of western Norway and southern Alaska. Both are located at the same latitude but experience different ocean streams⁸. In Bethel (western coast of Alaska) the monthly mean temperature ranges between -14.3°C in February and 12.8°C in July⁹ while in Bergen (same latitude and approximately the same topography) the annual temperature ranges between 1.3°C and 15°C during the same period¹⁰.

Furthermore Oceans store much heat and act as the prime carbon dioxide sink. The heat

⁸<http://koeppen-geiger.vu-wien.ac.at/pics/kotteketal2006.gif>

⁹<http://www.klimadiagramme.de/Namerika/bethel.html>

¹⁰<http://www.klimadiagramme.de/Europa/bergen.html>

2 The Climate System

storage arises due to the high heat capacity and conductivity (compare with soil). Water becomes mixed by convections and other turbulent movements [Baede *et al.*, 2001]. Therefore the tropical oceans can warm until a depth of about 400 m. That's much deeper than for the lithosphere, where heat penetrates only a few decimeters downward [Hartmann, 1994, pp. 13, 86].

Water Vapor in the Atmosphere

Water in the atmosphere belongs to the hydrosphere too and consists of 0.0008 % of the total available water or 0.03 % of the fresh water content. There it appears as water vapor, cloud droplets or as ice crystals. The atmosphere plays an important role for the water cycle. Water evaporates at the oceans, rivers, lakes and seas or transpires at the leaves of plants. Then it convects upward and is moved away by the winds. If the specific humidity is high enough to saturate the air, water vapor condenses to clouds and releases latent heat. Since the saturation pressure depends on the temperature, the water vapor pressure decreases with increasing latitude and altitude. Therefore the polar atmosphere contains 90 % less water than the tropical one. Water vapor decreases exponentially with altitude. About half of the surface value is left at 2 km height and about 10 % at 5 km height.

2.2.3 Cryosphere

As mentioned above, the Cryosphere contains the total water in frozen form (i.e.: glaciers, sea ice, snow cover and, permafrost). It increases the albedo of the surface and cools the surrounding environment because of the low surface temperature. Important for the climatology is the area and not the thickness due to the low heat conductivity. The impact of an ice shield changes not much, after it has reached a depth of some meters.

About 11 % of the land and 7 % of the oceans are covered by ice and snow. Most of it can be found in Antarctica (89 %) and in Greenland (8.6 %) [Hartmann, 1994]. The cryosphere also acts as the promoter of the deep ocean convection. It cools the warm tropical streams, which become denser and start to sink down to the ground, where they flow back to the lower latitudes. The actual climate warming may melt a high amount of the glaciers and add much fresh water to the oceans. Especially melting ice of Greenland would decrease the salinity of the oceans and the water might become too light to sink down, what could shift or even break the Gulf Stream.

2.2.4 Lithosphere

Together with the Cryosphere and the Hydrosphere, the Lithosphere influences the absorption of solar radiation and its transformation in longwave radiation, sensible heat, and

latent heat. The location of the continents¹¹ determine the glaciers' extension and temperature variability. They influence the climate of the surrounding environment by controlling ocean streams and winds. Mountains for example hold back clouds, which rain out on one side. Obviously the topography changes the friction of the boundary layer. That dynamically influences the atmosphere due to transfer of angular momentum and dissipative kinetic energy.

2.2.5 Biosphere

The combination of Atmosphere, Hydrosphere, and Lithosphere is important for life to develop. They supply it with water and energy. But vegetation also influences them. The best example is oxygen, which has been produced after the development of plankton in the early geological ages. Vegetated areas decrease the albedo and store water, which is returned to the atmosphere, where it falls back as precipitation. Without them, water would quickly flow back to the oceans or sink into the ground. Less water evaporates and the air becomes drier. Surface water damps the temperature maximum and the diurnal variability, which would fall out in that case.

Plants, animals, and especially humans also control the carbon dioxide and many other cycles. This again is important for the absorption of longwave radiation. Since humans have started to emit industrial greenhouse gases, the radiation balance got out of balance. The composition of the atmosphere has changed and may continue changing in the further future.

2.3 Climate Variability

The climate system is quite complex since all components are strongly connected with each other and interact via transfer of energy, mass and momentum. But the components are not stable. They change dynamically with time and space, which has to do with internal and external forces.

External forces are impacts on the climate system as a whole and have their origin in the interior of the Earth (plate tectonic and volcanoes) or in the space (meteorite impact). The sun is the main energy source and a change of its activity, which is visible through the appearance of sun spots, impacts the radiation balance. Sun spots are colder areas and arise due to disruption of the outflowing energy. They are super compensated by bright surrounding areas and disappear after several weeks. Their number changes periodically every 11 years. A connection with the magnetic polarity gives a total sun activity cycle of 22 years. The net effect on the climate system is quite small. A variation of $\pm 1.5 \text{ W/m}^2$ could be measured by satellites. Nevertheless exists a strong correlation between the little ice age and the virtual absence of sun spots in the 17th and 18th century [Hartmann, 1994,

¹¹The continents are stable on a scale of several 1000 years.

pp. 287]. Changes in the orbital parameters produce a bigger impact. The orbit of the Earth changes between an almost circular shape to a more elliptic one every 100000 years. The eccentricity defines the variability of the mean insolation throughout a year, which becomes important in connection with the precision. Like a gyroscope Earth's rotation axis wobbles around the normal to the planetary orbit plane. Actually the rotation axis points to the polar star Polaris. The axis rotates in a period of 21000 years and with it the date of the closest distance¹². The effect increases with the eccentricity¹³ up to 15%. The reason is the difference of the insolation between winter and summer, perihelion and aphelion. Regions beyond the polar circle receive no radiation during winter and are dependend on the insolation in summer. Important for the high latitudes are also changes of the obliquity (tilt angle), which varies between 22.2° and 24.5° within 41000 years. It can raise the summer insolation by about 10%. Together with the eccentricity and precision the insolation can decrease by 30% in the high latitudes.

A periodic oscillation between ice age and warmer interglacial could be determined from ice cores for the past million years. Since the impact of these orbital parameters correlate to temperature, they are supposed to have triggered warming and cooling. Sometimes the temperature changed rapidly by several degrees within one human life time. In the last 10000 years the temperature has been quite stable and varied only slightly. For a closer description see *Solomon et al.* [2007] in the AR4, 2007.

Changes in insolation are not responsible for the total temperature variation. Feedback mechanisms of the climate system have amplified the orbital effects. If e.g., the temperature decreases the ice volume increases. That raises the albedo and therefore the temperature drops even more, called the ice-albedo feedback. If water vapor evaporates the temperature increases because of the greenhouse effect and this leads to further evaporation. Other feedbacks are self regulators. A temperature increases results in a higher longwave radiation output. Therefore, the radiation balance is negative and that leads to a cooling [*Baede et al.*, 2001]. There are many other physical and biochemical feedbacks. Biochemical is a connection of biological, chemical and geological elements. The vegetation may change with temperature and with it the albedo. A relationship exists between carbon dioxide concentration and the uptake rate of the oceans. A closer insight into the feedbacks mechanisms can be found in *Hartmann* [1994, pp. 229] or *Baede et al.* [2001]. Another problem is that many processes and interactions occur nonlinear and show a chaotic behavior. This means that the impact of a climate force depends on the initial conditions. A small change can be compensated in one case but can also trigger a domino effect in another case. That limits the precision of climate models and uncertainties rise with the length of the simulated time period¹⁴. Positive and negative feedback mechanisms and interconnections between several climate-components are known as internal forces and dynamically influence the climate system. In a quasi stable condition the climate parameters are controlled by negative and positive feedbacks. The properties change from one year to another but tend to remain

¹²The perihelion is actually at the 5th of January.

¹³<http://www-earth.usc.edu/geol150/variability/orbitalchanges.html>

¹⁴Compare with weather predictions, which lose reliability with time.

Annual Greenhouse Gas Emissions by Sector

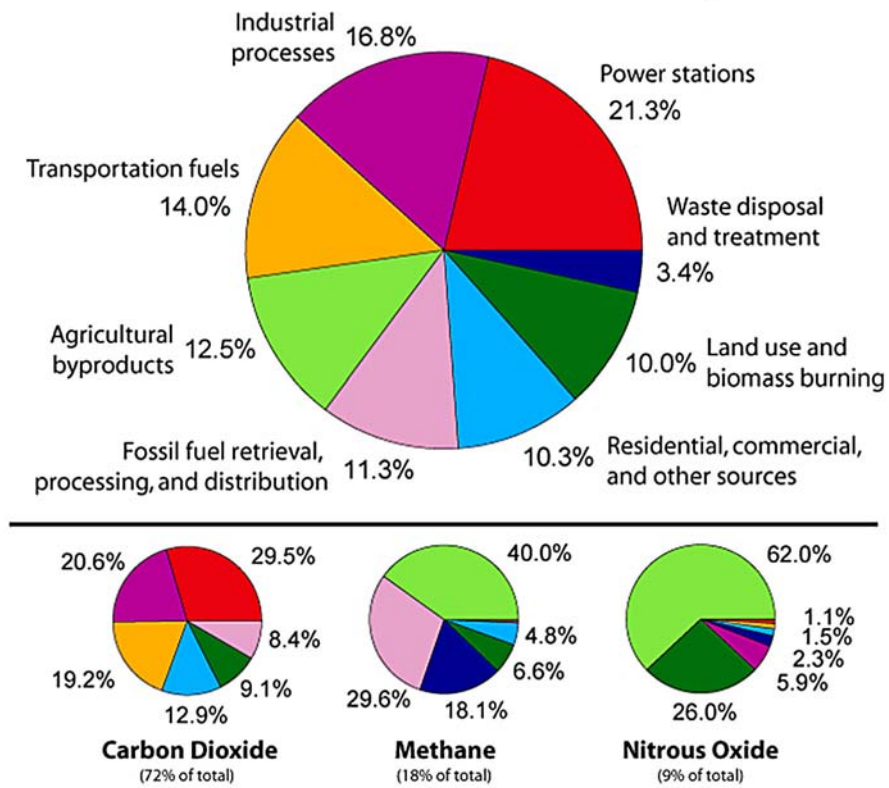


Figure 2.7: The proportion of the prime greenhouse gas emitters on the total anthropogenic impact throughout a year. The lower panel considers the prime human-made greenhouse gases CO₂, CH₄ and NO₂ http://en.wikipedia.org/wiki/Greenhouse_gas.

at an average value within a period of 10 to 100 years. On a regional scale the climate system becomes more complex. Heat and precipitation supply may change due to internal forces. If one region cools another one warms. A good example gives ENSO (El Niño Southern Oscillation), which is an abnormal warming of the eastern Pacific. Because of that a low pressure system develops where usually a high pressure system is. This causes floods in Peru and droughts in Indonesia.

Volcanism and fossil fuel burning count to external forces, although they originate in the interior of the Earth. They change the composition of the atmosphere and the radiation balance. Anthropogenic burning of coal and oil releases carbonates and methane, which have been driven away from the climate system over the past geological ages. During volcanic eruptions sulphurous gases are injected into the atmosphere, where they react to SO₂ and to sulphurous aerosols. In the troposphere they fall out quite quickly after some weeks. But during large explosive eruptions, these gases are emitted into the stratosphere, where they distribute over the total globe and sometimes stay for several years. They absorb the solar infrared radiation, which in turn warms the stratosphere and cools the troposphere

and the surface, as it was observed after the last three large volcanic eruptions: Pinatubo (Philippines) in 1991, El Chichon (Mexico) in 1982, and Agung (Indonesia) in 1963 (see: Figure 2.9).

2.3.1 Anthropogenic Climate Change

Every organism influences and changes its environment. But the role of the humans is very special and has largely increased since the industrial revolution in the mid 18th century. Since then, the concentration of the greenhouse gases has reached values far above the preindustrial quantities, as determined from ice cores [Solomon *et al.*, 2007]. CO₂ arises mainly because of fossil fuel burning. About two third of the anthropogenic emission arises from traffic, industries, and power production. Also important are land use changes like biomass burning and agricultural byproducts. The concentration has already increased by one third and still increases by about 1.9 ppm/year¹⁵. Alone 50 ppm of 100 ppm have been added in the past three decades. Therefore the concentration has by far exceeded the natural range of the past 650 Ky. A similar behavior can be observed from other greenhouse gases, as visualized in Table 2.2. Methane develops during agricultural processes like rice farming, land use changes, and fermentation¹⁶, which have increased by more than 70 % since 1750. A closer separation of the main emitters is shown in Figure 2.7. A much higher increase of 700 % was observed in the concentration of nitrous oxide, which mainly originates from agricultural processes. But methane didn't increase much since the early nineties (plus 42 ppb) [Solomon *et al.*, 2007] and the concentration of nitrous oxide has remained constant since 1980.

The warming potential of the components is quite different because of the different lifetimes. Table 2.2 shows the growth rate and the effect on the radiation balance of the greenhouse gases¹⁷. Their concentration in the year 2005 was as follows: 379 ppm (CO₂), 1.774 ppm (CH₄) and 0.319 ppm (NO₂). The CFCs show a very high warming potential and are responsible for ozone destruction in the stratosphere. They are used in refrigeration, fire suppression systems, and in manufacturing processes. Recently, the concentration has stabilized, so that the ozone layer can recover.

Together all emissions of greenhouse gases have increased the radiation balance by 2.4 W/m² (Table 2.2). Additional air pollution with black carbon, organic carbon, sulphate and dust has canceled a part of the impact. The aerosols have directly increased the reflection by 0.5 W/m² and by further 0.7 W/m² due to a higher cloud growth rate. This is known as the global dimming which is responsible for the almost constant surface temperature in the sixties and seventies. Since people have started to reduce air pollution, the dimming effect has decreased and a significant temperature trend was observed. More

¹⁵Average growth rate between 1995 and 2005 [Solomon *et al.*, 2007]

¹⁶More detailed information about the greenhouse gas emitters are available on the webpage http://en.wikipedia.org/wiki/Greenhouse_gas

¹⁷http://en.wikipedia.org/wiki/Greenhouse_gas and http://www.grida.no/climate/ipcc_tar/wg1/221.htm

Greenhouse Gas	Element	Contribution 1998	Radiative force
<i>Carbon Dioxide</i>	CO_2	365 ppm (280 ppm)	$1.66 W/m^2$
<i>Methane</i>	CH_4	1.745 ppm (0.715 ppm)	$0.48 W/m^2$
<i>Nitrous Oxide</i>	NO_2	0.314 ppm (0.270 ppm)	$0.16 W/m^2$
<i>Tropospheric Ozone</i>	O_3	0.034 ppm/(0.025 ppm)	$0.35 W/m^2$
<i>CFC-12</i>	CCl_2F_2	533 ppt	$0.13 W/m^2$
<i>CFC-11</i>	CCl_3F	268 ppt	$0.07 W/m^2$
<i>CFC-113</i>	$Cl_2FC - CClF_2$	084 ppt	$0.03 W/m^2$
<i>HCFC-22</i>	$CHClF_2$	069 ppt	$0.03 W/m^2$

Table 2.2: The most important greenhouse gases, the current and preindustrial (in brackets) concentrations, and their impact on the radiation balance [Houghton et al., 2001].

detailed information is available in the IPCC report from 2007.

Overall the surface temperature has increased by $0.74^\circ C (\pm 0.18^\circ C)$ on a global scale between 1906 and 2005 [Solomon et al., 2007], as listed in Table 2.3. The positive trend was not limited on the surface. In the mid troposphere e.g., the temperature increased by $0.17^\circ C$ per decade between 1979 and 1998 [Fu et al., 2004], as visualized in Figure 3.9 and in Figure 3.10. The warming has also penetrated about 3000 m down into the oceans, which store about 80 % of the additional available heat in the climate system. Therefore, the largest fraction of the observed sea level rise belongs to the thermal expansion of water. The sea level has increased by about 17 ± 5 cm in the last century with 3.1 ± 0.7 mm/year between 1903 and 2003 [Solomon et al., 2007]. Only a small part arises due to the melting glaciers in all mountain ranges. The alpine glaciers for instance have lost about a third of their area since 1850 and almost all of them are actually shrinking. Mountain range glaciers are shrinking as well as the amount of snowfall in the northern and southern hemisphere, but the large ice shields on Greenland and Antarctica are not melting significantly. Nevertheless the flow speed has increased, what indicates a slow thinning of the ice masses and that a higher volume breaks off into the sea.

On regional scale the precipitation amount, ocean salinity and wind pattern has changed quite differently. While the eastern North and South America, northern Europe and central Asia have experienced more rain, the southern Africa and the Mediterranean became drier. The number and intensity of droughts has increased over most parts of the continents. An analogous trend could be seen in the frequency of heavy precipitation. This corresponds to the additional water vapor which can be held by warmer air. A change of extremes could also be observed besides the temperature rise. It is very likely that the number of hot days has increased while the number of cold days and frost has decreased and it is virtually certain that those trends continue in this century. The emission of greenhouse gases still increases, with even faster speed than before. This might lead to a stronger temperature trend. Maybe this will be comparable with abrupt climate changes, which have already happened several times. Note that the temperature has been $2^\circ C$ higher than nowadays after the last ice age [Solomon et al., 2007].

	1910 - 1945	$\pm 2\sigma$	1946 - 1978	$\pm 2\sigma$	1979 - 2004	$\pm 2\sigma$
Total Earth	0.140	0.046	0.007	0.049	0.165	0.056
All continents	0.109	0.053	-0.008	0.055	0.235	0.094
All oceans	0.153	0.043	0.013	0.047	0.136	0.041
NH total area	0.149	0.053	-0.040	0.072	0.235	0.083
NH continents	0.140	0.068	-0.043	0.064	0.317	0.115
NH oceans	0.155	0.044	-0.038	0.077	0.183	0.062
SH total area	0.126	0.046	0.064	0.056	0.094	0.053
SH continents	0.068	0.059	0.036	0.062	0.125	0.081
SH oceans	0.140	0.043	0.071	0.054	0.087	0.047

Table 2.3: The observed surface temperature trends in K/decade for rural and maritime areas on a global and hemispherical scale in the 20th century. Equivalent data from different sources were summarized [Solomon *et al.*, 2007].

But some phenomena, which are expected when temperature raises, could not be observed. The Antarctic sea ice extent shows only an inter-annual variability but not a significant trend, probably due to the high altitude of the glacier surface, where temperature can hardly exceed the zero-degree range. Changes of the global ocean circulation and weather events as hail and tornadoes could neither be detected. All in all, the warmth of the second half of the 20th century is unusual for the past millennium. The last decade was maybe the warmest one since 1000 AD. It is very likely that the emission of greenhouse gases is responsible for the increasing global surface temperature [Solomon *et al.*, 2007].

2.4 Climate Monitoring

As shown in the previous section, fundamental statements could be made for the development of the temperature over land and ocean. The results are undisputed and well accepted. The observational data stem from different sources and instruments, which were adjusted with respect to temporal changes in instrumentation, measurement technique, and environment (e.g. urbanization close to a weather station). The surface data sets were provided by different weather stations over land and by ships and buoys over oceans, which were homogenized to a global data set. Only the different sampling of measurement points introduced an uncertainty into the data series.

The atmosphere plays the most important role in the climate system and interconnects strongly with the surface. The lower layers of the atmosphere, especially the mid and upper troposphere and the lower stratosphere, will be mainly considered in this thesis. As a matter of fact, the observation of the atmosphere is more complicated than that of the surface, because most measurements can be carried out only indirectly. Two types of observation were successfully established in the past. On the one hand, there are radioson-

des and on the other hand, satellite observations. Radiosondes are temperature sensors on weather balloons, which are launched at weather stations and on ships. They measure within the free atmosphere at several altitudes and provide a temperature profile from the surface up to a height of about 30 km. As visible (purple and green lines) in Figure 2.9, radiosonde observations are available since 1958, when a great project was started during the geophysical year. The aim was to build up a continuous measurement time series of the atmosphere. The observations are to trust with caution, because they are limited to the northern extratropical continents and some ship tracks in between. The southern hemisphere and the tropics are under-represented and large gaps still exist over the southern ocean, South-America, Africa and the Middle-East. Additionally, all instruments are calibrated differently and the performance of the instruments changed over a longer time period. This is probably the reason, why the inter-annual variability during the sixties and seventies is large in comparison to surface based observations [Solomon *et al.*, 2007]. The 1976-1977 climate shift is related to the phase change in the Pacific Decadal Oscillation toward more El Niño events, as it is visible in the tropospheric radiosonde records (Figure 2.9).

Some years later in 1979, the satellite observations started with the global weather experiment. The NOAA satellites carry the MSU instruments, which sound the microwave emission of the atmosphere at several frequencies and provide the brightness temperature of a few atmospheric layers. The prime advantage was, that they provided global homogeneously distributed measurements with a small number of instruments and an almost indent calibration. But they could measure only some layers and provided no temperature profiles like the radiosondes. Furthermore, the satellites lost height and drifted in time over some years. In order to merge MSU observations to one time series, several intercalibration and correction procedures had to be applied. The result depends quite largely on the processing center, due to different retrieval mechanisms (Figure 2.9).

The first analysis of temperature trend results led to a big controversy about the reliability of observations and of climate models and the reality of anthropogenic climate warming. Recently, new and improved¹⁸ data sets showed tropospheric warming which is consistent with the surface trend. Generally, all observations, which were carried out since the late 1950s, measured a thermal warming of the surface and of the troposphere and a thermal cooling¹⁹ of the stratosphere. That is consistent with the radiative forcing of the greenhouse gases, the ozone depletion and the physics in climate models.

The question is now, how far and with which magnitude the change extends. In other words: "Does the atmosphere show a stronger warming than the surface or not?" Different types of observations showed different results. On the global scale, radiosondes showed a stronger warming of the troposphere than of the surface (since 1958), while satellite based observations brought no clear results, which suggest a stronger warming of the surface than of the troposphere since 1979. But the majority of climate models obtained a

¹⁸Some biases were found and corrected.

¹⁹"Warming" is meant in a sense of a positive temperature trend and not of an increasing internal energy, which can occur due to a moisture and/or temperature increase

2 The Climate System

stronger warming of the troposphere on the global scale. Thus, it is not yet clear whether the troposphere has warmed more or less than the surface.

Principally, there is no inconsistency between the results of observations and of all model simulations. The models could explain the temperature developments only with including the anthropogenic changes of greenhouse gases, aerosols, and stratospheric ozone in combination with the natural forcing.

For the tropical regions, almost all models obtained a stronger warming of the troposphere than of the surface, which means that the trend is amplified there relative to the surface. Especially in the tropics, such a behavior would confirm the physical understandings of the climate system, because more latent heat can be released by condensing clouds, due to higher temperature and evaporation rate at the surface. But nevertheless the majority of observations shows a stronger warming of the surface since 1979. Interesting is the point for the tropics, that models and observations show a similar amplification of the trend only on a year-to-year scale and not on longer scales.

There are several reasons why the atmosphere experiences a different development than the surface. Inhomogeneities which arise from different warming patterns on the surface are smoothed and balanced much quicker in the atmosphere. This changes the atmospheric circulation system, which in turn can trigger different trends on the surface. Then, the inversion layer of the high latitudes, which develops above ice and during winter, is separated from the atmosphere above it. This inhibits vertical mixing between the warmer troposphere and the surface layer. And finally, different natural and anthropogenic influences may alter the stratospheric, tropospheric and surface trends. The vertical structure of the temperature trend within the troposphere is caused by different processes, which depend on altitude and latitude.

Table 2.3 shows the observed temperature trends. On the global scale, the surface temperature increased by 0.12 K/decade since 1958 and by 0.16 K/decade since 1979, while the tropical surface warmed by 0.11 K/decade since 1958 and by 0.13 K/decade since 1979, respectively. For the troposphere the radiosondes showed a warming of 0.14 K/decade globally and of 0.13 K/decade in the tropics since 1958. Satellite observations show temperature trends ranging from 0.02-0.19 K/decade depending on the actual processing center.

The radiosonde trends are supposed to have a cold bias. The point is, that the sun heats the temperature sensors and introduces a warm bias, which has to be corrected. If the adjustment procedure is improved, the radiosonde measure a colder temperature than before, which results in a colder trend. Several aspects have proofed this assumption. For instance, radiosondes observed a stronger temperature increase during night than during day, while this difference becomes largest where the biggest discrepancy between the observed troposphere and the measured surface temperature trend exists. Also in the stratosphere, the radiosondes show much colder temperature time series than the satellites. There, the satellite data match the results from most climate models.

Figure 2.9 shows the observed temperature of the surface, the low troposphere, the mid troposphere, and the lower stratosphere on a global scale since 1958. Significant are peaks of temperature increase in the stratosphere after large volcanic eruptions in 1963, 1982 and 1991. Generally, in the stratosphere the temperature decreases due to ozone depletion.

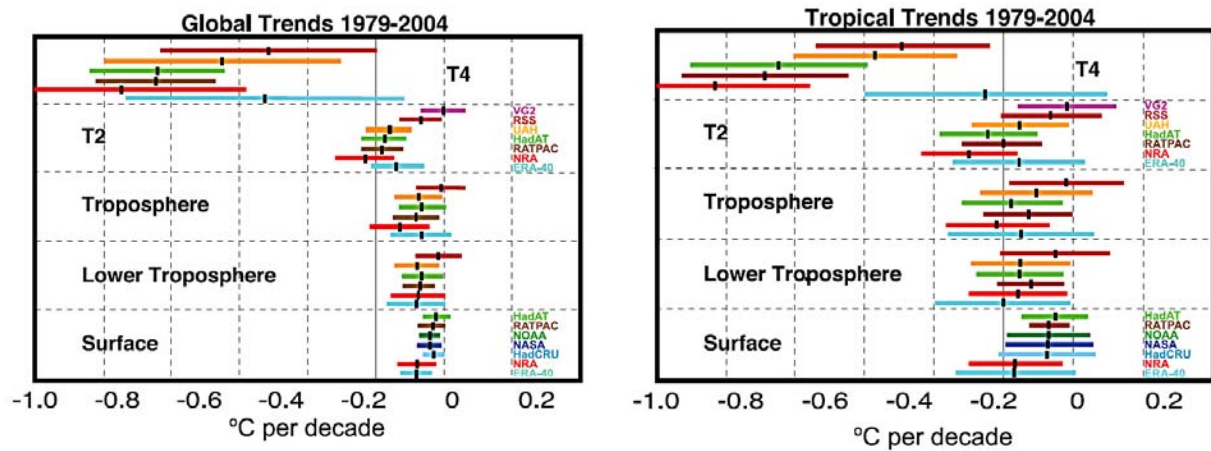


Figure 2.8: Observed temperature trends at three atmospheric layers and at the surface, separated between the global trend (left) and the tropical trend (right) [Solomon *et al.*, 2007].

Interesting are the stepwise decrease after large volcanic eruptions and a spread in the observations after 1993. Especially, the difference between the MSU and radiosonde measurements increased. In the troposphere and at the surface one can see a volcanic cooling effect. But in the year 1983 after the eruption of El Chichon, Mexico (1982), this effect was canceled by an El Niño, which is visible in an increasing surface temperature, contrary to what would be expected after large volcanic eruptions. El Niño is clearly visible in the year 1998, which was probably the warmest year of the last millennium. All in all, the surface and the troposphere have warmed since the seventies. The eighties and the early nineties showed quite stable conditions, when warmer years followed colder ones. Analogously to the stratospheric records, the tropospheric ones started to spread out as well in 1993. This marks the point, where the different temperature trends began.

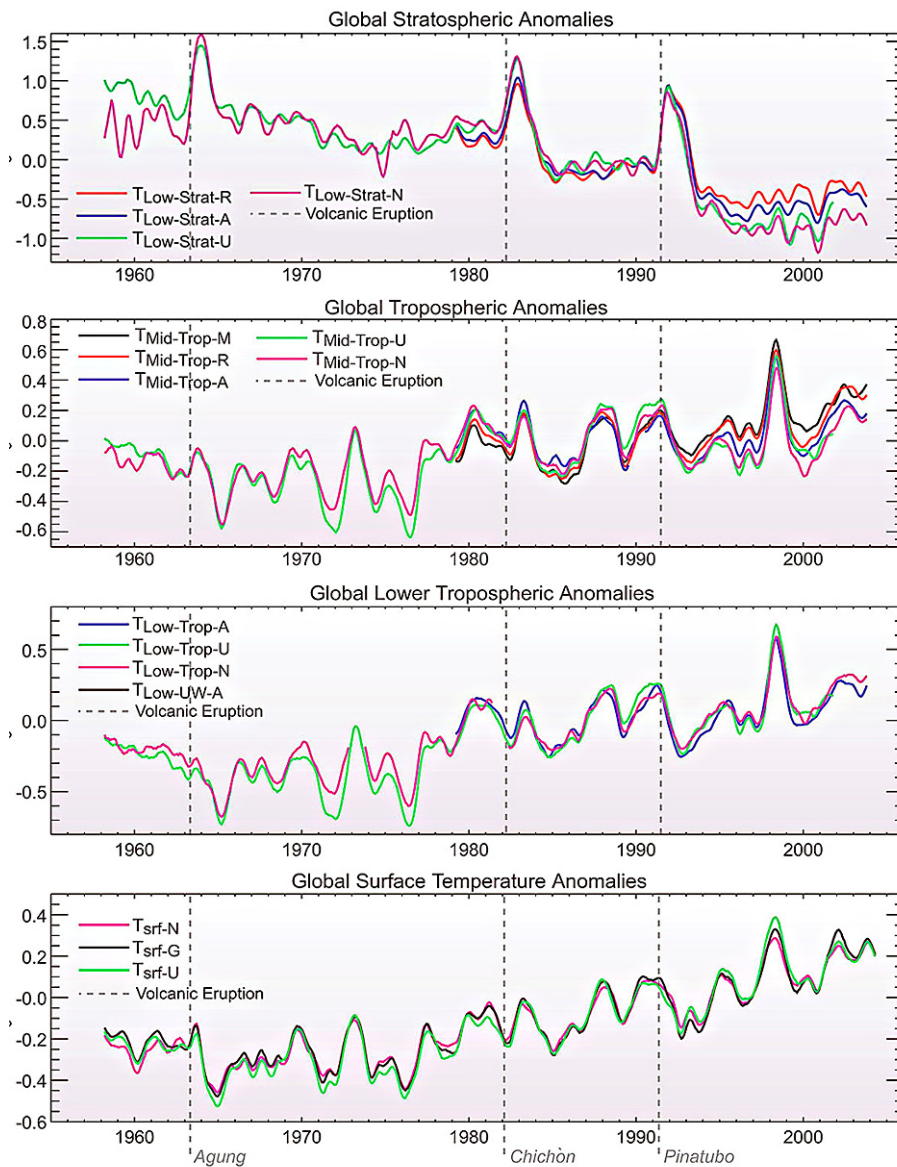


Figure 2.9: These time series visualize the observed global monthly temperature anomalies since 1958 relative to the mean temperature of the period 1979-1998. The values have been smoothed with a 7-month running mean filter and show temperature anomalies of the lower stratosphere, of the mid and of the low troposphere, and of the surface (top to bottom). The atmospheric temperatures are provided by different MSU processing centers (A, R, M, UW) and by two radiosonde records (U, N). The surface time series are produced by NOAA (surf-N), NASA GISS (surf-G) and UKMO/CRU (surf-U) [Solomon *et al.*, 2007].

3 Microwave Emission Measurements

The first continuous satellite based observations began with measurements of the atmospheric microwave emission with MSU¹ instruments in the year 1979. The main advantage was the global homogeneous resolution of several atmospheric layers, which could not be provided by earlier surface and radiosonde based measurements. The observations had been concentrated on North America, Europe, Eastern Asia and some ship tracks. Other countries had no technological resources for that or were hardly populated.

MSU brought necessary informations about the weather conditions over land and ocean. Accurate knowledge of initial and boundary conditions is important for weather forecast models to reduce errors and to enhance the reliability.

The importance of the satellite measurements for climate observations arose due to the discussion about climate warming in the late eighties and nineties. Therefore it was necessary to improve the accuracy of satellite based measurements and to minimize their errors. The smallest deviation can cause large temperature trend differences causing wrong conclusions and misinterpretations.

3.1 Physical Concept

3.1.1 Microwave Sounding of the Atmosphere

In general MSU provides measurements of the Earth's emission in the microwave spectrum. Since absorption at a certain frequency changes with pressure, temperature can be retrieved from the radiation output of the atmosphere. Interesting are regions close to absorption peaks of oxygen (and water vapor) at several frequencies in the microwave spectrum. For some reasons, described later, MSU measures radiation at four frequencies or channels close to oxygen's absorption peak at 60 GHz. At that point MSU would "see" only the highest atmosphere layer. The farther the observed frequency deviates from that point, the lower atmospheric regions can be detected by the instrument. In other words the observed height depends on the frequency. The emission informations are used to compute the brightness temperature in a further instance, what is carried out by several institutes like the University of Alabama, Huntsville² (UAH) and the Remote Sensing System, Santa

¹MSU ... Microwave Sounding Unit

²UAH ... University of Alabama, Huntsville, USA

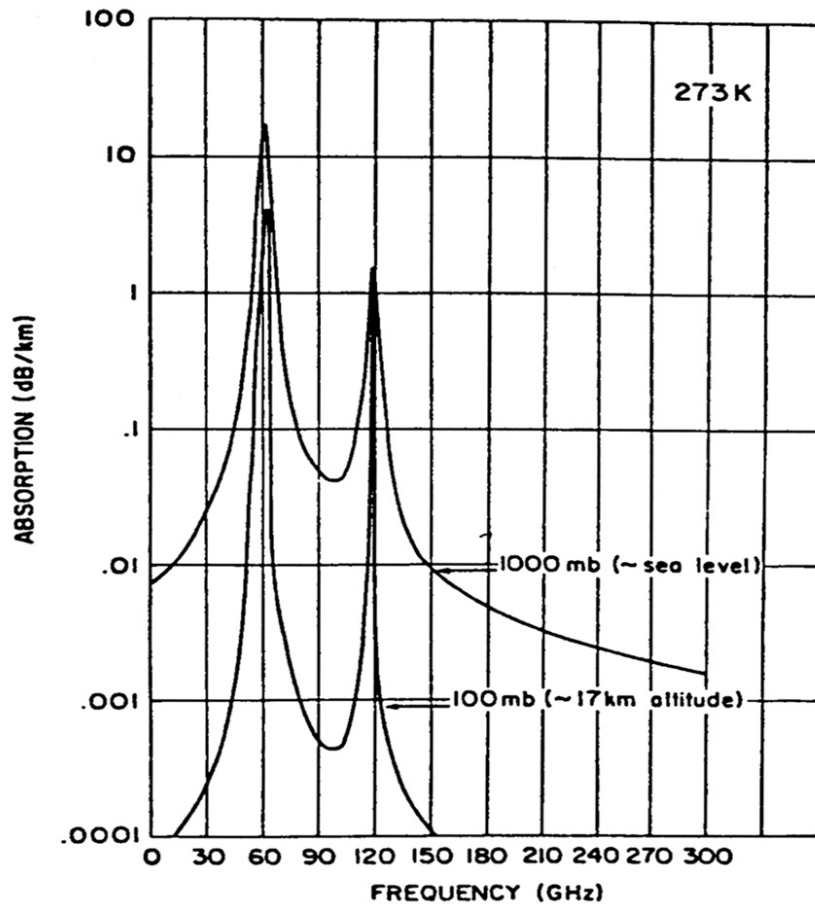


Figure 3.1: Absorption of O_2 in the microwave spectrum at 2 pressure levels (1000 hPa and 100 hPa) and at a constant temperature (273 K) [Chahine, 1983; Elachi, 1987].

Rosa³ (RSS). Brightness temperature means, that not only one height layer contributes to the observed radiation. Rather all altitudes contribute to the outgoing radiation, which is normally distributed around an altitude layer, which has the largest influence on the outgoing radiation. This relationship is quite well described by the so-called weighting functions.

The MSU instruments are fixed on-board of several Earth orbiting satellites, which were built and launched by the Jet Propulsion Laboratory⁴ for the National Oceanographic and Atmospheric Administration⁵, which runs them for daily weather observations, observes their orbits, and is responsible for reliable measurements [Spencer *et al.*, 1990].

³RSS ... Remote Sensing System, Santa Rosa, California, USA

⁴JPL ... Jet Propulsion Laboratory

⁵NOAA ... National Oceanographic and Atmospheric Administration

3.1.2 The Microwave Absorption Spectrum

There are several ways for the molecules to interact with radiation, depending on their shape and other set-up properties. Radiation is either absorbed, scattered, or reflected. If the energy of a photon equals to the difference between two energy states of a molecule, it becomes absorbed and the energy is transformed into thermal, rotational, vibrational, or electronic energy. The largest differences, which require high energies, describe electronic and the smallest rotational transitions. The energy E of a photon is directly proportional to its frequency ν

$$E(\nu) = n\hbar\nu \rightarrow (n = 0, 1, 2, \dots). \quad (3.1)$$

This is the Planck's equation, which describes discrete energy levels of an atom ($E(\nu)$), which is a function of the proportionality factor \hbar (Planck's constant) and the frequency (ν). The sum over all of them gives the characteristic emission or absorption spectrum. Each transition requires energy equal to $\hbar\nu$.

The microwave sounding technique applies the microwave spectrum between 1 mm ($\cong 300$ GHz) and 100 mm ($\cong 3$ GHz) (Figure 3.1), which is the region of rotational energy levels. There are four types of rotating molecules (three nonlinear modes and one linear mode). Nonlinear molecules produce a permanent electrical dipole moment because they have comparable moments of inertia and that is important to produce rotational energy bands. Either all three moments of inertia are the same (spherical top, e.g. CH_4) or two of them are equal (symmetrical top) or all of them are different (asymmetrical top, e.g. H_2O) [Elachi, 1987]. Linear molecules do not have electrical dipole moments because two inertia moments are the same and the third one is negligible. Though O_2 is a linear molecule, it produces rotational transitions. The reason for that is the permanent magnetic dipole moment, which arises due to the two unpaired orbital electrons. The orientation of the electronic spin changes relative to the molecular rotational direction. There follow rotational spectral lines at 60 GHz and one 118.75 GHz. Oxygen and water vapor are the main absorbers in the microwave spectrum. The decision to use oxygen is based on its high space and time stability [Warnek, 1988]. O_2 is uniformly mixed up to 80 km and has a fraction of 20.95 %, which is independent from atmospheric properties. The water vapor content variates strongly with space and time, because it depends on temperature, which changes within a day and a year. Furthermore winds and turbulences transport air to other regions and mix it with the air masses there.

3.1.3 Line Broadening

Line broadening is the precondition for successful remote sensing, because it enables observations of deep atmosphere layers. The curves have a Gaussian structure and are not a Delta function with an infinite narrow width. There are several reasons for the broadening of absorption lines.

3 Microwave Emission Measurements

1. *Natural Broadening* results from the time, that molecules need to absorb and emit photons and from the finite precision of determining the frequency.
2. *Doppler Broadening* is induced by thermal movements of the molecule relative to the emitted light, which causes a Doppler shift of the absorbed frequency. Doppler broadening is more important than the natural broadening and dominates in high altitudes with low pressure.
3. *Lorentz Broadening* or *Pressure Broadening* occurs due to collisions between two and more molecules. This in turn induces a little amount of energy, what enables to absorb a broader range of photons. The Lorentz broadening dominates in the troposphere (Figure 3.1).

These broadening mechanisms produce the characteristic shape of the terrestrial absorption spectrum. The number of collisions rises with increasing pressure and the Lorentz curve becomes broader and absorption of photons with lower frequency becomes more probable. That is important in remote sensing because the shape depends primary on the pressure, which can be linked to temperature with the ideal gas law. The atmosphere is opaque for electromagnetic waves with the frequency at a physical spectral line. Signals, which arise from lower atmospheric layers, are invisible. Therefore frequencies are chosen, which lie within the wings of the absorption curve, where transmission is more probable.

Each atmospheric layer influences the passing radiation differently. The top of the atmosphere influences the microwave radiation rarely because of the low density, which increases exponentially with decreasing altitude. Therefore the number of absorbers and emitters. is rising. The impact increases rapidly and reaches its maximum at a specific height, which depends on the optical thickness τ , which in turn is related to the absorption coefficient. The absorption coefficient is a function of frequency. It is highest at the spectral lines and decreases in the wings. Below that height, the impact decreases again since radiation has to pass the whole atmosphere above it. The connection of all influences within the atmosphere gives a continuous curve known as the weighting function [Elachi, 1987].

3.1.4 Derivation of the Weighting Functions

This section follows mainly the textbook of Elachi [1987]. In the microwave spectrum radiation energy can be described with the Rayleigh Jeans approximation ($kT \gg h\nu$) of the Planck's law, where k is the Boltzmann constant. The terrestrial radiation increases linearly with temperature T and quadratic with frequency ν . That is valid for the Earth's

emission since the maximum is within the infrared spectrum at a much higher frequency.

$$B(\nu) = \frac{2k\nu^2}{c_0^2} T(\nu) \quad (3.2)$$

$$dB = -\alpha(\nu, z)B(\nu, T(z))dz \quad (3.3)$$

$$dB = -\tau \frac{1}{B(\nu, T(z))} \quad (3.4)$$

While light penetrates through the atmosphere (c_0 is the speed of light in vacuum) it becomes partly absorbed, while the rate of intensity reduction (dB) is proportional to the absorption coefficient α .

The electromagnetic waves, which are emitted at height h with intensity B and frequency ν , have to penetrate through the total atmosphere above their source height. The amount of absorbers, which they have to pass, decreases exponentially with altitude and is actually the optical thickness τ

$$\tau(\nu, z) = \int_h^\infty \alpha(\nu, h)dh. \quad (3.5)$$

Furthermore the number of emitters has to be taken in account. The sum over all of them gives the radiation, which is received at the top of the atmosphere, $B_t(\nu)$. For simplification the surface is treated as a single emitter, $B_s(\nu)$.

$$B_t(\nu) = B_s(\nu)e^{-\tau_m(\nu)} + B_a(\nu) \quad (3.6)$$

$\tau_m(\nu)$ is the optical thickness of the total atmosphere. Since radiation is proportional to temperature, $B(\nu)$ can be directly replaced by $T(\nu)$ with the Rayleigh-Jeans approximation.

$$T_a(\nu) = \int_0^\infty T(z) \underbrace{\alpha(\nu, z)e^{-\int_h^\infty \alpha(\nu, h)dh}}_{W(\nu, z)} dz \quad (3.7)$$

This equation shows the weighting function W , which is a function of height z and frequency ν (Figure 3.2). The integration over all weighted temperatures gives the atmospheric temperature (T_a). Together with the "surface" one gets the brightness temperature T_b . The impact is actually normally distributed over all altitudes. Figure 3.2 shows the weighting function as a function of frequency and altitude.

But the absorption coefficient varies with density. Since pressure, which is proportional to density, decreases exponentially with height, the number of absorbers falls as well. A good help is the homogeneous mixing ratio of oxygen. Therefore the absorption coefficient $\alpha(\nu, z)$ is a function of height: $\alpha_0(\nu)e^{-z/H}$, which redefines the weighting function.

$$W(\nu, z) = \alpha_0(\nu)e^{-z/H - \alpha_0(\nu)He^{-z/H}} \quad (3.8)$$

At the surface (z is 0) W decreases to $\alpha_0e^{-\tau_m}$, with $\tau_m = \alpha_0(\nu)H$ and at the top of the atmosphere ($z \approx \infty$) W becomes zero.

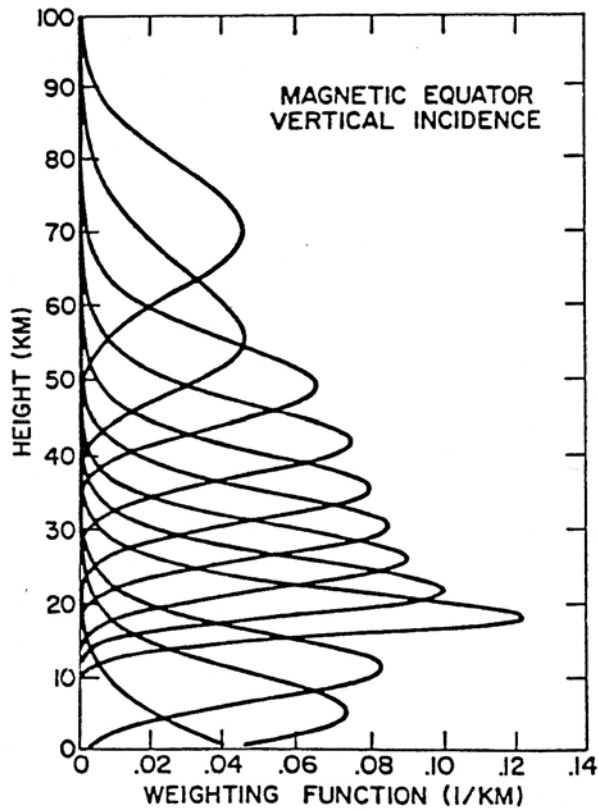


Figure 3.2: This picture shows all temperature weighting functions at nadir around the emission line of oxygen at 60 GHz, which are a function of altitude [Lenoir, 1968; Elachi, 1987].

Since τ varies with frequency⁶, the observed altitude can be changed easily, as visualized in Figure 3.2. Therefore NOAA measures the Earth's radiation at several frequencies below oxygen's physical emission line at 60 GHz.

3.2 First Satellite-based Observations

Originally satellites were launched to observe the Earth from space for various reasons (e.g. the American Air Force). First suggestions, that the temperature of the atmosphere can be measured via remote sensing came from King (1956). This was advanced by Kaplan (1959), who has shown that temperature profiles can be retrieved from the spectral distribution of the Earth's emission. The first weather satellite was the polar orbiter TIROS-1⁷. It was launched in Cape Canaveral in Florida on the 1st of April, 1960 to perform weather observations. He shot the first photos of the Earth's surface and its cloud cover (Figure

⁶ τ decreases with the distance from the physical spectral line

⁷TIROS ... Television and Infrared Observation Satellite

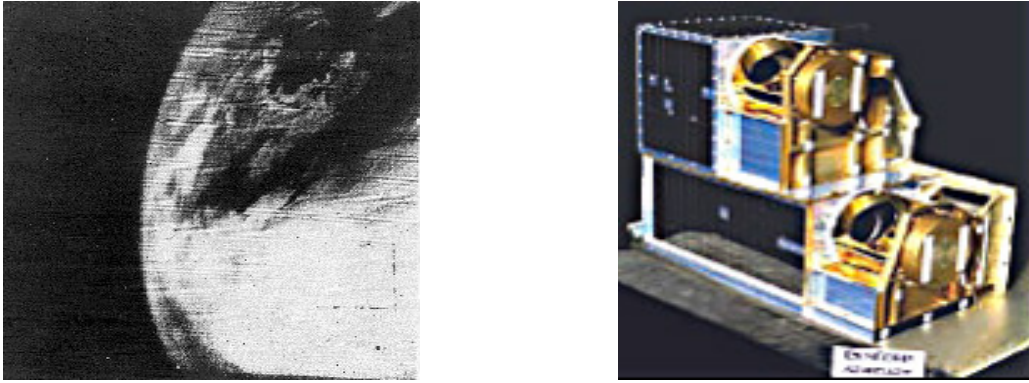


Figure 3.3: The left figure shows the first picture of the Earth from space (made on the 1st of April 1960) and the right one shows the AMSU-A1 instrument, which is used by the new NOAA satellites <http://www.centennialofflight.gov/essay/SPACEFLIGHT/metsats/-SP35.html>, [NASA/NOAA, 2004].

3.3). Nine more TIROS satellites followed the predecessor in the following five years, which produced over 10000 pictures. To that time CO₂ was of prime interest in remote sensing. The first temperature measurements have been carried out with TIROS-7 (launched in 1963), which carried a Medium Resolution Infrared Radiometer (MRIR), which observed the emission at 15 μm [Kennedy and Nordberg, 1967]. A series of Nimbus satellites was launched between 1964 and 1978 to test new remote sensing instruments and to apply improved data gathering methods. The satellite Nimbus-3 (launched in 1969) for example used the infrared spectrometer (SIRS). It measured six channels around 15 μm to gain the temperature of lower atmospheric layers like the troposphere and stratosphere. The following spacecrafts carried microwave spectrometers, ozone mappers, and radiometers. This was the start of globally distributed temperature measurements. A series of Improved TIROS Operational System (ITOS) satellites was launched by NASA for operational meteorological needs. The reliable and stable ones were handed over to NOAA for further use. The first one of them was NOAA-1, which was launched on the 11th of December, 1970. To that time NOAA could only measure over free and sparsely overcast regions, because clouds absorb the emitted infrared radiation [Waters, 1973].

This was actually the reason to measure the Earth's emission in the microwave spectrum. There are strong absorption lines of oxygen and also of water vapor. Meeks and Lilley [1963] have started the discussion about measuring the thermal emission of oxygen and derived the basic concept of temperature retrieval with the help of the microwave weighting functions, which can be used to determine the altitudes of the emitted electromagnetic waves. After some trials with earth-based observations and satellite measurements (Nimbus-5, 1972), microwave sounding became the main technique in the operational and synoptic meteorology.

The continuous temperature time series has finally started with the launch of TIROS-N in October 1978. The microwave emission of several atmospheric layers was measured twice a day by each polar orbiter. Three years later NOAA started to observe with two satel-

3 Microwave Emission Measurements

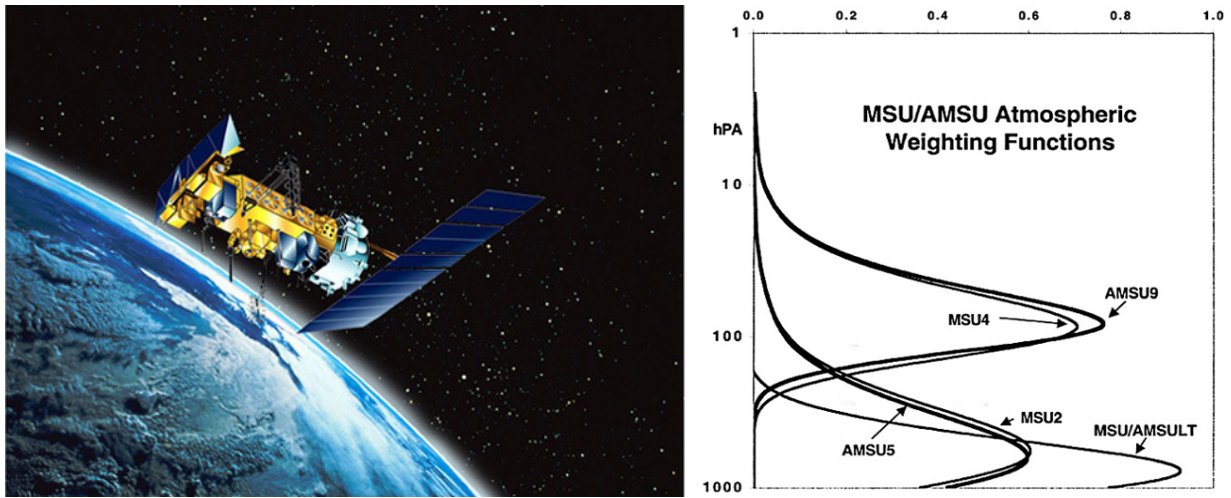


Figure 3.4: On the left hand is the MSU orbiter NOAA-16 and on the right hand the MSU weighting functions in comparison to the AMSU ones [Christy *et al.*, 2003; NASA/NOAA, 2004].

lites simultaneously with 90° difference in longitude. For instance a p.m. orbiter operated simultaneously with an a.m. satellite for two years and also two years with the following a.m. satellite. But problems raised due to time instabilities and technical problems.

The afternoon satellites drifted to later times and the morning ones drifted to earlier times. NOAA-9 operated for only 16 months and NOAA-13 was lost even after one week, due to insufficient power supply from the solar panels. NOAA-12 was probably accompanied by an additional emitting object in the cold space (important for calibration). The afternoon orbiter NOAA-11 suffered from an extremely large diurnal drift of more than four hours during its operation time of about six years. Finally it could be used as a morning satellite [Christy *et al.*, 1998; Vinnikov and Grody, 2003].

Since 1998 NOAA has applied the advanced-MSU⁸ to sound the atmosphere (one of them is shown in Figure 3.3). The main development beside some other improvements was the emission measurement at 20 spectral lines instead of 4. This improved the vertical resolution and enabled to observe many more atmosphere layers than before. The earlier MSU instrument measured the temperature of four layers: the low troposphere (T1), the mid troposphere (T2), the "upper"⁹ troposphere (T3), and the lower stratosphere (T4). Figure 3.4 shows the MSU channels (T2 and T4) in comparison to the analogous AMSU channels (channel-5 or TMT and channel-9 or TLS).

MSU was used beside AMSU until NOAA-14 was shut down in December 2004. 13 satellites have been launched since 1978 to measure the temperature of the troposphere and of the stratosphere. One of them is shown in Figure 3.4. Actually NOAA-18 is the youngest satellite¹⁰. It has been launched on the 20th of May, 2005.

⁸AMSU ... Advanced Microwave Sounding Unit

⁹The corresponding pressure levels sometimes belong already to the lower stratosphere, especially in the higher latitudes.

¹⁰<http://www.astronautix.com/project/tiros.htm>



Figure 3.5: Orbital path of a NOAA satellite. For one orbit it needs approximately 103 min. During that time the Earth rotates about 25.7° eastward. There follow 14 orbits per day <http://www.crisp.nus.edu.sg/~research/tutorial/spacebrn.htm>.

3.3 Temperature Retrieval

The MSU satellites are in a polar and almost sun synchronous orbit, which means that each place is scanned at the same local time. It orbits the Earth at an inclination angle of 98.9° at a height of 833–870 km¹¹. This is necessary to provide a daytime stable track around the globe. Usually there is launched one morning satellite (7:30 a.m. and 7:30 p.m.) and one afternoon satellite (1:30 a.m. and 1:30 p.m.). The spacecrafts encircle the earth from south to north in the evening or in the early afternoon (ascending) and from north to south in the night or in the morning (descending), as shown in Figure 3.5, [Christy *et al.*, 1995].

The antenna of the MSU radiometer measures at 11 view angles between 0° and 56° . The footprints at the surface have a circular-elliptic shape and provide a resolution of 110×109 km at the nadir and 178×320 km at the limb, as visible in Figure 3.6 [Spencer *et al.*, 1990]. In sum they are about 2000 km broad, which require about 26 s for one track scan. Over 3323 series can be measured during one day, which result in 36553 footprints. But only 23261 of them are actually used for further analysis, because they provide more reliable informations than signals from footprints closer to the limb, which have to penetrate a longer distance through the atmosphere and become more absorbed. Therefore the optical thickness increases and the weighting function changes, which introduces a cooling bias. Due to that the lowest seven points are used for TMT and TLS, after a limb correcting scheme has been applied [Spencer *et al.*, 1990; Spencer and Christy, 1992].

The radiometer counts the emission digitally. Then the brightness temperature is derived

¹¹<http://telsat.belspo.be/bE0/en/satellites/noaa.htm>

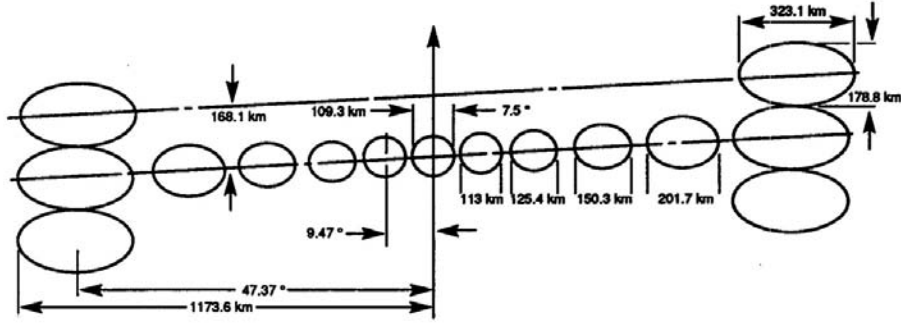


Figure 3.6: MSU cross track scan from a nominal orbital altitude of 833 km with an antenna of 3 dB beam width [Grody, 1983; Spencer et al., 1990].

from a calibration scheme, as described in Spencer et al. [1990], which consists of several steps. First of all, the number of counts (C_{raw}) has to be corrected quadratically to C_{earth} , because of the nonlinear instrument response. The coefficients (a_1 , a_2 , and a_3) vary with instrument and frequency.

$$C_{\text{earth}} = a_1 + a_2 C_{\text{raw}} + a_3 C_{\text{raw}}^2 \quad (3.9)$$

The space is assumed to have a background temperature of 2.7 K (T_{space}). Furthermore the temperature of the hot target, which is a hot platinum resistor (T_{target})

$$T_b = \frac{T_{\text{target}} - T_{\text{space}}}{C_{\text{target}} - C_{\text{space}}} * (C_{\text{earth}} - C_{\text{space}}) + T_{\text{space}} \quad (3.10)$$

T_b denotes the resulting brightness temperature of the footprint, T the observed temperatures and C_{space} resp. C_{target} the gathered number of counts from the space resp. the MSU hot target. After calibration, the data are checked for their reliability. The temperature of each footprint should be located within a temperature range, depending on the weighting function. Other results are suspicious. The mid tropospheric temperature e.g. is assumed to be located between 190 K and 290 K. If the difference between the temperature of one footprint and the average temperature of the two neighboring footprints does not exceed 1.5 K, the series is taken in account. Otherwise it would be skipped. This reduces disturbances due to snow covered mountains and short-scaled deep convections. If one measurement series has passed the tests, the seven footprint temperatures¹² closest to the nadir are combined to one brightness temperature [Christy et al., 1998].

The temperatures are sampled on a $2.5^\circ \times 2.5^\circ$ grid, while the nadir points are defining the cell of the brightness temperature. On average 85 % of the series are approved for further analyses [Christy et al., 1995]. If a grid remains empty, it is filled up by linear interpolation between the nearest eastern and western grid points unless there are not more than 15 cells missing. In that case a time interpolation between two daily means is made [Spencer and Christy, 1992].

¹²TMT and TLS require only five footprints

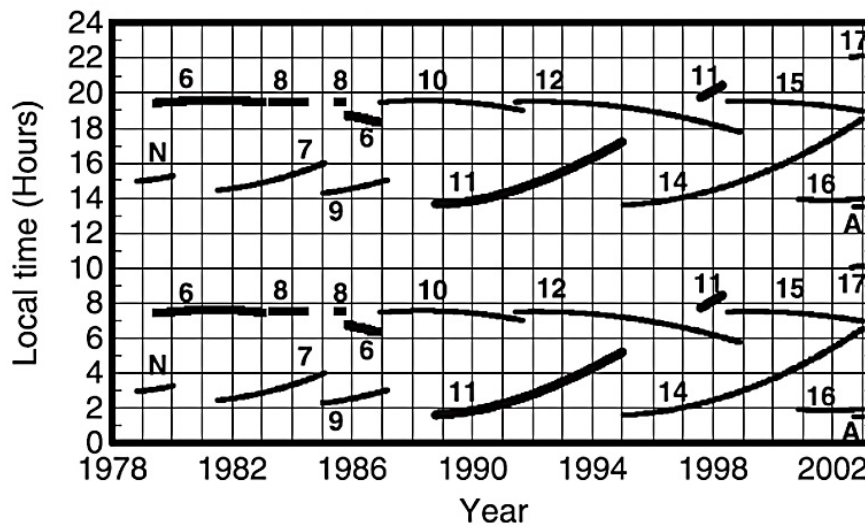


Figure 3.7: Those are the equator crossing local times of the polar orbiting MSU and AMSU satellites. The numbers correspond to the NOAA orbiters, N to TIROS-N and A to AQUA [Vinnikov and Grody, 2003].

3.4 Merging Procedure and Data Quality

After the retrieval of the brightness temperature of all MSU and AMSU data, the temperatures are combined to one homogeneous monthly mean time series from 1979 onwards. First, a reference annual cycle of absolute temperatures is calculated for NOAA-6 (a.m. orbiter) and NOAA-7 (p.m. orbiter) for the period common to both: September 1981 - August 1982. Then the reference annual cycles are smoothed to reduce fluctuations of less than 15 days. They are used as starting reference for all anomalies: the NOAA-6 reference annual cycle for all a.m. orbiters and the NOAA-7 reference annual cycle for all p.m. orbiters. Perturbation annual cycle removal, drift error correction, and random biases removal are included in the merging procedure described by *Christy et al.* [1998].

A five days median filter reduces the fluctuations and outliers which can arise due to weather changes and extreme weather events [Spencer and Christy, 1992]. Together with Fourier component analysis, the standard deviation of the difference between e.g. NOAA-11 and NOAA-12 decreased to 0.02K for monthly means. The annual difference time series and the attitude bias of each satellite is determined relative to its predecessor. After adjustment of all time series to the anchor satellite NOAA-6 a representative reference period is chosen for the complete anomaly series: January 1982 - December 1991 as the basis for tropospheric temperatures and January 1984 - December 1990 for stratospheric temperatures (the volcanic impact is excluded from the latter period).

The prime issue is to reduce the noise and to increase the signal to noise ratio, which is lowest over high regions like Tibet and continental areas which are some degrees north and south of the equator (e.g. Southern Brazil, Sahel, Eastern Indonesia, some points in the

3 Microwave Emission Measurements

Southern Ocean) [Spencer and Christy, 1992]. The mean bias of a daily or monthly mean average (T_{bias}) results from the square root of the sum over all temperature differences between one satellite ($T_{1,\phi}$) and a corrected one ($T_{2,\phi}$), weighted with the cosine of the latitude ϕ .

$$T_{\text{bias}} = \sqrt{\frac{\sum_{\phi=-82.5}^{82.5} (T_1(\phi) - T_2(\phi))^2 * \cos \phi}{\sum_{\phi=-82.5}^{82.5} \cos \phi}} \quad (3.11)$$

But problems arise due to the sparse overlaps in the eighties, especially of NOAA-8 and NOAA-9 (Figure 3.7), which measured only with one year overlap and that with a strong bias [Christy et al., 1998]. Usually an orbiter should work simultaneously with another satellite and its successor for four years. That could be provided since 1989, when all satellite showed reliable observations over the planned lifetime of four years. But those were sometimes affected by strong diurnal drifts of more than 4 h over their lifetime (e.g. NOAA-11 and NOAA-14), as visualized in Figure 3.7. Generally two years are needed to give reliable statements about drift error, inter-satellite biases, and disturbing annual cycles, which are shortly described now.

1. **Sampling effect:** Due to the orbital shape, MSU represents the higher latitudes better than lower ones, as shown in Figure 3.8. It provides well resolved observations in latitudes higher than 40° but leaves gaps below, while the largest ones remain at 25° . The reason is that the tracks cross each other in exactly that area. Since the

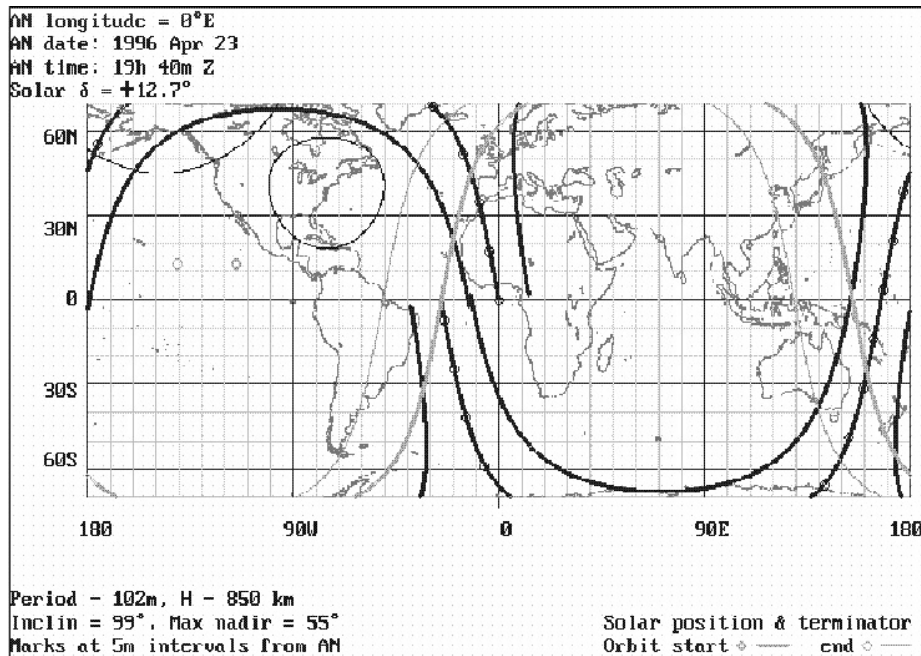


Figure 3.8: Orbital subtrack from a single NOAA polar orbiting satellite (NOAA-14) during one orbit, which lasts about 102 min <http://www.ncdc.noaa.gov/oa/pod-guide/ncdc/docs/klm/html/c2/sec2-3.htm#f232-2>.

whole pattern drifts 700 km eastward per day, the gaps vanish after three or four days. The consequence is, that the subtropical regions are represented less well than the higher ones on a monthly mean scale.

Additionally every satellite has another precision. Therefore, a difference analysis produces a 10 to 12 days oscillation, depending on the coincidence of the patterns. The error is smaller, if the patterns match each other and increases if they slip out of phase. More detailed information can be found in *Christy et al.* [1998].

2. **Disturbing Annual Cycle (DAC):** After the removal of the reference annual cycles, some annual variations can still remain. They indicate an error, which variates harmonically throughout a year. Different shadowing effects and insulations can cause such seasonal variations, which in turn influence the hot target and the retrieved brightness temperature [*Christy et al.*, 1998]. Although the target's temperature can easily be determined and calibrated, it has introduced variations of up to e.g. 7 K in the NOAA-11/12 difference time series. But only 2 % of the error propagates to the brightness temperature (the DAC bias on T_b is about 0.14 K) [*Christy et al.*, 1998]. Since the error varies like a harmonic oscillator with a wavelength of one year, it can be quantified and removed.
3. **Diurnal Drift Error:** Originally the MSU satellites were launched in a sun synchronous polar orbit. That should enable continuous observations of the Earth at the same local times. But they could not keep the angular rotation velocity and drifted by about one to two hours on average over a satellites lifetime. The afternoon orbiters have drifted to later local times ($\gg 2$ h) and the morning ones to earlier times ($\ll 1$ h). An extreme case was NOAA-11. It had drifted about $3\frac{1}{2}$ h since its launch in September 1988 until July 1994 [*Christy et al.*, 1998]. It continued drifting until it could be used as a morning satellite in 1997, as visible in Figure 3.7, [*Vinnikov and Grody*, 2003].

In the case of a perfectly sine shaped daily temperature variation, this effect would cancel out itself because the curve increases with the same magnitude as it decreases a half wavelength later. But the daily temperature reaches the maximum above rural areas in the early afternoon and above maritime ones some hours later. Therefore, a larger temperature trend could be observed above oceans than above continents. The minimum is generally reached in the early morning, shortly before sunrise.

The point is that landmasses heat up and cool down much quicker than the atmosphere above it during a day, what might cancel a part of the trend [*Christy et al.*, 1998]. This increases their proportion on the net radiation output of the atmosphere. Mountain ranges (e.g. Alps) and high elevated plateaus (e.g. Tibet) show similar error characteristics. Due to the low density, the surface warming and cooling predominates the signal, which introduces an anharmonic diurnal cycle of the emission at the top of the atmosphere. The difference between the morning and evening temperature is much smaller than the difference between the early afternoon and late night temperature, because of the relatively low insulation at that time.

This is the reason why a shift of the observation time (diurnal drift) introduces a

3 Microwave Emission Measurements

spurious temperature trend. This can be detected, if a significant trend signal establishes, while the standard deviation of the anomaly time series increases. The correction relative to the reference time series is supposed to solve that problem [Christy *et al.*, 1998].

4. **Bias:** A further bias can still remain due to different calibrations of the MSU instruments at the surface [Christy *et al.*, 1998]. The mean difference between two satellites is determined for all days, which pass the T_{bias} criterion. This is done for all simultaneously operating satellites to receive the bias of the zonal mean anomaly time series of each satellite relative to the reference climatologies.

There are quite a lot of biases in the MSU observations, which are corrected after the reference annual cycle has been removed from the temperature measurements. To summarize, the median filter treats sampling errors and weather anomaly effects. The disturbing annual cycles, which originate from temperature variations of the hot target, are reduced as well as spurious warming trends, which arise from diurnal drifts of the orbiters.

3.5 Trend Results and Discussion

3.5.1 Received Temperature Trends

In the previous section, bias removals in radiometer measurements was discussed and how they are removed. This section deals with the trend results and the discussion about them. After the MSU measurements had been corrected and merged to continuous monthly mean temperature time series, trend analysis of the troposphere and of the stratosphere could be started. Although a climate warming has already been observed and proved in many cases [Solomon *et al.*, 2007] and (Section 2.3), the first trend results did not coincide with that. This circumstance caused a big controversy about the climate warming and the interpretation of MSU measurements.

The MSU processing center UAH found that the temperature of the mid troposphere has increased by about 0.01 K/decade between 1979 and 1998 [Christy and Spencer, 2003]. They estimated an error range of ± 0.05 K/decade after comparing their data with radiosondes, which consist of a set of quality controlled temperature measurements.

In general, the UAH team used radiosonde observations as a reference for temperature retrievals to improve the efficiency of bias reduction and the quality of the merging procedure, as described by Spencer *et al.* [1990]; Spencer and Christy [1992]; Christy *et al.* [1998]. But radiosondes are spatially not well distributed and show inhomogeneities in their time series [Thorne *et al.*, 2005]. Every radiosonde consists of a different set of instruments and goes up in isolated regions and describes various trajectories. MSU provides homogeneous global measurements, which can be provided with one radiometer instrument. Additionally the radiosonde records were calculated to MSU equivalent brightness temperatures with the weighting functions. Therefore it seems to be problematic to use radiosondes to

improve the MSU radiometer outputs, as mentioned by *Santer et al.* [2003].

The second main processing center of MSU measurements is RSS [*Mears et al.*, 2003; *Wentz and Schabel*, 1998]. Contrary to UAH, RSS applies a multiple regression model. This includes all data, which originate in overlapping periods of two NOAA satellites. Additionally RSS has not accommodated its results to radiosonde based observations [*Santer et al.*, 2003]. Therefore, RSS probably found a slightly higher mid tropospheric warming than UAH (0.1 K/decade globally between 1979 and 1998).

The zonal mean anomaly trends are visualized in Figure 3.9. TMT shows a net cooling at the Southern high latitudes ($\geq 50^\circ\text{S}$) and a warming of about 0.2 K/decade in the mid latitudes and in the tropics, which increases up to 0.4 K/decade in the Northern high latitudes. There is almost no difference between rural and maritime regions. Above arid and continental areas the trend is slightly higher than elsewhere, but that is also valid for the low-latitude Atlantic. The TTS does not show a homogeneous pattern but is consistent with TMT and TLS since it includes contributions from the troposphere and the stratosphere. Generally, the TTS trend varies between ± 0.1 K/decade and reaches values above 0.5 K/decade in the Northern high latitudes. The lower stratosphere shows generally a strong cooling with a minimum of ≤ -0.5 K/decade at 35°S and 43°N . Between those latitudes the temperature trend increases up to about -0.25 K/decade. The southern high latitudes show a very strong cooling, while the northern ones show only a slight cooling. Interesting is that the southern mid latitudes show an irregular pattern of slight warming and strong cooling (comparable with TTS).

Trend results from the Parallel Climate Model (PCM) suggest also a global warming of 0.07 K/decade for the same period, which is not significantly different from the RSS MSU trends. UAH complained that the model excludes the extraordinary warm El years, what would require further analysis [*Christy and Spencer*, 2003]. Uncertainties arise due to the chaotic behavior of the atmosphere, which can not be represented in a 3-dimensional global model with an infinite precision, because small scale processes must be quantified and large ones summarized and expressed as boundary conditions. Nevertheless PCM could simulate the statistical characteristics of an El Niño event.

3.5.2 Stratospheric Influence on TMT

The results of RSS and PCM deviate significantly from the observed warming trend at the surface (0.17 K/decade), as described by *Hansen et al.* [2002] and by *Jones and Moberg* [2003].

A good explanation for this discrepancy gives the weighting function of the mid troposphere, which extends far up into the stratosphere. Since the layers are weakly connected due to rare air exchanges, they can experience different temperature trends. Therefore the layers in the stratosphere may have a disturbing effect on the TMT-trend [*Fu et al.*, 2004]. A strong cooling could be observed in the lower stratosphere (between -0.5 K/decade and -0.9 K/decade) from radiosonde and MSU based measurements. The stratosphere is cooling because less terrestrial radiation penetrates through the troposphere. Additionally, parts

3 Microwave Emission Measurements

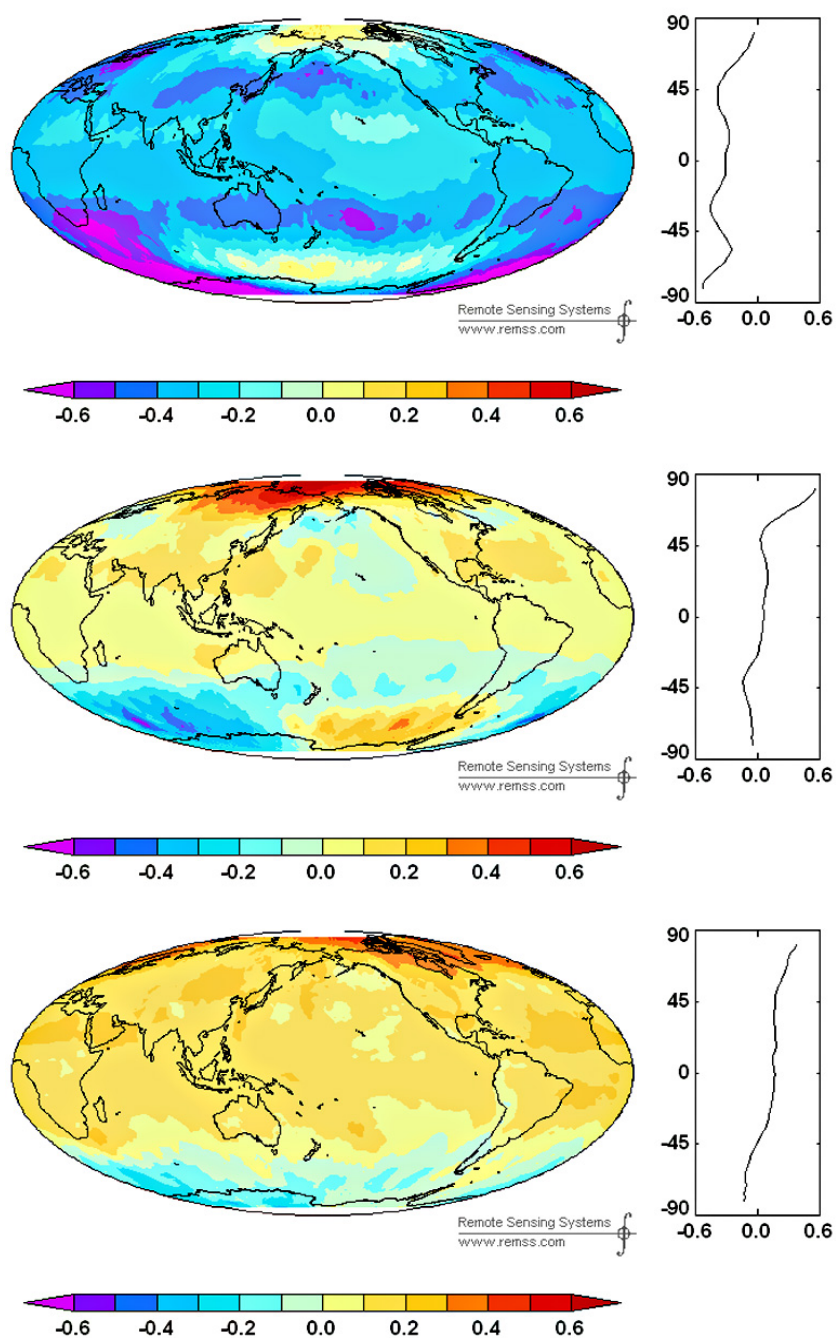


Figure 3.9: The observed RSS MSU-AMSU trends per decade of the monthly mean TLS (top), TTS (middle) and TMT (bottom) brightness temperatures between 1979 and 2006. The data are provided on a global $2.5^\circ \times 2.5^\circ$ grid. The right panel represents the temperature trends as a function of latitude, which are also given in K/decade [Solomon *et al.*, 2007].

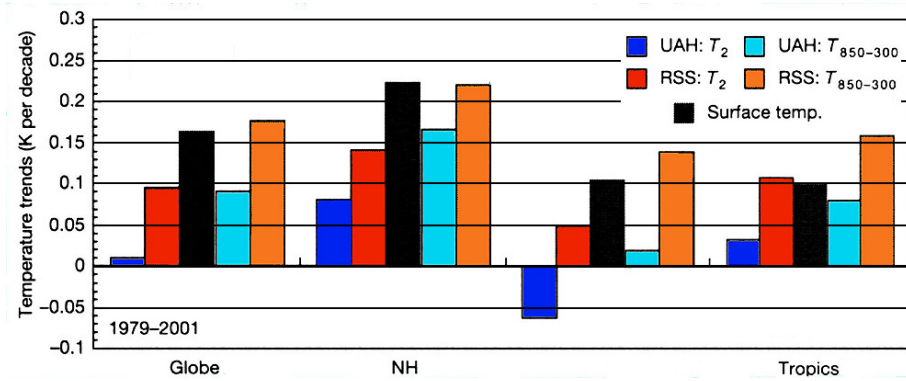


Figure 3.10: The observed MSU zonal and global mean Temperature trends of the mid troposphere from RSS and UAH in comparison to the surface based temperature trend before and after the correction of the stratospheric influence (adopted from *Fu et al.* [2004] and modified).

of the ozone layer broke down due to CFC emission in the seventies and eighties and that caused even less absorption.

85 % (or $\frac{5}{6}$) of the TMT signals arise in layers below 200 hPa, which is the troposphere [*Fu et al.*, 2004]. If the stratosphere (above 200 hPa) cools at 0.8 K/decade and the troposphere warms at e.g., 0.16 K/decade, then the TMT trend would decrease to zero. Conversely, the troposphere influences TLS much less, as it is visible in Figure 3.4 and 5.4.

To remove the stratospheric impact, *Fu et al.* [2004] have applied a least-squares regression analysis on 87 well proved radiosonde profiles, which provide temperature anomalies between 1958 and 1997, to receive the contributions of TMT and TLS on the free tropospheric layer between 300 hPa and 850 hPa.

$$T_{850-300} = a_0 + a_2 TMT + a_4 TLS \quad (3.12)$$

This equation describes the free tropospheric temperature ($T_{850-300}$). For the global mean the coefficients are 1.156 (a_2) and -0.153 (a_4). The effective weighting function of that layer behaves analogously to the free tropospheric temperature. It is 15 % larger than the maximum of the TMT weighting function, but it becomes negative above 100 hPa [*Fu et al.*, 2004]. This is supposed to cancel the stratospheric influence.

Therefore, the RSS tropospheric global trend increased up to 0.18 K/decade, which is 1.1 times larger than the surface trend (0.17 K/decade). The analogous UAH trend raised up to 0.09 K/decade, as visualized in Figure 3.10. The uncertainty of these results is quite large due to the shape of the effective weighting function ($\pm 0.09^\circ$). Therefore the UAH trend is insignificantly different from the one of RSS [*Neu*, 2005]. The global mean temperature trend ratio between surface and troposphere confirms the RSS result.

GCM¹³ model results showed a ratio of 1.2 between them. The analogous tropical ratio is even larger, 1.54 (for more detailed information apply *Hansen et al.* [2002]; *Hegerl and Wallace* [2002]), what is more or less confirmed by the RSS free tropospheric tropical av-

¹³GCM ... Global Circulation Model

3 Microwave Emission Measurements

erage (Figure 3.10). The tropical atmosphere should warm faster than the underlying surface because of the moist adiabatic temperature gradient and the permanent convection there. Water evaporates at the surface and raises latent heat up into the free troposphere, where it is released due to condensation. As simulated in the GCM, the northern hemisphere experiences a higher tropospheric warming than the southern one. Reasons for that are the distribution of land and ocean and the high heat capacity of water in comparison to soil. Land masses warm up quickly and heat can only be transported by turbulences, advection and convections. In maritime regions a high amount of heat is also stored by water and transported into the deep ocean. Therefore the atmosphere above them is not heated up by the same amount as the atmosphere above the rural areas.

Spencer et al. [2006] criticized the theory of *Fu et al.* [2004]. They argued, that the vertical trend distribution is not well known. Therefore it might be possible to see stratospheric cooling as tropospheric warming if the coefficients are set too large. UAH compared the results with temperature profiles from radiosonde. This institute argued that the coefficients remained the same after removing the trend from the radiosonde data. This implies that the prime source originates in the annual variability and not in the temperature trend. Another, but a critical, point is the time stability. Trials were attained with different sets of radiosonde data. There, a_2 varied between 0.944 and 1.129. The results depend on the data set and also on the time interval (range: 1979 until 1993 or until 2003) .

3.5.3 Diurnal Drift Correction

Another analysis procedure considers the diurnal drift problem. For that the satellite data are fitted to a model function, which includes the time of observations [*Vinnikov and Grody*, 2003]. According to that, the measured temperature is a mixture of the diurnal temperature variation and the trend, which is a function of the time of a day (i.e. e.g. 3 a.m., 6 p.m.). This enables to distinguish between the trend of the day and the trend of the night. Differences may arise due to e.g. environmental changes [*Solomon et al.*, 2007]. The measurements of each overlapping period (simultaneous observations of two MSU orbiters) was applied to determine the Fourier coefficients of the model, which is supposed to minimize the inter-satellite bias on the one hand and to give the trend as a function of time on the other hand. The result of this model was, that the mid troposphere warmed with a rate of 0.26 K/decade, which is by one third larger than the analogous surface value. The trend is larger in mid summer than in winter. It is also larger during daytime than during night and ranges between 0.35 K/decade and 0.20 K/decade [*Vinnikov and Grody*, 2003].

Vinnikov and Grody [2003] have explained the difference between their trend and the trend from UAH and RSS with the synchronous elimination of the instrumental bias and the temperature fluctuation of the hot target. Additionally, the bias becomes smaller due to different gaps filling methods.

But there is still a stratospheric influence on the signal, as mentioned by *Fu et al.* [2004]. If one assumes a stratospheric cooling of 0.5 K/decade, the TMT trend would increase up

to 0.33-0.37 K/decade. This is twice the surface trend and exceeds the results of various models by far (Section 1.4.). The reason for this discrepancy can either be the stratospheric correction, which has an uncertainty due to the effective weighting function, or the model scheme, which could not eliminate all biases.

Anyway, without the stratospheric correction, the global average TMT trend is already 1.6 times larger than the surface trend. This is supposed to occur only in tropical regions¹⁴, where more water vapor condenses in the troposphere due to a higher rate of evaporation at the surface.

3.6 RSS Temperature Retrieval

The scientific group of RSS developed an alternative processing scheme of the radiometer measurements with the aim to determine and reduce the biases more efficiently. RSS uses the same calibration scheme as UAH (digital counts, hot target correction, limb correction, ...) but different diurnal drift correction and merging procedure. To compute the diurnal temperature anomalies of each footprint, RSS has applied the results of the NCAR community diurnal cycle model, which is based on a 5 years run [Kiehl *et al.*, 1996]. From this model follow the first four coefficients of the Fourier series, which are enough to represent the diurnal cycle. The first one vanishes since the satellites measure the radiation with a delay of 12 h [Mears *et al.*, 2003].

The smallest diurnal cycle errors arise over maritime regions. They have an amplitude of

¹⁴A result from the GCM models

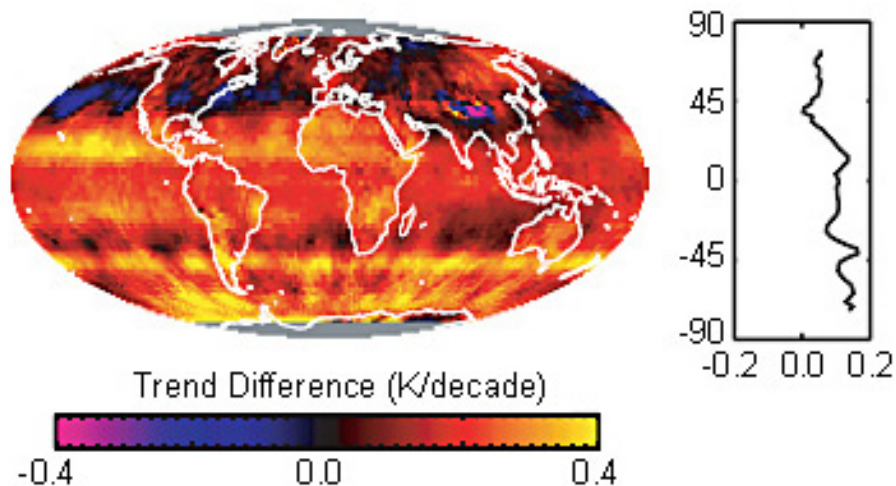


Figure 3.11: The difference between the UAH and the RSS TMT trend on a $2.5^\circ \times 2.5^\circ$ grid (left) and averaged on a zonal scale (right) [Mears *et al.*, 2003].

3 Microwave Emission Measurements

Source	Oceans	Lands	Total
<i>MSU - RSS</i>	0.098	0.087	0.097
<i>MSU - UAH</i>	-0.011	0.050	0.009

Table 3.1: The RSS and UAH TMT temperature trends are listed here for the period from 1979 to 1998. The trends in K/decade represent global averages of all oceans, of all continents, and of the total Earth.

≤ 0.5 K and change slightly from nadir to limb, what indicates an atmospheric origin of the diurnal cycle. The high heat capacity of water shifts the time of the temperature maximum into the late afternoon and dampens the diurnal temperature amplitude. Over the rural regions, surface heating and radiative cooling dominate the diurnal cycle. Therefore, the amplitude decreases from nadir to limb [Mears *et al.*, 2003].

RSS fitted all MSU measurements to a reference time and corrected the bias similar to UAH. In fact, due to the diurnal drift correction, RSS increased the global TMT trend by 0.03 K/decade in comparison to UAH, while the trend above oceans increased much less than over the continents (Table 3.1).

But the main trend difference between RSS and UAH arose due to different merging procedures. RSS applied all overlapping periods of more than five days, with the same weight to receive the target factors and biases. In comparison, UAH has only regarded overlapping periods longer than 60-120 days and therefore disregarded the total NOAA-9 time series. Despite the big differences between the UAH and RSS results, they show a similar zonal shape. They have the strongest warming over the continents in the Northern hemisphere with the maximum at 40°N. Their trends show a minimum at 10°N, where UAH received a slight cooling, and a southern maximum at 30°S, which is smaller than the northern one, as shown in Figure 3.11. Over the southern oceans and Antarctica, both show a cooling of the troposphere but with a difference of ~ 0.2 K/decade. The tropical oceans also contain large discrepancies with a belt like maximum at 15°N. The biggest agreements are found above 50°, which has to do with the high availability of radiosonde observations (Figure 3.11).

All in all, it was not a big deal to measure the temperature of the free atmosphere with MSU. It was much more difficult to produce a consistent and homogeneous temperature time series, since problems arose due to the temporal unstable satellites and the calibration scheme against a hot target, which induced an error relative to other satellites. Therefore, different retrieval procedures led to different results.

4 Radio Occultation Measurements

A new method for remote sensing of the Earth's atmosphere was tested in 1993, the so-called RO¹ method. It is an active limb sounding technique and needs at least two satellites. The GNSS² satellites at about 20000 km height emit radiowaves at two frequencies. Phase and amplitude of the signal are observed by a high precision receiver on a low earth orbiter at circa 400-800 km height (Figure 4.1 and Figure 4.5). During the movement of the LEO³ satellite the atmosphere can be almost vertically scanned from the surface to the top (rising occultation) or vice versa (setting occultation). With the phase delay⁴ it is possible to determine the refractive index and profiles of pressure, temperature, electron density, neutral density, and geopotential height.

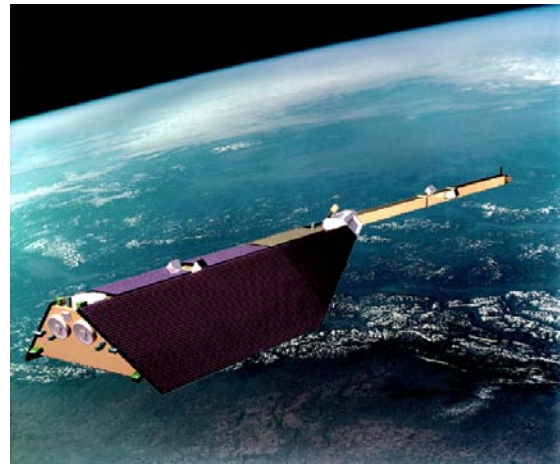


Figure 4.1: An artistic plot of the CHAMP satellite in space <http://www.gfz-potsdam.de>.

4.1 Development of this Technology

The RO technology works with similar methods as the seismology, which uses the Wiechert-Herglotz-method to determine the density structure of the solid Earth. The observed travel time shift corresponds to the arc distance between transmitter and receiver, if the Earth shows a spherical symmetric structure, which leads to continuous velocity changes with depth, and refraction happens without reflection at the interfaces. Radio waves are sent through the atmosphere. From the phase delay of the waves it should be possible to retrieve the arc distance and the refractivity [*Phinney and Anderson, 1968*].

Originally, RO was developed to measure the atmosphere of other planets. It could be

¹Radio Occultation

²GNSS ... Global Navigation Satellite System

³Low Earth Orbiter

⁴actual phase relative to vacuum phase

4 Radio Occultation Measurements

largely observed that the radio link to a spacecraft varies when it moves behind a planetary atmosphere. After first successful trials to gather informations about the atmosphere of Mars via radio occultation measurements, which were carried out with the satellite Mariner-IV in 1965 [Fjeldbo and Eshleman, 1965], several missions to other planets followed. The ionosphere and the neutral atmosphere of Venus were observed some years later [Fjeldbo et al., 1971]. The atmospheric properties of Jupiter and its moon Io were determined, when Pioneer-10 passed behind them [Kliore et al., 1975]. More information about Jupiter and Saturn, Titan, Uranus and Neptune were provided by several Voyager missions in the eighties and early nineties, as described by e.g., Lindal et al. [1983, 1985]. For the Earth, radio occultations have not been that interesting for a long time, because the location of the satellites could not be measured exactly enough, to provide high quality observations of the atmosphere. But it became realistic after the installation of the U.S. GPS⁵ system in the early eighties. Gurvich and Krasil'nikova [1990] created a concept how to observe the terrestrial atmosphere with the RO method and several years later it was tested with the GPS/MET proof-of-concept mission under the conduction of the University Cooperation for Atmospheric Research in Boulder, Colorado. A satellite named Microlab-1, was launched in April, 1994 during the GPS/MET experiment. It showed successfully the performance of the radio occultation measurements, as described in the articles from e.g., Ware et al. [1996] and/or Kursinski et al. [1996]. The data impressed with an accuracy of under 1 K and a high vertical resolution of 500-1500 m. Like the radiometer measurements the occultation method works during all weather events. Major steps toward a continuous measurement time series were done with the US-Argentinian SAC-C satellite (for receiver testing) but foremost with the US-German CHAMP⁶ satellite. They used the new TRSR-2 and TRSR-3 receivers, which have been developed at the NASA's Jet Propulsion Laboratory [Gobiet, 2005]. In this thesis only the CHAMP temperature time series are applied. Also the GRACE⁷ mission, which started in 2002 [Wickert et al., 2005], provides RO observations. GRACE and also CHAMP primary focus on other atmospheric and seismic topics, as described on the GFZ homepage, www.gfz-potsdam.de. Nevertheless they provided the first continuous longer time series. Further steps are made by the Taiwan-U.S. mission COSMIC⁸. The issue is to increase the horizontal data resolution and to provide a continuous data stream. COSMIC e.g. consists of six micro-satellites, which carry the integrated GPS occultation receiver and increase the global coverage of the occultation events up to 1000 km. It is supposed to measure about 900 up to 3000 occultations per day, while the number depends on the realization of setting events and on hardware, software, and retrieval advancements [Gobiet, 2005]. The resolution gaps in the equatorial and subtropical regions, as shown in Figure 4.3, can additionally be compensated by the Brazilian EQUARS⁹ satellite mission. The European

⁵GPS ... Global Positioning System

⁶CHAMP ... Challenging Mini-satellite Payload

⁷GRACE ... Gravity Recovery and Climate Experiment

⁸COSMIC ... Constellation Observing System for Meteorology

⁹EQUARS ... Brazilian Equatorial Atmosphere Research Satellite

METOP satellite, which is operated by EUMESAT¹⁰, was launched in October 2006, with the new GRAS¹¹ receiver on board. This will be the first "operational" satellite for RO and is supposed to measure until 2020 (METOP-A to METOP-C with 5 year lifetime each). But one problem still remains. The water content of the atmosphere can not be extracted by single RO measurements. Therefore background information is applied from e.g., ECMWF¹² (Section 4.5.5). Maybe this problem can be solved by further satellite missions and by a new measurement concept, which includes higher frequencies for water vapor [Kirchengast and Hoeg, 2004]

4.2 Signals, Constellation and Resolution

The signals, used by the RO system, come from the U.S. Global Position System. The well known GPS system consists of 28 satellites. They are set in 6 circular orbits in a height of 20185 km with an inclination of 55° relative to the equator [Hofmann-Wellenhof *et al.*, 1992]. For one orbit they need almost 12 hours. 2008 the European GALILEO will follow as a further signal source.

The GPS signals are transmitted to a receiver on a LEO satellite at 300 km to 500 km

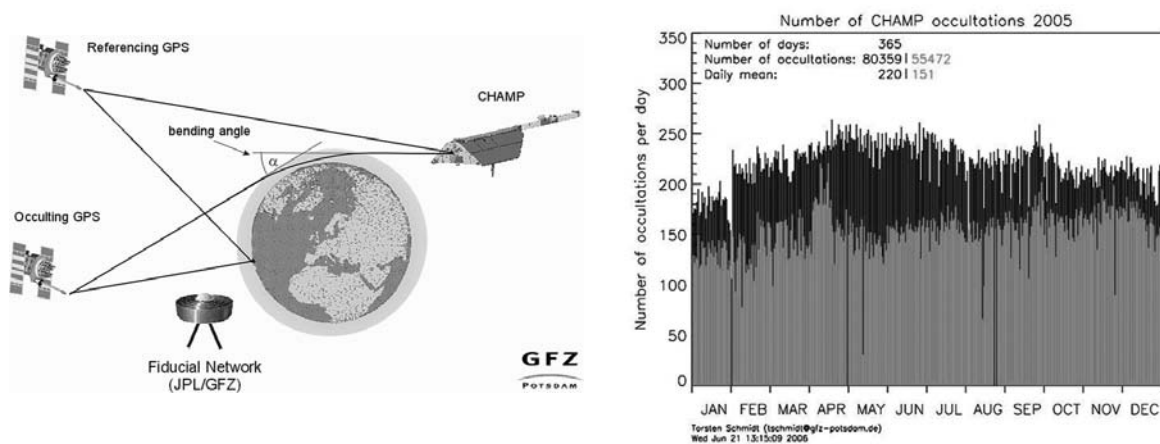


Figure 4.2: This figure shows the principle construction of the GFZ RO measurements (left) and the number of daily received occultations in comparison to retrieved atmospheric profiles at GFZ (right) for the year 2005 <http://www.gfz-potsdam.de/pb1/op/champ>.

height, which orbits the Earth in 90-116 min. The high inclination relative to the equatorial plane guarantees a good and homogeneous geographical distribution of measurements (Figure 4.3). Only in low latitudes gaps remain after one month of observations, as visi-

¹⁰EUMESAT ... European Meteorological Satellite Organization

¹¹GRAS ... GNSS Receiver for Atmospheric Sounding

¹²ECMWF ... European Center for Medium-Range Weather Forecast

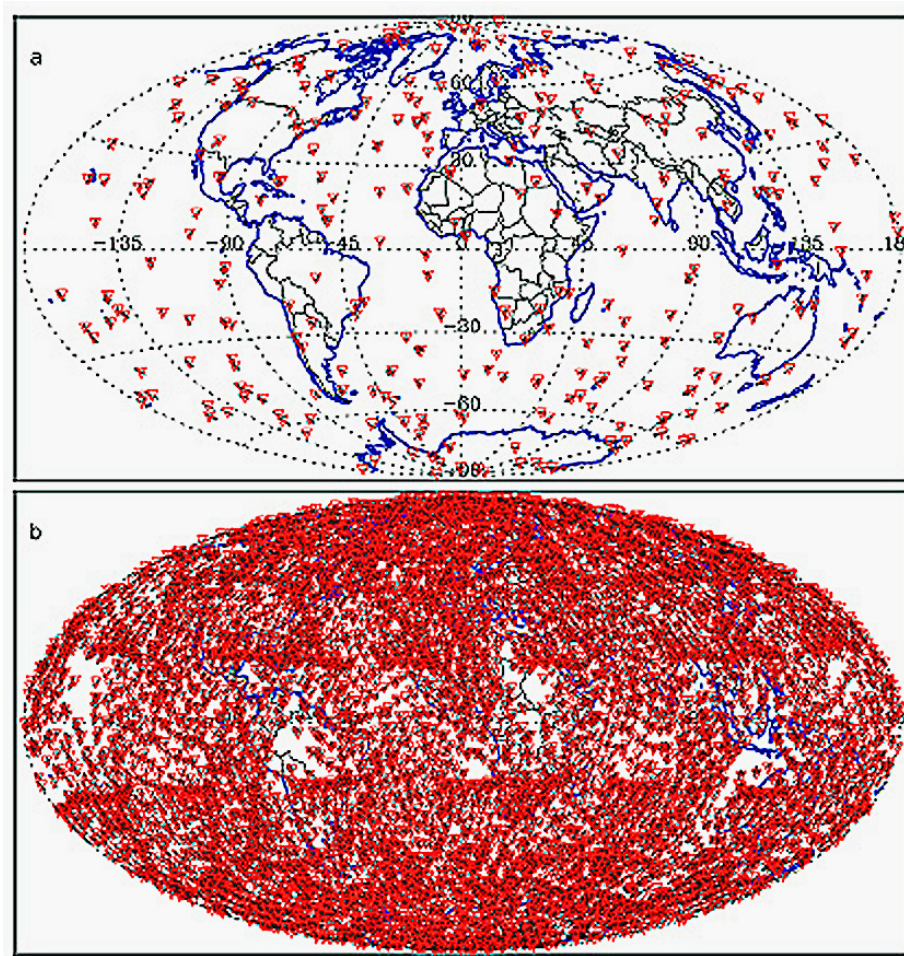


Figure 4.3: The geographical distribution of occultations received by the CHAMP satellite (only setting events) after (a) one day (279 events) and (b) one month (8649) events [Gobiet, 2005].

ble in Figure 4.3. The resolution depends on the antenna¹³ and on the receiver software, which limits the number of recorded events. An occulting event takes place, whenever GPS signals pass the LEO satellite. Each receiver records between 250 and 300 events per day. Due to some reasons, the number reduces down to 180¹⁴, as visualized in Figure 4.2 [Gobiet, 2005]. The satellite carries two receivers: one aft looking antenna for setting events and one front looking antenna to record rising events. Actually, only the first one is technically demonstrated.

Actually RO applies two GPS signals. Those are carrier frequencies in the L-band¹⁵, which are multiples of the precisely controlled atomic clock frequency¹⁶. Three binary pseudo

¹³antenna defines the radius of view

¹⁴results in an efficiency rate between 60 % and 70 %

¹⁵Link2-(L2): 1.228 GHz and Link1-(L1): 1.575 GHz

¹⁶atomic clock frequency: ν_0 is 10.23 MHz

random noise (PRN) sequences modulate the signal with two codes, which are needed to determine the phase of the passing signal. The coarse acquisition (CA) PNR code overlays L1 with $v_0/10$ and the precise (P) code overlays both signals with v_0 [Gobiet, 2005]. The public user usually applies the P code for his navigation system, which can give the position with a precision of 100 m.

Additional clock offset data (reference signal) and ephemeris data are sent along with the navigation message. The transmission time arises from comparisons with the clock on the transmitter. This is crucial for the clock calibration, which is more accurate than necessary. Since only the short term clock stability impacts the accuracy of the RO technique, it can be treated as a "self calibrating" and as a long term stable method.

4.3 Data Processing

In this study, RO data from the German-U.S. CHAMP RO Experiment are used, a project of the Geoforschungs Zentrum (GFZ) Potsdam [Reigber *et al.*, 1995]. A low Earth orbiting satellite was launched with the Russian COSMOS rocket in summer 2000. It is 8.3 m long (including the 4.04 m boom) and orbits the Earth at 454 km height with an inclination angle of 87° relative to the equatorial plane, as visible in Figure 4.4 [Wickert, 2002; Wickert *et al.*, 2004, 2005]. Several orbit lifting maneuvers have been carried out since then to compensate the atmospheric drag, which permanently lowers the orbital height.

CHAMP is supposed to measure Earth's gravity and magnetic field up to 2009. Beside that it can perform limb soundings of the ionosphere and neutral atmosphere. The satellite consists of the so-called "Black Jack" (TRSR-2) GPS flight receiver, which contains an aft looking helix antenna (built by JPL), and several other instruments like a magnetometer, an accelerometer, a star sensor, a laser retro reflector, and an ion drift meter, as visualized in Figure 4.4. More detailed information about the CHAMP project are available at the GFZ homepage: www.gfz-potsdam.de.

Since September 2001, CHAMP provides a continuous RO data stream. Six months later, it reached its maximum efficiency of 240 occultations per day. 65 % of them are used to

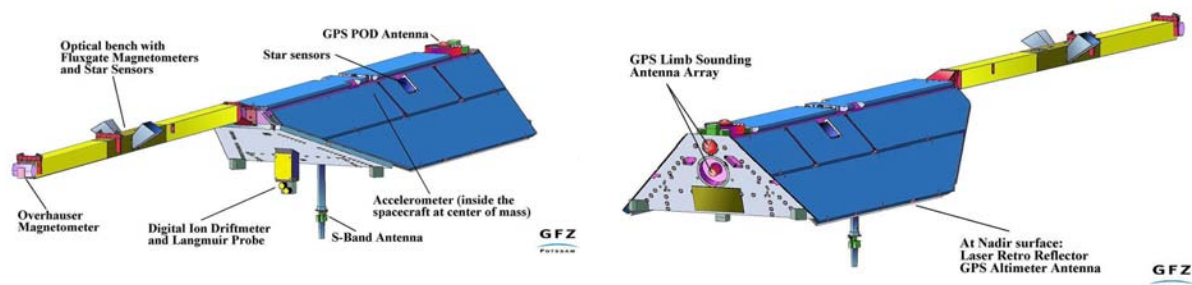


Figure 4.4: This is the construction of the CHAMP satellite, its subsystems and instruments <http://www.gfz-potsdam.de/pb1/op/champ>.

4 Radio Occultation Measurements

derive atmospheric profiles. The accuracy is quite high. The temperature bias lies below 0.5 K in the upper troposphere and between 1 K and 3 K in the lower stratosphere.

The GFZ RO ground infrastructure, as shown in Figure 4.5, enables data analysis with a delay of five hours between the provision of atmospheric profiles and the corresponding measurements. This is an important point, which has to be improved in the future since NWP models usually require a delay of less than three hours between measurement and data availability.

4.3.1 Data Acquisition

For RO missions it is necessary to have a ground infrastructure beside the space components. A down-link station near the poles (polar receiving station) enables data downloads from CHAMP in the desired amount and quality and avoids data loss. Beside this, GFZ uses 40 GPS ground stations to get precise orbit information, which is needed to correct the clock errors of the satellites. It depends on the quality of the clocks if it has to solve for one or two clock imprecisions. The common way for solving that is to apply the link between the LEO satellite and one occulting and one reference GPS satellite and to use their link to the ground station [Hajj *et al.*, 2002; Wickert, 2002].

The clock correction data from the GPS ground network are applied to determine the ex-

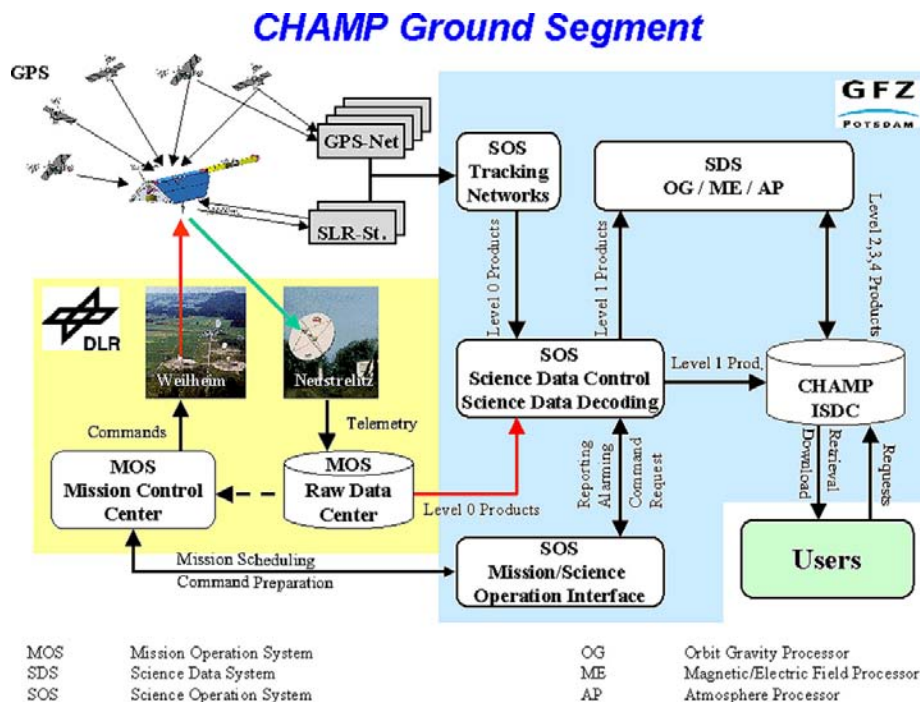


Figure 4.5: The main components of the CHAMP infrastructure, necessary to supply institutes around the Earth with data received from radio occultation measurements <http://www.gfz-potsdam.de/pb1/op/champ>.

act orbits of the GNSS and LEO satellites [König *et al.*, 2002] for the direct "vacuum"¹⁷ pathway. This is an important part of the ground infrastructure ("precise satellite orbits" \Rightarrow Figure 4.5). The information is sent to data processing facilities, which compute the refractive index and the vertical temperature and pressure profiles in a further instance, as described in the next sections.

The operational weather services supply CHAMP with additional background informations. ECMWF e.g. simulates the state of the atmosphere for precise weather forecasts. Actual weather states are stored in the archival data center. Institutes and data centers use them for comparisons and further analysis.

4.4 Physical Concept

As mentioned, RO signals are radiowaves, which have a higher wavelength than the microwaves¹⁸. The wavelength is inversely proportional to frequency and energy. In this spectrum the waves are refracted or scattered when passing the atmosphere. Absorption occurs at higher energy levels, what allows radio-waves to pass through the atmosphere. Basically the propagation of electromagnetic waves can be expressed by the Maxwell Equations [Demtröder, 1999], which describe the fundamental classical electrodynamics.

$$\nabla \mathbf{D} = \rho_{el} \quad (4.1)$$

$$\nabla \times \mathbf{H} = \mathbf{j} + \frac{\partial \mathbf{D}}{\partial t} \quad (4.2)$$

$$\nabla \mathbf{B} = 0 \quad (4.3)$$

$$\nabla \times \mathbf{E} = -\frac{\partial \mathbf{B}}{\partial t} \quad (4.4)$$

The source of a dielectric displacement (\mathbf{D}) is always a (net) charge density of a material (ρ_{el}). The charge dipoles within a matter cancel out themselves and contribute not to the material charge. The neutral atmosphere has obviously no charges and is an electric isotropic medium. In the ionosphere, charges and plasma interact with EM waves and Earth's magnetic field. Therefore the ionosphere becomes anisotropic and \mathbf{D} varies.

Magnetic Induction (\mathbf{B}) develops only in connection with an electric field and consists of both poles, which demands that the same number of field lines leaves and enters an arbitrary plane. Therefore the magnetic field is constant. It has no sources and the gradient becomes zero, as expressed in the Gauss law. Magnetic fields can either be generated by flowing currents within a conductor or by changing electric fields, which can be seen in a condenser.

Equation 4.4 (Faraday's law) describes the induced electric field due to varying magnetic fields. It is proportional to the rate of change of the magnetic field through a coil. The

¹⁷the shortest distance between the LEO and the GPS satellite

¹⁸RO uses wavelengths at about 19 cm and 24 cm

4 Radio Occultation Measurements

change can be caused by rotation of the electric circuit in a magnetic field or by changing currents. To solve the Maxwell equations it is necessary to describe the dielectric displacement and the magnetic induction with the current density¹⁹ which correspond to material properties within an electromagnetic field. In a dielectric medium, an installation of an electric field causes electrons to separate from atomic nuclei and the development of a dipole moment. The total charge density can be seen as the sum of free and bounded charges (ρ_{bound}), while the number of bounded charges depends on the rate of the polarization (\mathbf{P} - mean electric dipole moment per volume) [Jackson, 1983].

$$\rho_{\text{bound}} = -\nabla \mathbf{P} \quad (4.5)$$

Since equation 4.1 describes the net number of charges, while the total number of charges can be expressed via Poisson's law as a function of the electric field strength (\mathbf{E}) and the permittivity of vacuum (ϵ_0), one can get the connection between \mathbf{D} and \mathbf{E} and analogously between \mathbf{B} and the magnetic field strength \mathbf{H} .

$$\nabla \mathbf{E} = \frac{\rho_{\text{total}}}{\epsilon_0} \quad (4.6)$$

$$\nabla \mathbf{D} = \rho_{\text{el}} = \rho_{\text{total}} - \rho_{\text{bound}} = \nabla \mathbf{E} \epsilon_0 + \mathbf{P} \quad (4.7)$$

$$\mathbf{D} = \epsilon_0 \mathbf{E} + \mathbf{P} \quad (4.8)$$

$$\mathbf{B} = \mu_0 \mathbf{H} + \mathbf{M} \quad (4.9)$$

The magnetic induction is analogously to the electric displacement a function of the magnetic field strength, the permeability of vacuum (μ_0) and the magnetic polarization (\mathbf{M}), which is the mean magnetic dipole moment per volume.

Every material increases the displacement and the induction, due to the specific dipole moments. In a homogeneous medium like Earth's neutral atmosphere the polarization is a linear function of the electric field strength and the electric susceptibility ($\hat{\chi}_e$), which degrades to a scalar. The term $(1 + \hat{\chi}_e)$ expresses simply the permittivity of a medium ϵ_r . In the case of a vacuum it is obviously one.

$$\mathbf{P} = \epsilon_0 \hat{\chi}_e \mathbf{E} \Rightarrow \mathbf{D} = \epsilon_0 \underbrace{(1 + \hat{\chi}_e)}_{\epsilon_r} \mathbf{E} \quad (4.10)$$

In the ionosphere $\hat{\chi}_e$ upgrades to a tensor of second order. Solar short wave radiation ionizes the molecules charges and currents. Therefore the layer becomes dispersive, i.e. refraction varies with the frequency of electromagnetic waves. This has to be considered, while computing the pathway of the signals. Measurements at two frequencies help to eliminate the ionospheric part of the refraction, which is a function of the pathway and atmospheric parameters like temperature and water vapor pressure.

The atmosphere is transparent at GNSS frequencies. This is a big advantage in comparison to microwaves, which are absorbed by several molecules (Section 2.2), which would lead to

¹⁹material and constitutive equations

a loss of the signals. The magnetic induction behaves similar to the electric displacement. The magnetic dipole moment is a function of magnetic susceptibility²⁰, permeability of vacuum and magnetic field strength.

$$\mathbf{M} = \mu_0 \hat{\chi}_m \mathbf{H} \Rightarrow \mathbf{B} = \underbrace{\mu_0 (1 + \hat{\chi}_m)}_{\mu_r} \mathbf{H} \quad (4.11)$$

Finally the current density (\mathbf{j}) can be expressed with Ohm's law as a function of the electric field and the conductivity ($\hat{\sigma}$), which is a matrix of second rank in anisotropic media, like the ionosphere. But it is negligible there, because of the low pressure (\rightarrow small charge density)

$$\mathbf{j} = \hat{\sigma} \mathbf{E} \quad (4.12)$$

The neutral atmosphere has principally no conductors and therefore $\hat{\sigma}$ vanishes. Now \mathbf{B} , \mathbf{D} (and \mathbf{j}) can be expressed as a function of the magnetic and electric field strength and inserted into the equations. The rotor of equation 2.2 and 2.4 and the vector identity relation $\nabla \times \nabla \mathbf{E} = \nabla(\nabla \mathbf{E}) - \Delta \mathbf{E}$ give the standard partial wave equations of \mathbf{E} and \mathbf{H} , from which the equations of electric and magnetic plane waves at location \mathbf{r} to time t arise after two integration steps.

$$\mathbf{E}_{\mathbf{r},t} = \mathbf{E}_0 * \exp i\left(\frac{2\pi}{\lambda} \mathbf{r} - 2\pi \nu t\right) \quad \mathbf{H}_{\mathbf{r},t} = \mathbf{H}_0 * \exp i\left(\frac{2\pi}{\lambda} \mathbf{r} - 2\pi \nu t\right) \quad (4.13)$$

\mathbf{H} and \mathbf{E} can be inserted into the partial wave equations (not shown here) to get the relation between the wave and material properties.

$$\frac{1}{\lambda^2} \mathbf{E} = \epsilon_0 \epsilon_r \mu_0 \nu^2 \mathbf{E} \quad \lambda \nu = c = \frac{1}{\sqrt{\epsilon_0 \epsilon_r \mu_0}} \quad (4.14)$$

This is the propagation velocity of electromagnetic waves in a medium with permittivity (ϵ_r). Since ϵ_r is larger than one, the velocity reduces relative to the vacuum, where the electromagnetic waves penetrate with the maximum speed²¹. The relation between c_0 and c defines the refractive index of a medium (n), which is known as the Maxwell relation.

$$n \equiv \frac{c_0}{c} = \sqrt{\epsilon_r} \quad (4.15)$$

Generally ϵ_r is a function of the frequency but is constant at GNSS frequencies. A further advantage of radiowaves is that the permittivity is not complex at those frequencies, which could result in complex refractivity fields.

The interconnection between refraction index and atmospheric parameters like temperature (T), dry air pressure (p_{dry}) and water vapor pressure (e) can be derived with the atomistic theory of matter. This is well described by *Foelsche* [1999] and references therein. In RO

²⁰ $\hat{\chi}$ is negligible in the total atmosphere

²¹ speed of light in vacuum: $c_0=299792458$ m/s

4 Radio Occultation Measurements

these parameters are used as a function of the refractivity (N). The relation between them and the refractivity is shown in the formula of *Smith and Weintraub* [1953].

$$N = (n - 1) * 10^6 \quad (4.16)$$

$$N = k_1 \frac{p_{\text{dry}}}{T} + k_2 \frac{e}{T} + k_3 \frac{e}{T^2} \quad (4.17)$$

$$N = k_1 \frac{p}{T} + k_4 \frac{e}{T^2} \quad (4.18)$$

The constants k_1 , k_2 and k_3 ²² have been experimentally derived by *Bevis et al.* [1994]. A further transformation gives the pseudo constant k_4 ($k_4 = (k_2 - k_1)T + k_3$). Then the total air pressure (p) can be taken with a small error [*Gobiet, 2005*]. This relation is widely used in RO data processing and gives the refractivity with an uncertainty of 0.02 % in dry and 0.5 % in wet air. Obviously, problems arise when e should be derived separately from temperature.

In the ionosphere things become more complicated because of the dispersive properties there. Close to the surface the typical bending angle ranges between 1 deg and 2 deg (about 20 mrad) and decreases exponentially with height, analogously to the air pressure. But above 30 km it increases again, due to ionization. The relation between refraction and the ionospheric properties is described by the Appleton-Hartree formula [*Budden, 1985*]. For GPS signals, it can be approximated to an equation of second order [*Bassiri and Hajj, 1993*], while the second order term has virtually no influence as well (only a small influence at daytime and during high solar activity) [*Syndergaard, 1999*] and is neglected in RO retrievals.

$$N_k = -C \frac{N_e}{v_k^2} - K \frac{B_{\text{par}} N_e}{v_k^3} \approx -C \frac{N_e}{v_k^2} \quad (4.19)$$

N_k is the ionospheric part of the refractivity of signal k , N_e the electron density, C a constant, K another constant and B_{par} the absolute value of Earth's magnetic field parallel to the wave propagation. The remaining first order term is proportional to the inverse square of the signal's frequency v_k and is removed by linear combining the two signals.

4.5 Temperature and Pressure Profiles

4.5.1 The Optical Path

The optical path (L_k) is expressed as a function of the refraction index (n) along the pathway (s). It increases with refractivity and follows Fermat's law of minimization of the optical pathway, which extends from one GPS to the LEO satellite. Generally electromagnetic waves are decelerated because $n \gg 1$. But in the ionosphere n decreases below unity and the ray becomes accelerated and bended away from Earth's center. This results in a change

²² k_1 : 77.60±0.05 K/hPa, k_2 : 70.4±2.2 K/hPa, k_3 : 3.739±0.01210⁵ K²/hPa

of the actual phase in comparison to the vacuum phase.

$$L_k = \int_{GPS}^{LEO} n ds \quad (4.20)$$

In most parts of the atmosphere spherical geometric optics can be applied for RO. The wavelength is small relative to the spatial extension and therefore the bending of wave fronts can be neglected [Gobiet, 2005]. There the waves behave like plane rays.

Small scale perturbations occur in some parts of the ionosphere and in the lower troposphere of the mid and low latitudes due to the high water vapor pressure, which raises rapidly the refraction index. This produces a multi path propagation signal and causes the RO retrieval to fail. In other words the phase change gives ambiguous informations about the actual pathway of the signal and the position of its source. Radio holographic methods [Gorbunov et al., 2003] like the canonical transform method and the full spectrum inversion technique [Jensen et al., 2003] were developed to solve this problem. Actually these methods increase the reliability of the lower tropospheric temperature retrieval.

This is the major thing in the RO. In fact, temperature and pressure distribution in the atmosphere influence the optical pathway of a signal, which is proportional to the bending angle (α). The atmosphere is supposed to have a spherical symmetrical field and therefore a symmetrical refraction field. Therefore the waves follow a curve-linear path and α can be related to n and be used to solve for the refraction field. It is much easier to measure the optical path as a function of the phase and amplitude with GPS receivers than to measure the bending angle directly with huge antennas.

This is the reason why the receivers measure the phase delay of the signal relative to the reference phase (Φ_k). While LEO sets down behind the atmosphere²³, the phase starts to change due to increasing distance and the atmospheric influence. The further setting progresses the lower layers of the atmosphere can be reached and the signal is more and more refracted. Since GPS transmits signals at a high time rate, the relative phase delay can be measured directly [Hajj et al., 2002].

$$L_k \equiv -\frac{c_0}{v_k} * \Phi_k = \gamma^V + \gamma^N + \gamma_k^I + C_{LEO} + C_{GPS} + r_k \quad (4.21)$$

The optical pathway follows from the constellation of the satellites, as shown in Figure 4.6. With the knowledge about the exact locations of the transmitting GPS and receiving LEO satellite one gets the direct vacuum path between them (γ^V i.e. S_0 in Figure 4.6) and also the clock errors (C_{LEO} and C_{GPS}), as described in Section 4.3. The extra optical path, which is a part of the total optical path, is caused by refraction in the neutral atmosphere (γ^N) and in the ionosphere (γ_k^I ²⁴) and by the receiver noise r_k .

²³Setting of LEO from GPS' point of view

²⁴signal k with frequency v_k

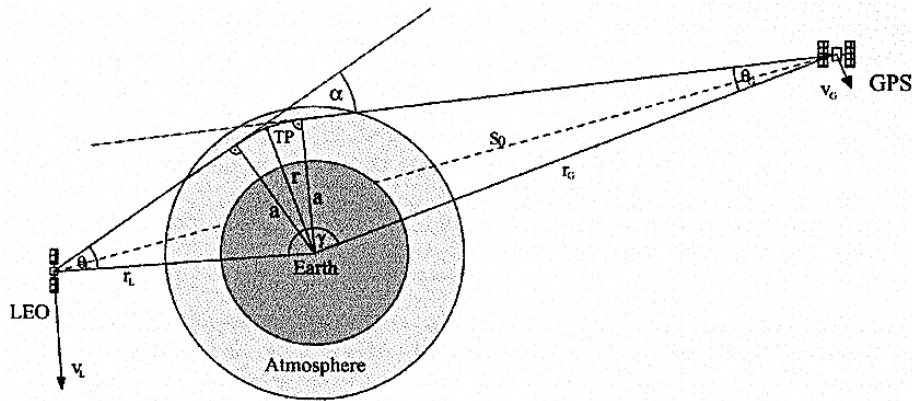


Figure 4.6: The geometry of a radio occultation event with the main parameters to retrieve the bending angle (s_0 is the vacuum path, a the impact parameter and r_G and r_L the orbit radii of the satellites) [Foelsche, 1999].

4.5.2 Bending Angle

The change of the ray direction with the ray path produces an extra optical path, which is a function of refractivity, or more precisely, a function of the bending angle (α). With the help of geometric optics, α can be derived from the combination of the angle between the LEO and the GPS satellite (γ) and from the ray directions from the satellites' point of view (Θ_G and Θ_L)²⁵ (Figure 4.6).

$$\alpha = \gamma + \Theta_G + \Theta_L - \pi \quad (4.22)$$

The angle γ follows from the satellite constellation, while the other angles must be derived, since the waves are sent homogeneously in all directions.

The atmosphere, where the ray has to penetrate through, is an approximately spherical symmetric refractivity field around the Earth's center [Born and Wolf, 1999]. This circumstance brings important simplifications [Foelsche, 1999; Gobet, 2005]. Thereafter, n varies only with the distance from Earth's center (r) but not with longitude or with latitude.

$$\mathbf{r} \times n(r)\mathbf{s} = a = \text{const.} \quad (4.23)$$

$$nr \sin(\phi) = a \quad (4.24)$$

This is the formula of Bouguer, which represents Snell's law in a spherical symmetric medium. The constant a is called the impact parameter and describes the normal distance of the ray to the center of refraction. A short description may give an explanation of this statement.

Assume a ray, which penetrates through three media with refractivity n_1 , n_2 , and n_3 and two interfaces (the ray crosses the interfaces at the points R_1 and R_2). The ray becomes

²⁵G is the synonym for GPS and L for LEO e.g., CHAMP

refracted at both interfaces and leaves them with the angles of reflection: β_1 and β_2 . Following Snell's law ($n \sin(\phi)$ is constant) the ratio between the angle of incidence and the angle of reflection is the same as the inverse ratio between the refractivity indices of the media at an interface. This relation is valid for waves, which behave like rays in a (spherical) homogeneous stratified medium or refraction field. The angles of incidence at point R_1 and at point R_2 can be easily associated with the sine law (trigonometry). [Foelsche, 1999].

$$n_1 \sin(\beta_1) = n_2 \sin(\alpha_1) \quad (4.25)$$

$$r_2 / \sin(\alpha_1) = r_1 / \sin(\pi - \beta_2) \equiv r_1 / \sin(\beta_2) \Rightarrow \quad (4.26)$$

$$n_1 r_1 \sin(\beta_1) = n_2 r_2 \sin(\beta_2) = a = \text{const.} \quad (4.27)$$

r_1 and r_2 are the distances of the points from Earth's center. Since the refractivity index of vacuum is unity, the total bending angle can be gained by inserting the orbital parameters of the satellites.

$$r_G \sin(\Theta_G) = r_L \sin(\Theta_L) \quad (4.28)$$

The bending angle is quite small and increases up to 1-2 deg if the ray passes low altitudes, where the water vapor impact becomes very strong [Kursinski *et al.*, 2000].

The third equation to solve the bending angle is the Doppler shift relation, which describes the frequency delay (v_d) due to the movement of the receiver relative to the transmitter.

$$v_d = \frac{v_G}{c_0} \frac{dL_k}{dt} = \frac{v_G}{c_0} (v_G s_G + v_L s_L) \quad (4.29)$$

$$v_d = \frac{v_G}{c_0} (v_L^r \cos(\Theta_L) - v_L^t \sin(\Theta_L) + v_G^r \cos(\Theta_G) + v_G^t \sin(\Theta_G)) \quad (4.30)$$

Distance from Earth's center and velocity of the satellites ($G \equiv \text{GPS}$ and $L \equiv \text{LEO}$) are well known, which are separated into radial and tangential components ($v_{L,G}^{r,t}$). s is the ray path and Θ implies the direction of the ray relative to the vertical height axis. The measured Doppler shift delay can be retrieved with a numerical iterative algorithm. It is proportional to the time derivative of the optical path, which results from the relative phase delay with time (equation 4.21). From the combination of the equations 4.22, 4.28, and 4.30 arises the bending angle α .

Some corrections have to be made for disturbing influences. Firstly, the Earth is rather an ellipsoid than a perfect sphere. Therefore, the retrieval error can raise up to 6 K near the surface, if the oblateness is neglected. Syndergaard [1998] has developed an ellipsoid approximation correction scheme, which could reduce the retrieval error below 0.1 K near the surface and to virtually zero above 8 km. He regarded the ellipsoid's curvature in the occultation plane to compute the velocities and positions of the satellites.

Secondary, the ionosphere produces a significant influence on the refraction, what is reduced by combining the two GNSS signals as mentioned above. The ionosphere is a dis-

4 Radio Occultation Measurements

persive medium and refracts the radiowaves in different ray paths. The refraction index, which is proportional to refractivity, (equation 4.20) is composed of an ionospheric and neutral atmospheric part. The ionospheric refractivity increases with the inverse square of the carrier frequency as presented in equation 4.19. That describes the measured optical path (L_k), which is affected by several influences (see: equation 4.21), along the ray path (S_k). The "linear correction of phase delays" scheme helps to analyse the ionospheric impact [Spilker, 1980] on the ray path. There the equation below has to be combined for both signals (L_1 and L_2) to receive the ionospheric contribution on the path length, which is approximately the same for both signals.

$$L_k(t) = \int_{LEO}^{GPS} \left(1 + \frac{N^{NE} + N_k^{IO}}{10^6}\right) ds = S_k - \frac{C}{10^6 v_k^2} \int_{LEO}^{GPS} N_e ds + \frac{1}{10^6} \int_{LEO}^{GPS} N^{NE} ds \quad (4.31)$$

$$L_c(t) = L_1(t) - \frac{C}{10^6 v_1^2} \int_{LEO}^{GPS} N_e ds \quad (4.32)$$

$$L_c(t) = \frac{L_1(t)v_1^2 - L_2(t)v_2^2}{v_1^2 - v_2^2} \quad (4.33)$$

The neutral atmospheric refractivity (N^{NE}) is the same for both signals (frequency v_1 and v_2). In the ionosphere they are supposed to take the same pathway ($S_1 = S_2 \Rightarrow$ equal electron density N_e). Therefore the ionospheric contribution is only dependent on the optical path and the carrier frequencies of the signals. A final subtraction of the total optical path (L_1) of signal 1 gives the ionospheric corrected optical path (L_c).

But high order variabilities still remain in this context and may produce an error in daytime during high solar activity. Furthermore, the ray paths are actually not the same due to the dispersive properties of the ionosphere. In sum the optical path is a function of the bending angle, which can also be considered as a function of the inverse squared carrier frequency. The correction scheme for the refraction angle from Vorob'ev and Krasil'nikova [1994] has the advantage that it accounts for different ray paths because it is related to the impact parameter a instead of time t .

$$\alpha_c(a) = \frac{\alpha_1(a)v_1^2 - \alpha_2(a)v_2^2}{v_1^2 - v_2^2} \quad (4.34)$$

Most part of the refraction occurs in lower altitudes because of the high pressure. Therefore the ionospheric contribution on the refraction is considered to be lower than that of the neutral atmosphere. But the electron density is zero below 30 km and increases upward until about 150 km. This means that the refraction index increases as well and the ionospheric part predominates above 45 km. Small scale structures in the ionosphere and higher order terms can not be valuated with the linear bending angle correction scheme as well. Other errors like measurement noise and technically corrupted data are determined during error propagation analysis in the bending angle correction scheme. Hocke *et al.* [2003] presented a modification, where they applied a low pass filter on the bending angle profiles. It

reduces the noise amplification and is robust against technically corrupted data. Since the neutral atmosphere contains small scale structures as well, which are important for further retrievals, the high frequent part of the bending angle of signal L_1 is added to the corrected bending angle again, while the high frequent part of the more noisy L_2 is disregarded. More detailed informations about the application on CHAMP can be found in the thesis of *Gobiet* [2005].

4.5.3 Refractivity

This section gives a short insight into the retrieval of the refractivity from the derived bending angle, which depends on the impact parameter and on the heights of occultation. This information is used to determine atmospheric parameters like temperature, pressure, and geopotential height.

The relation between refractivity and bending angle is derived by using the ray path equation [*Born and Wolf*, 1999] and the assumption of a spherical symmetric geometry. It describes the change of the ray direction along the ray ($d\mathbf{s}/ds$). The variation of the radius from Earth's center (\mathbf{r}) along the ray path depends on the unit vector of ray direction ($\mathbf{s} \rightarrow d\mathbf{r} = \mathbf{s}ds$).

$$\frac{d}{ds}\left(n\frac{d\mathbf{r}}{ds}\right) = \nabla n \quad (4.35)$$

The change of the ray-direction is proportional to the refractivity gradient perpendicular to it. The bending angle follows from the norm of $d\mathbf{s}$. Since n varies only with the radius from Earth the equation can be written in scalar form and simplified with the assumption of constant impact parameters .

$$d\alpha = \frac{1}{n} |\nabla_{\perp \mathbf{s}} n| ds = \frac{1}{n} \frac{dn}{dr} \sin(\Phi) ds = \frac{d(\ln n)}{dr} \frac{\sin \Phi}{\cos \Phi} dr \quad (4.36)$$

Note that ds is the same as $dr/(\cos \Phi)$, while Φ describes the angle between the ray and the point vector \mathbf{r} . The following relation follows from inserting the impact parameter and expressing cosine as a function of sine.

$$d\alpha = \frac{d \ln n}{dr} \frac{a}{\sqrt{n^2 r^2 - a^2}} dr \quad (4.37)$$

The total bending angle as a function of the impact parameter a follows after integrating two times from outside the atmosphere ($r = \infty$) to the point nearest to the refraction center ($r = a/n$). The result is an Abel integral transform, which can be converted with standard mathematical routines, which are described by *Fjeldbo et al.* [1971]. Rearranging that equation leads to the inverse Abel transform (equation 4.38), which is used to obtain the refractive index with the bending angle. To avoid a singularity, which arises when a equals a' , the inverse Abel is transformed by partial integrations to equation 4.39, which shows

4 Radio Occultation Measurements

no singularities [Steiner, 1998].

$$n(a) = \exp\left(\frac{1}{\pi} \int_a^\infty \frac{\alpha(a')}{\sqrt{a'^2 - a^2}} da'\right) \quad (4.38)$$

$$n(a) = \exp\left(-\frac{1}{\pi} \int_a^\infty \ln\left(\frac{a'}{a} + \sqrt{\left(\frac{a'}{a}\right)^2 - 1}\right) \frac{d\alpha}{da'} da'\right) \quad (4.39)$$

In a further step, the refractivity is expressed as a function of the refractive index (equation 4.16), which depends on the impact parameter a , which in turn is a function of the height above surface (z) ($z(a) + R_c = a/n(a)$), where R_c describes the radius of ellipsoidal Earth at the occultation location. With this information the refractivity at a certain height can be determined.

$$N(z) = 10^6(n(z + R_c) - 1) \quad (4.40)$$

Since the inverse Abel transform carries down the information about the bending angle at higher altitudes, the refractivity at height z depends on the computed bending angles above that layer. This influence decreases with the distance. Thus not only the signal information about the atmospheric parameters is propagated, but also errors like thermal noise, receiver noise, local multi path information, and remaining ionospheric influence. Therefore, at the bending angle level sufficient information about the layers above are needed to retrieve reliable results.

4.5.4 Temperature and Pressure

From the refractivity profile one can derive the profiles of various atmospheric parameters. In mid troposphere and above, the water vapor content is very small and can be neglected (equation 4.18). Using equation 4.41 dry air temperature (T_{dry}), pressure (p_{dry}), and density (ρ_{dry}) can be calculated from RO refractivity profiles.

$$N(z) = k_1 \frac{p_{\text{dry}}(z)}{T_{\text{dry}}(z)} \quad (4.41)$$

The dry air density at certain height z follows from inserting N into the ideal gas law. Here R is the universal gas constant and M_d the molar mass of dry air, which is constant below 100 km.

$$\rho(z) = \frac{M_d p(z)}{R T(z)} \quad (4.42)$$

$$\rho_{\text{dry}}(z) = \frac{M_d}{Rk_1} N(z) \quad (4.43)$$

But gravity decreases with latitude ϕ and quadratic with height z , what is relevant for further pressure and temperature retrievals. The radius of the solid Earth varies by 21 km

between equator and poles. To calculate the pressure of a height layer, which depends on the mass of all air masses above it²⁶, one has to determine the density up to 120 km (where $p \cong 0$). This approximation can be done since the initial error reduces exponentially with scale height, while the integration moves deeper into the atmosphere [Foelsche, 1999]. The dry air pressure follows from the insertion of the dry air density at height z into the hydrostatic equilibrium equation.

$$p_{\text{dry}}(z) = \int_z^\infty \rho_{\text{dry}}(z')g(\phi, z')dz' = \frac{M_d}{k_1 R} \int_z^\infty N(z')g(\phi, z')dz' \quad (4.44)$$

$$g(\phi, z) = \left(\frac{r}{r+z}\right)^2 9.7803(1 + 0.0053 \sin^2(\phi)) \quad (4.45)$$

$$T_{\text{dry}}(z) = \frac{M_d \int_z^\infty g(\phi, z')N(z')dz'}{R N(z)} = \frac{p_{\text{dry}}(z)}{N(z)} \quad (4.46)$$

Here the height integral considers all layers (z') above height z the vertical distance from the surface. Then the temperature profile can be derived as a function of refractivity by inserting pressure and density into the ideal gas law. It is expressed as the ratio between the refractivity field above z and the refractivity at height z .

Finally the geopotential height of the pressure layer $Z(p)$ is additionally derived by combining the directly observed height z with the pressure profiles.

$$Z(p) = \frac{1}{g_{\phi=45^\circ}} \int_0^{z(p)} g(\phi, z')dz' \quad (4.47)$$

4.5.5 Ambiguous Water Vapor Signal

But things change in the lower troposphere of the mid and equatorial latitudes, when water vapor is not negligible anymore. The water vapor contribution on the signal increases up to 30 % in the moist boundary layer and locally even up to 50 % in moist regions like the tropes or within clouds [Kursinski *et al.*, 1997].

The dry retrieval produces a cold biased temperature value of several ten degrees. Gobiet [2005] calculated the difference between dry and "wet" (physical) air temperature using a forward model to simulate RO profiles of the atmosphere. Background information, for computing the moisture were taken from Peixoto and Oort [1992, 1996] and pressure and temperature data from the MSISE-90 climatology [Hedin, 1991].

This model shows that in tropical regions, where the specific humidity ranges between 18 g/kg at the surface and 0.5 g/kg in 9 km, the cold temperature bias raises up to 60 K close to surface and falls down to 3 K in 9 km. In cold and dry polar regions, the bias becomes negligible above 5 km ((0.25 g/kg) and reaches its maximum value of 9 K (1.6 g/kg) at the surface. Those results relate to global mean temperatures and do not represent the values of single measurements, which highly depend on local weather conditions, which

²⁶as described with the hydrostatic equilibrium equation

4 Radio Occultation Measurements

transport moist air masses. In general the real error is not that large [Gobiet, 2005]. Therefore, such analysis can be used to determine a layer from which dry air temperature retrievals produce reliable results.

Background information about temperature and pressure is needed to retrieve water vapor or vice versa, information about water vapor is needed retrieve physical temperature. Generally, numerical weather prediction²⁷ models provide relevant data for deriving water vapor profiles, which arise from rearrangements of equation 4.18.

$$e(z) = \frac{(N(z)T(z) - k_1 p(z))T(z)}{k_4} \quad (4.48)$$

Studies about water vapor retrieval errors have been carried out. One of them [Kursinski and Hajj, 2001] applied equation 4.48 and found out that the error amounts to 5 % in low latitudes ($<35^\circ$) and to about 20 % in cold and much drier polar regions. The absolute water vapor discrepancy is hereby quite constant (0.3-0.4 g/kg). Generally, the relative water vapor uncertainty increases with smaller water vapor pressure, what gives a gradient from low to high latitudes and from surface to upper height levels. This study has applied typical RO retrieved errors for pressure and refractivity and a temperature root mean squared error of 1.5 K, which is typical for NWP analysis systems.

All in all several studies showed that problems while determining the low tropospheric temperature arise rather due to the uncertainty of the refractivity retrieval than due to the water vapor itself [Beyerle et al., 2004; Ao et al., 2003].

4.6 Benefits from RO Observations

Obviously, RO can bring some improvements in observing weather and climate variations and trends. It produces vertical high resolved temperature data but is limited due to the number of operating satellites, which may be increased in the future, and due to moist-dry ambiguity inherent in the measurements. That leads to ambiguous source localization and pathway information, especially in the lower troposphere. Monthly and seasonal climatologies can be derived even with only a single satellite. Here are listed some fundamental advantages:

1. RO provides data with a high vertical resolution (1 km up to 100 m) in the stratosphere and troposphere.
2. Accuracy of temperature, pressure and geopotential height measurements is quite high. For instance, the random error of temperature ranges between 0.1 K and 0.5 K [Gobiet, 2005].

²⁷NWP ... numerical weather prediction

3. Additionally, it is insensitive to clouds and weather conditions, as long as clouds are found in high altitudes, where temperature and saturation vapor pressure are very low.
4. Actually the horizontal resolution is very low (200-300 km) what leads to sampling problems especially in the subtropical latitudes. A higher number of operating satellites would be able to fill the daily gaps, which remain even after one month of observations. For diurnal cycle observations, one needs much more measurements.
5. Nevertheless, they preserve even coverage over land and ocean, as MSU does.
6. Contrary to MSU, RO allows absolute calibration via timing measurements with atomic clocks and therefore an instrumental independent long term stability of measurements.
7. The afford efficiency for RO measurements is quite high, since radiowaves are transmitted anyway (GPS) and a simple receiver and a ground infrastructure are needed

All in all, the data are assimilated in NWP models and can be used to test climate models. This shall increase their reliability and reduce the uncertainties of long term predictions. Climate models are usually valuated against internal and external forces, which have regulated past and present climate states. To minimize the error, observed data have to be assimilated to the model parameters.

Observations from radiosondes and especially radiometers, which have lead to much higher quality of weather and climate forecast, supply models with relevant data and analysis. MSU could fairly increase the efficiency because it produces even distributed data over the highly interconnected land and ocean areas. Its installation has been a big improvement since previous observation methods have been limited on rural areas and some ship tracks. But major troubles arose due to their lack of vertical resolution and long term instability of the measurement time series (chapter 2). This can be the chance of new and more advanced observation methods which make further improvements like RO.

4 *Radio Occultation Measurements*

5 Validation Process

5.1 Problem Formulation

As described in the previous chapters, the data sets are provided at different resolutions. Therefore they have to be brought to the same grid before starting comparison analyses. For this purpose, the weighting functions were applied on the CHAMP RO temperature profiles¹ to compute MSU equivalent CHAMP temperature data of several atmospheric layers. The choice to calculate the temperature of the mid troposphere, the "upper" troposphere and the lower stratosphere (described in detail in Section 5.2.2) based on the availability of the weighting functions and on the combination of CHAMP with ECMWF profiles. Furthermore, the MSU measurements were summarized to the horizontal CHAMP grid, which consists of 18 zonal bands.

After bringing the satellite observations to a common grid, they could be checked for discrepancies and agreements. Thereby, the focus was on the monthly means of the time period **between September 2001 and December 2005**, because RO measurements are only available since that time. I considered the main characteristics (i.e. brightness temperature T_b and the monthly mean of T_b) of three atmospheric layers (TMT, TTS, and TLS - described below) and the anomalies between the observations. On the one hand, the analysis was carried out on zonal means of 10° latitudinal width (i.e., 18 latitude bands) and presented with contour plots. On the other hand, larger zonal means were calculated (with cosine weighting of the latitudes), which are the northern extratropics (30°N-70°N), the southern extratropics (30°S-70°S), the tropical regions (20°S-20°N) and an (almost) global between 70°S and 70°N.

This chapter gives a short summary of the data sets, their resolution and uncertainties and the way to derive the results, which are presented and described in the following chapter.

5.2 Description of the Data Sets

5.2.1 Radio Occultation Data

To get started with the data, it's important to know about their source, format, resolution and manipulations. RO data are produced by the German-U.S. satellite research mission

¹i.e. they are interpolated on the CHAMP pressure grid

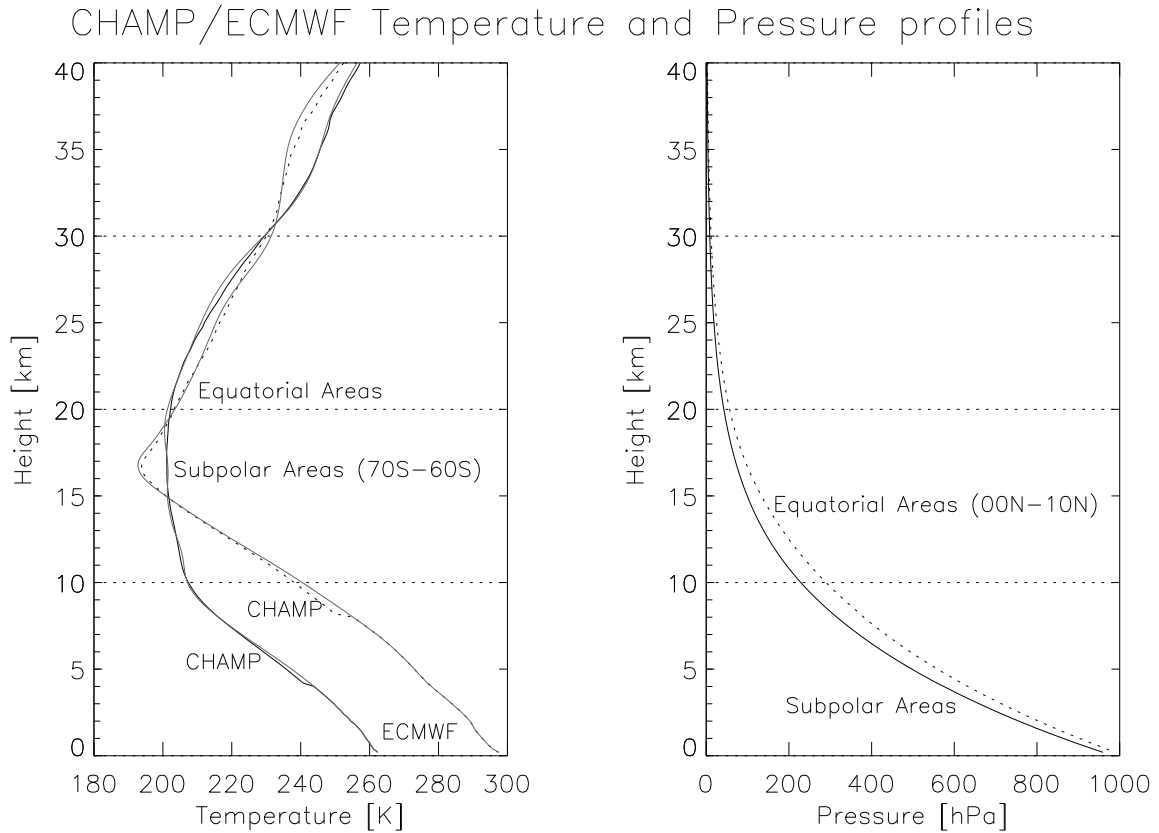


Figure 5.1: CHAMP temperature and pressure profiles (dotted and darker solid lines) relative to the ECMWF ones (lighter solid lines) for 70°S – 60°S and 00°N – 10°N in September, 2005. Here the limited CHAMP data were already extended by ECMWF.

CHAMP, which measures phase delay of both GNSS signals. CHAMP was launched in July 2000. Since September 2001 it provides the first continuous RO longterm time series and reached its highest efficiency with about 280 occultations per day in March 2002. Its raw data are managed by the Geoforschungszentrum Potsdam (GFZ), what carries out an internal calibration process on them. About 180 occultations are available for faculties and institutes around the globe for analysis and research purposes every day.

One of them is the Wegener Center, Graz. It uses the CHAMPCLIM retrieval scheme [Foelsche *et al.*, 2005] to compute atmospheric profiles of dry air temperature, geopotential height, dry air pressure, and density from the CHAMP RO profiles. Additionally the ECMWF analyses data are applied as background information and as reference data. Figures 5.2 and 5.1 show examples of a RO-based climatology and of some retrieved CHAMP profiles (combined with ECMWF). About 150 quality controlled profiles remain every day. They are almost homogeneously distributed around the Earth. In high altitudes the bending angle profiles are combined with background information, because of (residual) biases, which increase with altitude and reach a value of 0.2 K in 30 km [Gobiet *et al.*, 2005]. Re-

garding the TLS temperature, tests showed, that a bias of e.g., 2 K in 40 km has only a little influence on the result, due to the shape of the MSU TLS weighting function. In other words, the impact of temperature information above 30 km height is much smaller than that at height levels between 14 km and 24 km. Therefore the net bias on CHAMP TLS temperature decreases to 0.015 K, what could be shown in some perturbation analysis [Steiner *et al.*, 2007]. Since TMT and TTS are even less influenced by stratospheric temperature information, the impact becomes negligible.

Generally, the physical temperature is underestimated in the mid to low troposphere. Therefore temperature profiles are cut below 4 km at high latitudes and below 8 km at low latitudes. For this study, ECMWF physical temperature data are added below the cut-off height of up to 8 km in tropical and subtropical regions (between 40°S and 40°N) and of up to 4 km in polar areas ($\geq 70^\circ\text{N/S}$). In those regions, the zonal mean climatology profiles follow a stepwise curve. The difference between dry air temperature and actual temperature decreases below 0.1 K above 8 km in polar winter regions and above 14 km in moist tropical areas (see: Figure 5.1) but increases dramatically below 8 km as mentioned in Section 4.5.5.

Since the occultations are only "point" measurements, under-sampling in space and time occurs, which results in a global mean sampling error of 0.3 K. This is valid for the 360°E/W \times 10°S/N CHAMPCLIM "grid" and increases in some limited high latitude regions and during some monthly time intervals, while one half of the sampling error arises from the temporal resolution. CHAMP measures twice a day over each location but the local time of the RO event shifts by three hours every day and that induces a maximum bias of 0.15 K relative to one LEO satellite which would measure to all local times [Pirscher *et al.*, 2007].

Since CHAMP is the only regarded operating satellite in this study, the horizontal resolution ranges between 200 km and 300 km. But CHAMP produces high accurate vertical temperature measurements with a resolution of up to 150 m in the troposphere. This has principally the advantage that small scale structures within the atmosphere can be visualized. RO provides vertical information contrary to MSU measurements, which suffer from low vertical resolution and helps weather models like the ECMWF.

The ECMWF Analysis

The ECMWF analysis is an integrated weather forecast model, which assimilates observation data from e.g., radiosondes, radiometers, ground based weather stations, and satellite observations on a global 4-dimensional grid to generate analyses. Since December 2006 also radio occultation observations are assimilated. Starting from an initial condition it provides ten days of weather forecast two times per day with a time interval of six hours (00 utc, 06 utc, 12 utc and 18 utc). For that, the semi-Lagrangian model is used, which consists of 60 vertical layers up to 0.1 hPa and a spectral representation with triangular truncation at wave number 511 (T511) for upper air fields and horizontal derivatives [ECMWF, 2004]. Physical parameterizations and representations of atmospheric dynamics are described on

5 Validation Process

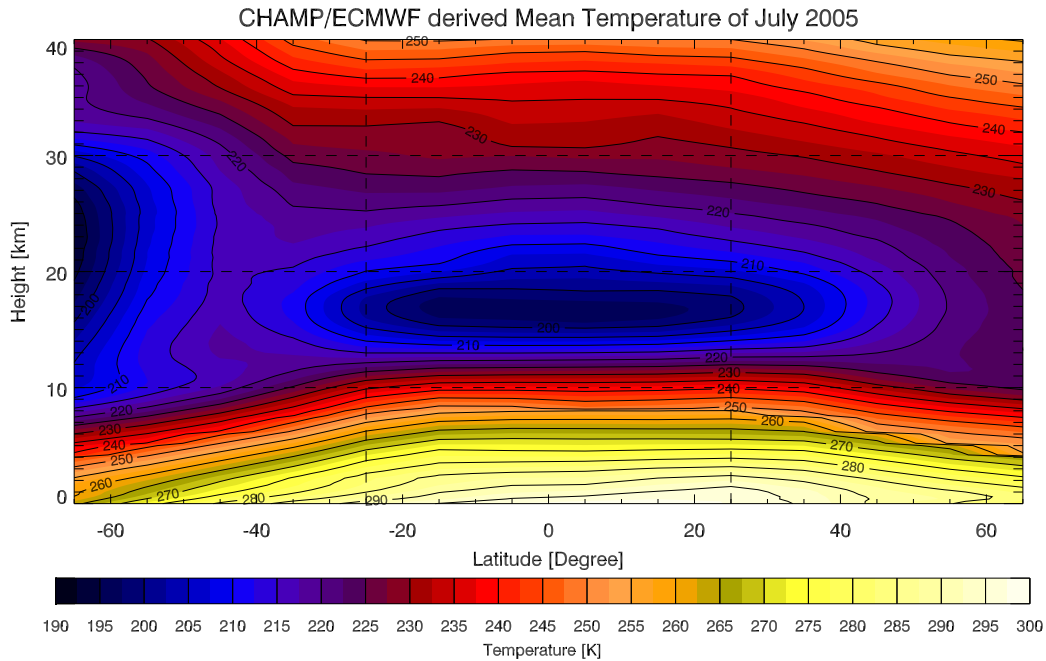


Figure 5.2: CHAMP RO climatology in July 2005. Note that the CHAMP data are already extended with ECMWF data in the troposphere.

a Gaussian grid. In February 2006, the horizontal resolution was improved up to T799 and the vertical one up to L91 (or 91 layers) [Untch *et al.*, 2006]. This has brought a better representation of the atmospheric wave activities as shown in the tropical tropopause analysis of Borsche *et al.* [2007], where the difference between ECMWF and CHAMP has decreased after February 2006. But the improvement of the resolution has been carried out after this validation period and is not relevant for further investigations. Actually the original T511L60 grid was regridded on a T42L60 field, which has a horizontal resolution of 300 km comparable to the horizontal resolution of RO data. This enables calculations of collocated ECMWF profiles, which are important for reliable analyses between CHAMP and ECMWF [Gobiet, 2005; Borsche *et al.*, 2006]. For that, the nearest ECMWF profiles at the closest time step were spatially interpolated to the location of data [Gobiet *et al.*, 2005]. The CHAMP climatologies were processed with the CCRv2.3 retrieval scheme.

Usually ECMWF data act as reference for operational comparison procedures. In this study they complete the CHAMP profiles, which are cut off at low altitudes, due to the dry-moist ambiguity. The introduction is important for calculating MSU equivalent TMT and TTS temperatures, which experience significant impacts from lower tropospheric regions.

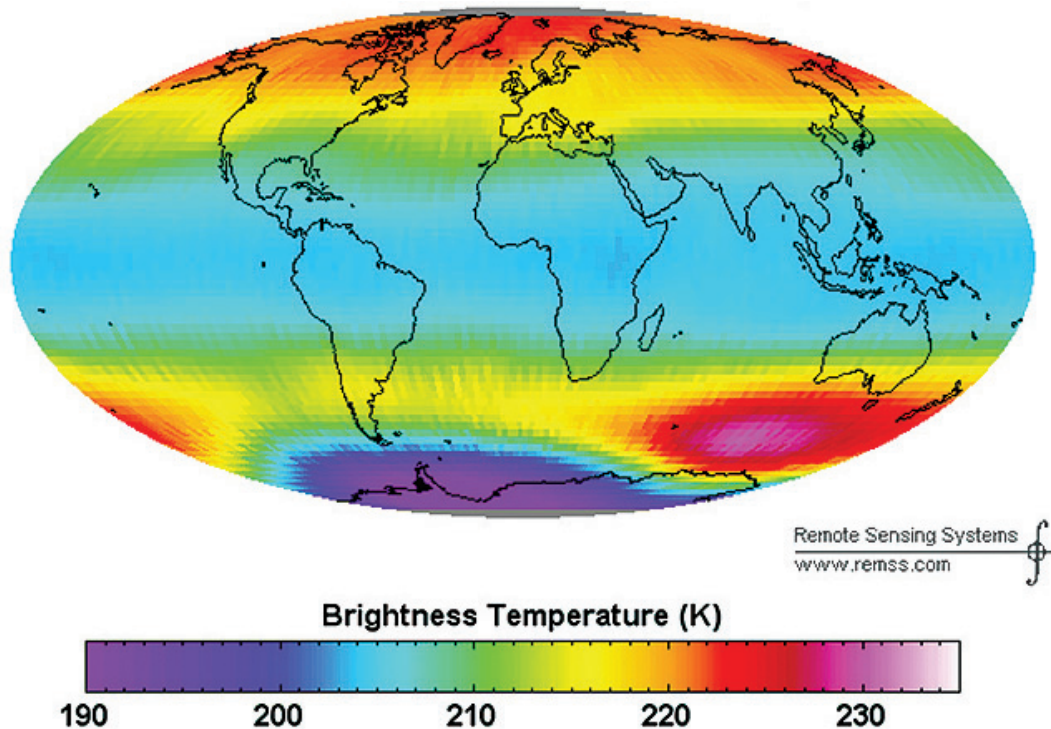


Figure 5.3: An example for a MSU retrieved monthly mean brightness temperature. This represents TLS in September 2005 http://www.remss.com/msu/msu_data_monthly.html.

5.2.2 Microwave Sounding Unit Data and Weighting Functions

The second data set arises from microwave emission measurements of MSU and AMSU². They measure the emission at several frequencies or channels below oxygen's absorption line at 60 GHz. The observed radiation is analysed and is derived to atmospheric temperature by several institutes. Of our prime interest are MSU data of the University of Alabama, Huntsville, USA (UAH) and the Remote Sensing System, Santa Rosa, California, USA (RSS), which provide data for several atmospheric layers, which are the lower troposphere³ or channel-1, the mid troposphere⁴ or channel-2, the tropopause region⁵ or channel-3, which is not provided by UAH, and the lower stratosphere⁶ or channel-4. Considered are TLS from UAH and TMT, TTS, and TLS from RSS. Since all layers contribute to the radiation output in space, the retrieved brightness temperature is described with so-called weighting functions, which are a function of pressure or height (Section 3.2). The choice to use those data is based on the availability of the corresponding weighting functions and on the point

²AMSU ... Advanced Microwave Sounding Unit

³TLT ... Temperature of the Lower Troposphere

⁴TMT ... Temperature of the Mid Troposphere

⁵TTS ... Temperature of the upper Troposphere and Stratosphere

⁶TLS ... Temperature of the Lower Stratosphere

5 Validation Process

that RO profiles are only provided down to a height of between 4 km and 8 km. Therefore TLT can hardly be applied on CHAMP data, as visualized in Figure 5.5 and Figure 5.6 and used for validation studies between CHAMP and MSU.

The monthly mean brightness temperature is given on a $2.5^\circ \times 2.5^\circ$ grid, which extends from 82.5°S to 82.5°N . The daily means are not that interesting due to the low RO resolution. Figure 5.3 shows an example map of the retrieved TLS brightness temperature, which was provided by RSS. For daily means, the TLS uncertainty is below 0.2 K in deep tropics and raises up to 0.3-0.4 K in north hemispheric mid-latitudes and up to 0.5-0.6 K in south hemispheric mid-latitudes (<http://ghrc.nsstc.nasa.gov/uso/readme/msulimb93.html>). But the uncertainty decreases to negligible values after summarizing the results to monthly means. CHAMP provides data on 10° latitude bands and MSU has to be fitted to that grid.

UAH provides monthly mean anomalies from the average monthly mean TLS temperature of the 20 year period 1979-1998 on <http://vortex.nsstc.uah.edu/data/msu/t4/> for public uses. The averages are also available there. RSS presents its monthly mean anomalies data in UAH-format on the ftp-server ftp://ftp.ssmi.com/msu/data/uah_compatible_format/ and describes the results in detail on the web page http://www.remss.com/msu/msu_data_description.html, which also shows the newest temperature trends and many useful links to publications. For this validation study, I applied version 5.1 of MSU data provided by UAH and version 2.1 provided by RSS.

Interesting for monthly means is the circumstance, that NOAA has applied the AMSU instruments since 1998 and the MSU instruments until 2004. Their error characteristics are indistinguishable from each other, but bias studies between equivalent MSU and AMSU brightness temperatures have shown a bias of 0.3 K between each other [*Christy and Spencer, 2003*].

Weighting Functions

The weighting functions and their meaning were well described in Section 3.2. Since the height of observation varies with the distance from the physical emission line, NOAA has chosen to observe a special set of frequencies or channels below 60 GHz (Figure 3.2). These are four MSU channels, which are at 50.30 GHz (MSU channel-1), at 53.74 GHz (MSU channel-2 or AMSU channel-5), at 54.96 GHz (MSU channel-3) and at 57.94 GHz (MSU channel-4 or AMSU channel-9), as shown in Figure 3.4.

Since 1998, NOAA has applied AMSU which provides 20 channels. The radiation, which is measured at a certain level, is a weighted mix of all emitters at all height levels and is described with the weighting functions. The weighting functions are named after the layer, which they represent to the biggest part. They are TLT (channel-1), TMT (channel-2), TTS (channel 3) and TLS (channel-4), as shown in Figure 5.4 [*Spencer et al., 1990; Christy et al., 1998*]. But TLT is be disregarded in this validation study.

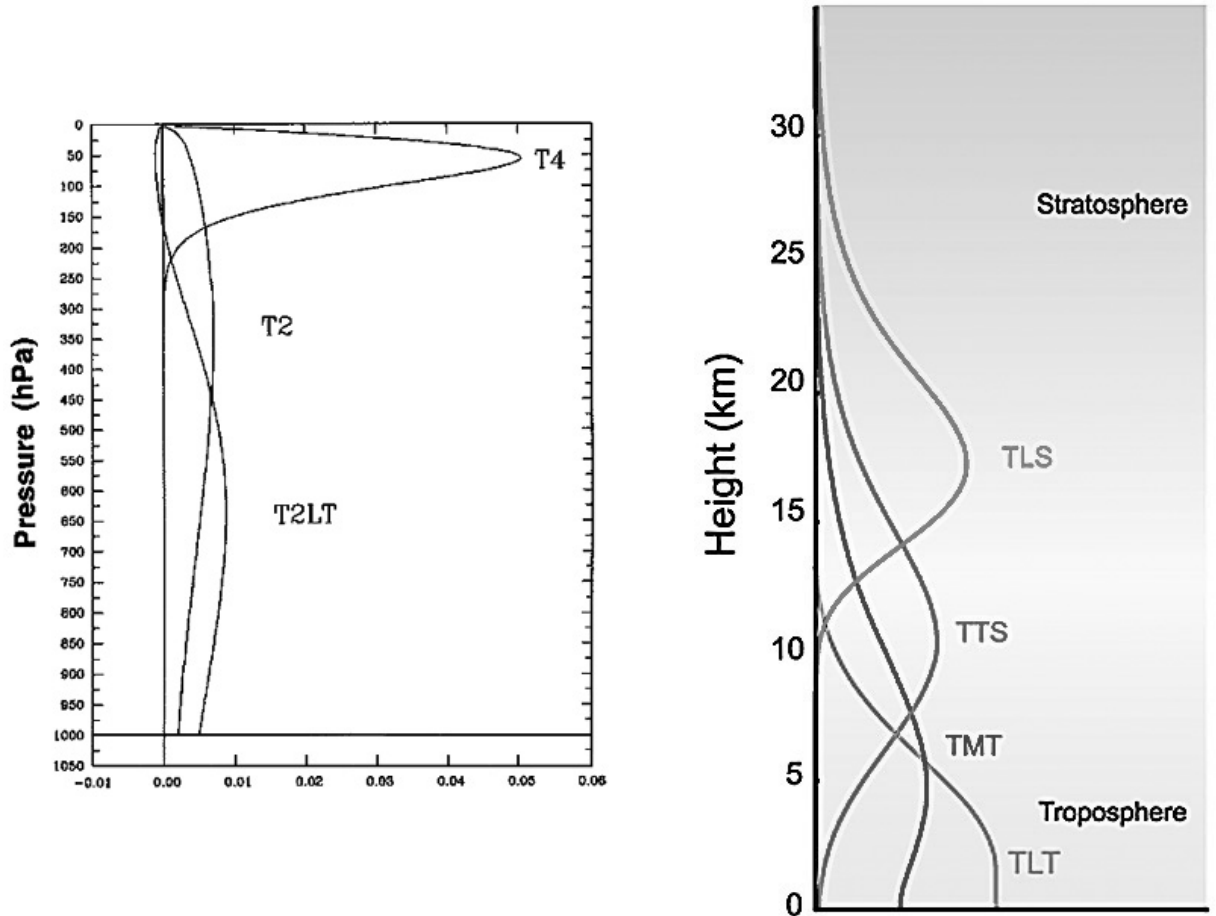


Figure 5.4: Left are the three MSU UAH weighting functions (T4, T2 and T2LT) [Christy *et al.*, 1998] and on the right side the four MSU RSS weighting functions or channels (TLT, TMT, TTS and TLS) for the troposphere and stratosphere http://www.remss.com/msu/msu_data_description.html.

1. **TMT** peaks at 372.5 hPa ($\sim 8 \text{ km}^7$). Two separate functions are provided. They are specifically designed for rural and maritime areas due to different atmospheric properties above land and oceans. The surface emissivity comes also into account, which is relevant for TMT and also for TTS. TMT describes mainly the troposphere, but includes a significant proportion (15%) of the atmosphere above 150 hPa, which approximately belongs to the lower stratosphere [Fu *et al.*, 2004].
2. **TTS** describes the upper troposphere and the lower stratosphere. It peaks at 140 hPa ($\sim 12 \text{ km}^8$) and extends from 2 km to 20 km, as visualized in Figure 5.4. The representation depends strongly on the latitude since the tropopause raises from 8 km until 18 km between the poles and the tropics. In high latitudes, TTS consists of layers

⁷RSS: $\max(g_{\text{TMT}}) = 0.00130 \text{ hPa}^{-1}$

⁸RSS: $\max(g_{\text{TTS}}) = 0.00284 \text{ hPa}^{-1}$

5 Validation Process

of the lower stratosphere in a similar way as TLS in equatorial regions, as visible in Figure 5.6. There, TTS plays a similar role as TMT in high latitudes since it represents most parts of the upper troposphere.

3. **TLS** is in comparison to TMT and TTS less affected by other atmospheric layers. About 90 % of the information originate between 150 hPa (≈ 12 km) and 20 hPa (≈ 26 km), with the maximum located at 57 hPa⁹. Only in the tropical regions, where the tropopause raises up to 18 km, 20 % of TLS extend down into the troposphere [Christy and Spencer, 2003]. This has to be taken into account, when analysing the tropical stratospheric temperature (Figure 5.3).

The RSS weighting functions TMT, TTS and TLS were used. They are provided as a function of height and are available for public use on the RSS ftp-server¹⁰. Figure 5.4 (right panel) visualizes the RSS weighting functions.

The UAH weighting function for the lower stratosphere was kindly provided as a function of pressure by John Christy, UAH, with the recommendation that the weighting functions are supposed to be better applied on anomaly time series and may not be that accurate for absolute temperature profiles.

5.3 Calculation of MSU Equivalent Temperatures

First of all I have analysed the weighting functions of each source and layer and used them on a 5 hPa grid between 2.5 hPa and 997.5 hPa, which were transformed from the received function of weight per km (RSS) or from a different pressure grid (UAH) [Steiner *et al.*, 2007]. The aim was to bring them on a pressure grid, which is useful for the CHAMP profiles. Generally, the RSS weighting functions show a smaller maximum than the UAH ones as visualized in Figure 5.5, due to the fact that RSS also considers the surface emission, contrary to UAH. For TLS it is not relevant but for TTS and especially for TMT it means a relatively high impact. Therefore, I have extended the CHAMP/ECMWF temperature profiles down to the surface by linear interpolation. For that I have computed the temperature gradient per 200 m between 200 m (T_{199} ¹¹) and 600 m (T_{197}) and added it to the lowest temperature value.

$$T_s = \frac{T_{200\text{m}} - T_{600\text{m}}}{4} * 2 + T_{200\text{m}} \quad (5.1)$$

Wegener Center has provided the CHAMP/ECMWF temperature and pressure profiles as a function of height from 40 km to 0.2 km with 0.2 km resolution. The heights above 40 km are not relevant for the MSU weighting functions, because pressure already decreases below 2.5 hPa.

⁹RSS: $\max(g_{\text{TLS}})=0.009 \text{ hPa}^{-1}$; UAH: $\max(g_{\text{TLS}})=0.0102 \text{ hPa}^{-1}$

¹⁰ftp://ftp.ssmi.com/msu/data/uah_compatible_format/

¹¹A single CHAMP profile consists of 200 (5*40) elements

5.3 Calculation of MSU Equivalent Temperatures

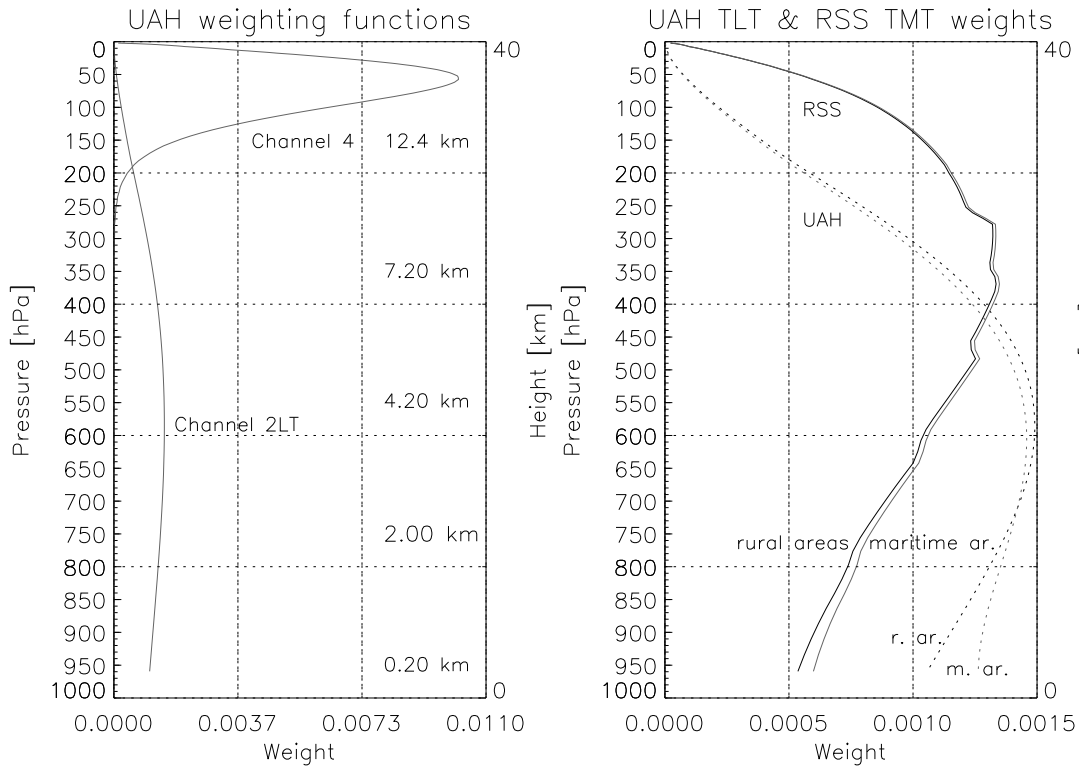


Figure 5.5: The UAH weighting functions (TLS, TLT) are shown on the left side. The right figure compares RSS TMT rural areas (r. ar.) with maritime (m. ar.) ones and UAH TLT r. ar. with UAH TLT m. ar.

However, CHAMP dry temperatures were complemented by ECMWF data below the cut-off heights, which is at 8 km in the tropical troposphere ($30^{\circ}\text{S} \longleftrightarrow 30^{\circ}\text{N}$). Since moisture decreases with increasing latitude the cold bias becomes less pronounced. Therefore the CHAMP data were applied down to 4 km in 60°N/S and poleward. The transition between high and low latitudes follows a stepwise curve: 5 km, 6 km and 7.4 km in $30^{\circ}\text{-}40^{\circ}$, $40^{\circ}\text{-}50^{\circ}$ and $50^{\circ}\text{-}60^{\circ}$ ¹².

Since almost a half of the tropospheric temperature data have been replaced by analogous ECMWF ones it is difficult to compare CHAMP RO with the MSU results. More than one half ($\leq 3/4$ in the tropics) of the TLT weighting function lies within the ECMWF "region", as visible in Figure 5.5.

TMT peaks higher than TLT in a layer, which is represented by CHAMP almost everywhere. As shown in Figure 5.5, there are two kinds of TMT weighting functions: one for rural areas (TMT_r) and one for maritime areas (TMT_m). In the troposphere, TMT_m is slightly larger than TMT_r, while both peak at the same altitude and the difference decreases with height. RSS has regarded the emissivity of different surfaces. It is much higher for lands than for oceans. Therefore, the rural areas have a higher surface weight than the

¹²The crossing is visible in Figure 5.1 and in Figure 5.2

5 Validation Process

maritime ones (0.07264 hPa^{-1} and 0.05315 hPa^{-1}). All in all, the MSU weighting functions (wf) are given for fixed pressure values and can not be directly applied on the CHAMP¹³ temperature and pressure profiles, since CHAMP measures the parameters as a function of height from 200 m up to 40 km. Therefore I needed to interpolate the weighting functions dynamically to the observed pressure grid. Generally pressure varies between $1000 \pm 50 \text{ hPa}$ at the surface and $2.3 \pm 0.5 \text{ hPa}$ in 40 km. The fact that pressure decreases exponentially with height enables a linear interpolation between two pressure points ($\ln(p(a)), \ln(p(b))$) on the logarithmic scale. But that scheme has a little uncertainty since temperature varies irregularly and with it the scale height and pressure drop. The value of a straight line (y) at point x results from the product of the gradient between two known points x_0, x_1 and the distance between e.g., x and x_0 plus the initial value of the straight line (y_0) at x_0 . ($\Delta y = k\Delta x + y_0$) I applied this on the CHAMP pressure profiles. The weight g represented the straight line, which was known for several points ($\ln(p(a)), \ln(p(b)), \dots$). If a CHAMP point ($\ln(p(i))$) lay within two MSU points, the corresponding weight followed from the gradient between the two known points times the distance from CHAMP to MSU plus the weight at point $\ln(p(a))$.

$$g_{\text{champ}}(i) = \frac{g_{\text{msu}}(b) - g_{\text{msu}}(a)}{\ln p_{\text{msu}}(b) - \ln p_{\text{msu}}(a)} (\ln p_{\text{champ}}(i) - \ln p_{\text{msu}}(a)) + g_{\text{msu}}(a) \quad (5.2)$$

With that method I got the MSU weighting functions interpolated to the CHAMP pressure profile. But if pressure dropped down below 2.5 hPa , what was not represented by the weighting functions, I needed to extrapolate to those points. It worked similar to linear interpolation, while the gradient was always determined between the first and the second point, i.e. $g_{\text{msu}}(2.5 \text{ hPa})$ and $g_{\text{msu}}(3 \text{ hPa})$. In some cases, that resulted in negative weights, especially when pressure dropped quite rapidly below 2 hPa . Then, I simply set those values to zero. Sometimes, it was also important to extrapolate to high pressure values above 997.5 hPa . This was not a big deal, because the same method could be applied as for extrapolating to lower points. Figure 5.6 presents an example of calculated weighting functions, which I applied on the CHAMP temperature profiles, which were a function of pressure.

With the interpolated MSU TLS, TTS, and TMT weighting functions it was possible to calculate the CHAMP brightness temperature (T_b) for those layers. Since the height of observation was the same for temperature and pressure, they could be converted directly by following synchronously the indices. But before that, the weighting functions had to be normalized, because they had been recalculated and therefore they did not sum up to unity. So, I created a sum over the average weight of each pressure layer (Δp) and this for all $n(=200)$ elements, which is the normalization factor (*norm*).

$$\text{norm} = \frac{g_0}{2} p_0 + \sum_{i=1}^{n-1} \left[\frac{g_i + g_{i-1}}{2} (p_i - p_{i-1}) \right] \quad (5.3)$$

¹³From now on, CHAMP is equivalent to CHAMP/ECMWF since both sources are used

5.3 Calculation of MSU Equivalent Temperatures

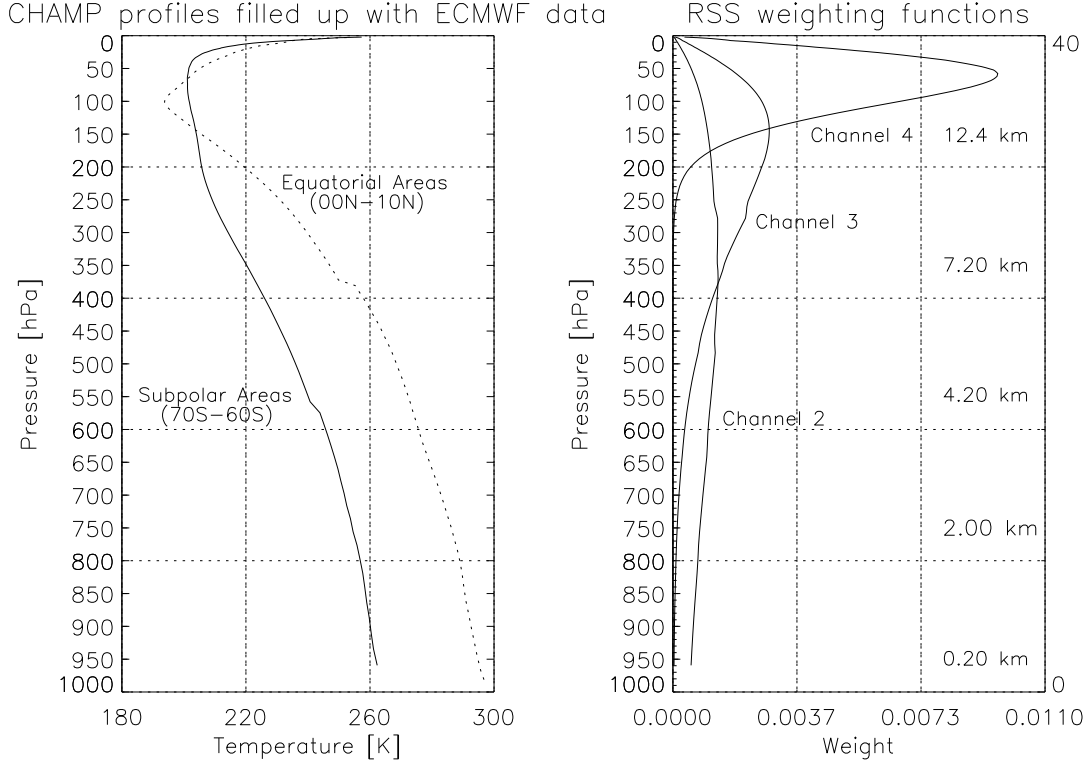


Figure 5.6: CHAMP/ECMWF temperature profiles as a function of pressure in September 2005 (left) which are weighted with the RSS weighting functions (right).

For the RSS weighting functions there came also a surface weight (g_s) into account, which was simply added to $norm$. After that, each calculated weight was divided by the sum of the weights.

The procedure to determine the brightness temperature of each MSU level was quite similar, with the only difference that the average weight between two pressure levels was multiplied with the observed CHAMP temperature at the higher pressure level.

$$T_b = \frac{g_0}{2} p_0 T_0 + \sum_{i=1}^{n-1} \left[\frac{g_i + g_{i-1}}{2} (p_i - p_{i-1} T_i) \right] + g_s T_s \quad (5.4)$$

The surface weight is regarded by adding the product between g_s and the surface temperature T_s .

This was the way, how the MSU equivalent CHAMP brightness temperatures were computed for the lower stratosphere (UAH and RSS), the "upper" troposphere, mid troposphere (RSS), and the low troposphere (UAH). This procedure was carried out for all months between September 2001 and December 2005 and also for all 10° latitude cells between $70^\circ S$ and $70^\circ N$.

But there were two TMT weighting functions: one for rural and one for maritime areas,

5 Validation Process

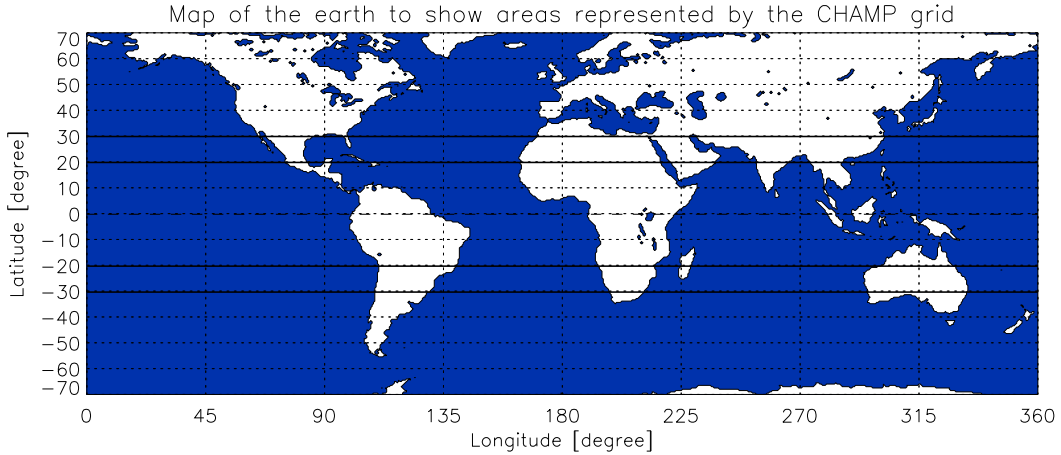


Figure 5.7: Global distribution of land and ocean.

which had to be combined analogously to the relation between land and ocean. The necessary informations could be received from a land-sea-mask, which was provided by the MPI-Hamburg [Dr. Luis Kornblueh, MPI-Hamburg, personal communication, 2000]. It describes the land-ocean distribution on a $0.5^\circ \times 0.5^\circ$ grid between the North- and the South pole (Figure 5.7). The procedure to fit those informations onto the $360^\circ \times 10^\circ$ CHAMP grid followed mainly the mechanism to summarize the MSU temperature values (see section below). To get a feeling, which regions are represented by each element of the zonal grid, I have also visualized it in Figure 5.7. The proportional distribution of land and

Latitude	Oceans	Lands	Latitude	Ozeans	Lands
<i>90S-80S</i>	0.000	1.000	<i>Equ-10N</i>	0.774	0.226
<i>80S-70S</i>	0.289	0.711	<i>10N-20N</i>	0.739	0.261
<i>70S-60S</i>	0.901	0.099	<i>20N-30N</i>	0.626	0.374
<i>60S-50S</i>	0.992	0.008	<i>30N-40N</i>	0.576	0.424
<i>50S-40S</i>	0.969	0.031	<i>40N-50N</i>	0.498	0.502
<i>40S-30S</i>	0.886	0.114	<i>50N-60N</i>	0.436	0.564
<i>30S-20S</i>	0.769	0.231	<i>60N-70N</i>	0.299	0.701
<i>20S-10S</i>	0.782	0.218	<i>70N-80N</i>	0.697	0.303
<i>10S-Equ</i>	0.768	0.232	<i>80N-90N</i>	0.901	0.099
<i>70S-30S</i>	0.936	0.064	<i>Total Globe</i>	0.712	0.288
<i>20S-20N</i>	0.766	0.234	<i>70S-70N</i>	0.726	0.274
<i>30N-70N</i>	0.476	0.524			

Table 5.1: The relative distribution of land and ocean on a zonal (10° latitude steps), "hemispherical" and global scale. The "hemispheres" are the northern and southern midlatitudes and the tropical areas.

oceans, as listed in Table 5.1, varies strongly from north to south. The largest land areas extend between 30°N and 70°N in the northern midlatitudes, where the continents slightly predominate the oceans, while almost 70% between 60°N and 70°N is land. Completely different are things in the southern midlatitudes (70°S-30°S), where dry land makes only 6.4% of the total surface. The difference is supposed to cause different behaviors between the north-hemispherical atmospheric temperature and the south-hemispherical one. The most maritime conditions are definitively between 60°S and 50°S, where the (is)lands sum up to few promilles. The Antarctica is not present in this study, but nevertheless it has an influence on the southern midlatitudes.

On the global average, the oceans predominate with about 71%. But it strengthens up to 73%, because I have regarded only latitudes between 70°S and 70°N. The tropical regions come with 76.6% oceans quite close to the global average. With the informations about the relation between land and ocean, it was possible to calculate the grid-specific TMT brightness temperature.

5.4 Regridding of MSU Data

Generally, UAH and RSS provide their results homogeneously on a 2.5°×2.5° grid. But contrary to CHAMP, MSU provides the data in form of monthly mean temperature anomalies relative to the monthly mean references (1979-1998), which has to do with the bias reduction and merging procedure.

In the section above, the CHAMP brightness temperature was computed for three layers for zonal means with 10° latitudal width. There were 144 temperature values per longitude and 72 per latitude. The aim was to regrid the MSU data onto the CHAMP grid. For each latitude, I created an arithmetic mean of all temperatures, which were evenly distributed over all longitudes. But for that one has to consider the shape of the Earth. The radius relative to the rotational axis increases toward the equator and with it the distance between two longitude degrees as well as the circumference. For instance, the circumference at the equator is twice the quantity than at 60°. This relation mainly fulfills a cosine function with a specific amplitude. But the amplitude, which is the radius in Earth's case, varies since the Earth is an ellipsoid. Therefore, it produces a small bias if the latitudes are weighted with a cosine function. The magnitude of such an error is quite small (~0.1%) because the radius increases by 0.35% from the poles towards the equator.

Therefore I weighted the data with the cosine of the latitude and normalized the result by dividing it by the sum of the weights. The angles needed to be transformed from degree to radian to give the right results.

$$T_j = \frac{\sum_{i=1}^4 (T_i \cos(\phi_i))}{\sum_{i=1}^4 (\cos(\phi_i))} \quad \dots \quad i = (j + 1.25) \frac{\pi}{180}, \dots, (j + 8.75) \frac{\pi}{180} \quad (5.5)$$

This procedure was repeated for all 14 cells of interest ($j=70^\circ\text{S}, 60^\circ\text{S}, \dots, 60^\circ\text{N}$), while each of them contained four MSU temperatures (T_i) between $j+8.75^\circ$ and $j+1.25^\circ$ with an interval of 2.5° . The cell j is added to i to receive the true latitude (ϕ) of the data¹⁴. This procedure simply fitted the MSU temperatures of each atmospheric layer to the CHAMP grid. This was applied on the lower stratosphere (UAH, RSS), the high troposphere and mid troposphere (RSS) to get the monthly mean and the temperature anomalies relative to this twenty years average. Those informations were necessary to gain the observed temperature of the CHAMP observation period between September 2001 and December 2005.

5.5 Calculation of Temperature Average and Anomalies

After the CHAMP/ECMWF climatologies and the MSU-UAH and MSU-RSS data had been brought on the same grid, they were ready for validations and comparisons. One feature was to compute a monthly mean temperature and the anomalies from this average during the analysis period. Due to the observation period, the frequency of each month differed slightly; the months between January and August appeared four times and the other ones five times. The different frequencies had to be regarded before calculating the brightness temperature and monthly mean from CHAMP and MSU. Actually, a MSU monthly mean temperature from UAH and RSS is already available for all layers, but for a period (January 1979 until December 1998), when CHAMP could not be used for validations. Therefore I computed a new MSU monthly mean temperature of TLS, TTS. and TMT, with the resulting new anomalies. The period of determining the new data was the same as for CHAMP (September 2001 until December 2005) of course. The new anomalies are actually the old ones plus a constant, which is the difference between the new and the old temperature average.

After that, I calculated larger zonal mean averages (weighted with the cosine of the latitude), which were the southern mid-latitudes, which extend from 70°S to 30°S , the tropical regions (20°S - 20°N), the northern mid-latitudes (30°N - 70°N), and the quasi-global average (70°S - 70°N).

This was the comparison set-up to get a feeling where the two climate monitoring systems provide the same observation results and where they differ from each other. Possible discrepancies may arise due to different resolutions, methodologies, technical requirements, or due to other biases. To find that out, anomalies time series were established relative to a reference data set. I decided to apply the MSU RSS measurement series as reference because RSS provided the temperature series as well as the corresponding weighting functions of three atmospheric layers (TLS, TTS, and TMT). Furthermore, RSS has received reliable trend results of the mid troposphere, as discussed in the Sections 3.4 and 2.4. Therefore the temperature observations are supposed to be quite accurate. All "interesting" weighting functions were principally available and it would have been possible to use

¹⁴e.g. for cell 60°N : $j=60, j+i=61.25,63.75,66.25,68.75$

5.5 Calculation of Temperature Average and Anomalies

the CHAMP/ECMWF climatologies as reference and not MSU RSS. But the weighting functions may have uncertainties and the analysed profiles stem from two different sources. Additionally, MSU provides a higher horizontal and temporal resolution than CHAMP. So, the anomaly time series of UAH-TLS were calculated relative to RSS-TLS to get the differences between the prime MSU processing centers and of the RSS weighted CHAMP profiles at several layers (TLS, TTS, TMT) to visualize the differences between RO and MSU. Additional anomaly plots between UAH- and RSS-TLS weighted CHAMP profiles are supposed to show some discrepancies between using different MSU weighting functions.

5 *Validation Process*

6 Results and Discussion

In this chapter the results of the CHAMP-MSU validation procedure are presented. First of all, it shows the reference brightness temperature sets of RSS of the lower stratosphere (TLS), the "upper" troposphere (TTS), and the mid troposphere (TMT) as well as of UAH for the lower stratosphere in comparison to the analogous RSS and UAH weighted CHAMP/ECMWF temperature profiles. Afterward, the observed temperature means will be discussed in detail, while considering the differences between the standard MSU temperature averages and the observed ones during the CHAMP observation period. Additionally temperature anomalies will be presented as the deviation of the brightness temperatures from the monthly average of the period September 2001 - December 2005.

Then, the anomalies of the observed brightness temperatures are shown with respect to the reference data sets, which are the MSU results provided by RSS (i.e. monthly means of January 1979 - December 1998). Finally the difference between the CHAMP/ECMWF and MSU RSS anomalies is investigated, while the results are based on zonal mean climatologies (10° latitude width) for four larger zonal means: (almost) global (70°S - 70°N), tropics (20°S - 20°N), northern hemispheric extra-tropics or NET (30°N - 70°N), and southern hemispheric extra-tropics or SET (70°S - 30°S).

6.1 Brightness Temperature

Figure 6.1 shows the observed brightness temperature during the CHAMP observation period, gained with MSU (left panel) and RO (right panel) measurements. The mid troposphere shows a temperature range between 234 K and 258 K, while the inter-annual variability is clearly visible in the northern and in the southern extra tropics (NET respectively SET). The northern hemisphere shows a much stronger inter-annual variability than the southern one, which has the origin in the different land ocean distribution, which is visible in Table 5.1. The oceans damp the diurnal and annual temperature cycle of the surface and also influence the mid troposphere. For instance, at 65°N the temperature ranges between 236 K and 251 K, while it ranges between 234 K and 243 K at 65°S . This results in an inter-annual temperature variability of 15 K and 9 K, respectively. But nevertheless, the temperature is smaller in the SET, especially in the high latitudes, than in the NET. The SET regions are in the domain of the Antarctica, which cools its surroundings. The variability decreases with lower latitude and vanishes in the tropical regions, which show no inter-annual temperature cycle and a constant temperature of about 257 K. But

6 Results and Discussion

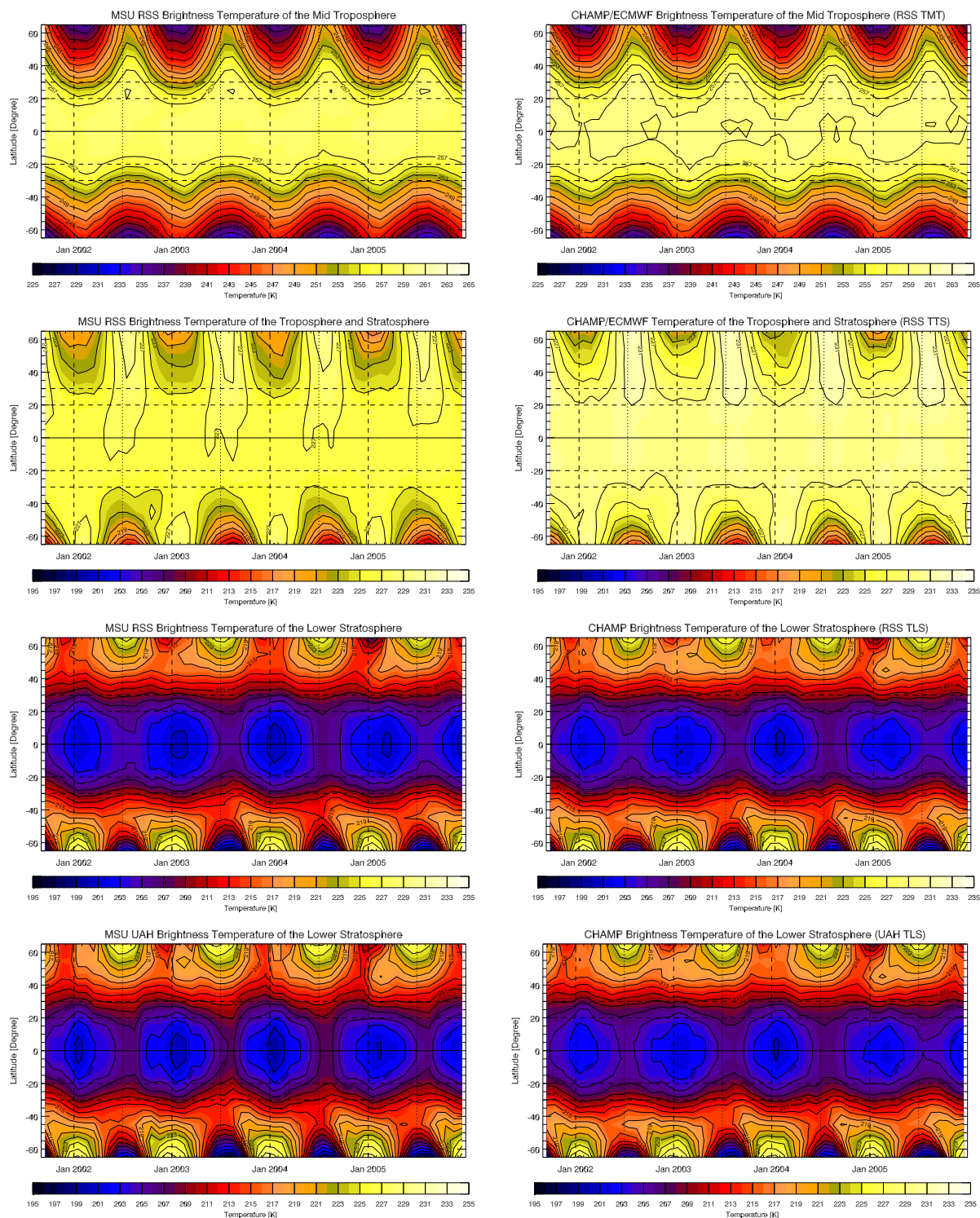


Figure 6.1: The observed brightness temperature from MSU (left) and the analogously weighted CHAMP/ECMWF profiles (right). From top to bottom they represent from RSS the mid troposphere, the upper troposphere, the lower stratosphere and from the UAH lower stratosphere.

CHAMP/ECMWF shows a slight variability of 1 K between 258 and 259 K. Generally, the temperature is slightly higher than that of MSU, what is visible from the northern hemisphere up to the southern mid latitudes. The NET temperature minimum from CHAMP/ECMWF is between 1 K and 2 K warmer than that from RSS, while the maximum one is almost the same, which in turn results in a smaller variability.

This difference between MSU RSS as the reference and CHAMP/ECMWF RSS is better visible in Figure 6.2. The figure shows the observations on a zonal scale (NET, SET, Tropics and Global). Globally, CHAMP/ECMWF temperatures are about 1 K warmer than MSU, while the discrepancy is a little larger between December and February. This difference exists in all regions. In the NET, it ranges between 0.5 K in January and February and 1.5 K in July and August. In the SET, the CHAMP/ECMWF TMT is between 1 K and 0.5 K higher than the MSU RSS one. But there, the maximum occurs rather in summer than in winter. In the tropics, there is no inter-annual variation visible and the difference is continuously 1 K and increases up to 1.2 K (Figure 6.5).

This indicates a systematic difference. RSS provided the weighting functions as a function of height and not of pressure, on which the microwave emission depends on, as explained in Chapter 3. In the TMT channel, the maximum radiation output occurs at about 370 hPa. This produces an error since pressure is a function of temperature and density, which varies from season to season. If temperature increases, the scale height increases as well and therefore the height of a certain pressure layer. Figure 5.1 shows the difference between the pressure profiles in high and low latitudes. For instance in September 2005, 370 hPa were measured at 7 km in sub polar areas and at 8.5 km in equatorial regions. The global weighting function for the mid troposphere peaks at about 8 km. Therefore it may introduce a warm bias in the tropics and a cold one in higher latitudes in comparison to the physical weighting function. Probably, a part of the warm bias was canceled by the dry temperature measurements from CHAMP in the tropics. It already deviates from the physical temperature several km above the cut-off height at 8 km, as visible in Figure 5.1. In an experimental study, where we have only applied ECMWF data to compute the TMT brightness temperature, the difference increased by about 0.4 K. In the NET, the deviation between winter and summer (Figure 6.2) decreased and ranged between 1.3 K and 1.8 K. Also in the SET, the summer difference did raise (up to 1.5 K). This indicates, that the cut-off height is set a bit too low, especially in the NET summer, where the dry temperature introduces a cold bias. But nevertheless there remains a significant difference.

In the "upper" troposphere, the temperature is as expected smaller than that in the mid troposphere. The MSU RSS brightness temperature ranges between 211 K and 230 K, while the inter annual variability decreases with decreasing latitude and vanishes in the tropics, similar to the mid troposphere (Figure 6.1). Regarding only the MSU RSS results, the tropical TTS is about 30 K colder than the tropical TMT (227-228 K), which met the expectations, because temperature decreases with height and the troposphere extends up to about 17 km there. The maximum of the TTS weighting function is located at 12 km and extends to the main part between 2 km and 20 km. Therefore the stratospheric inter-annual temperature variability (described below) does not affect the result. But in the high latitudes the weighting function extends far up into the stratosphere, contrary to the

6 Results and Discussion

low ones. The height of the tropopause varies between 17 km at the equator and 8 km at the poles. Since the stratosphere is characterized by strong ozone depletion during winter especially in the SET, the interannual temperature variability is highest in the SET, where TTS ranges between 211 K in August and 228 K at 65°S in January and February. The maximum temperature is the same as in the tropics and reaches the highest values in the NET at 65°N, where the variability ranges between 230 K in July and 219 K in the late winter months. In these latitudes the weighting function penetrates far up into the stratosphere, where the ozone layer plays an important role as a greenhouse gas and therefore influences the temperature. At 60° the TTS variability is higher in the SET and is in magnitude comparable with the TLS one. Furthermore, the overall minimum of the Northern hemisphere was observed in February, 2005, the same time when the stratosphere experienced the strongest cooling (Figure 6.1). Equatorwards, the influence of the mid troposphere seems to increase since the interannual variability of TTS converges to the TMT one. On larger zonal scales, MSU RSS TTS shows an interannual temperature variability everywhere. Even on the global scale TTS ranges between 225 K in November and 226.5 K in July. This is in magnitude and in behavior comparable with the interannual variability of the tropics (226 K in January and 227 K in July), as shown in Figure 6.3. The interannual temperature variability is much larger in the extra-tropics. In the NET, TTS ranges between 229 K in July and 222 K January-February, while it ranges between 227 K in February and 220 K in July-August in the SET.

As visible in Figure 6.3, there exists probably a significant difference between the MSU RSS and the CHAMP/ECMWF measurements, while the reference temperature time series is about 3 K colder than CHAMP/ECMWF on the global scale. The difference seems to have a trend and increases especially in the tropical regions from 2.9 K in September, 2001 until 3.3 K in December, 2005 (Figure 6.5). In the northern and in the southern extra-tropics the difference time series ranges between 2.5 K and 3 K, while the maximum deviation can be found in the winter and the minimum one in the late summer (August/September and February/March, respectively). The corresponding month of the maximum changes from year to year and is between December and February in the NET and between June and September in the SET.

In the experimental study, where only the ECMWF profiles were applied to compute the TTS brightness temperature, the difference time series increased up to 3.4 K on the global scale and up to 3.6 K in the tropics (Figure 6.13). Also in the extra-tropics the difference has increased, while the inter-annual variability has decreased. The MSU RSS TTS weighted ECMWF time series is between 3.0 K and 3.4 K warmer than the analogous MSU RSS one in the NET and respectively between 3.2 K and 3.0 K warmer in the SET.

The brightness temperature of the lower stratosphere was provided by RSS and by UAH. Therefore the CHAMP profiles were weighted with the UAH weighting function as well as with the RSS one. Generally, the temperature ranges between 198 K and 227 K (Figure 6.1). A comparison analysis between the TLS weighted CHAMP climatologies and a radiative transfer model [Steiner *et al.*, 2007] showed, that the difference ranged between 0.1 K and 0.2 K in larger zonal mean (i.e., NET, SET, ...). This is the layer, where also the tropical regions show an inter-annual variability (201-205 K) with the minimum in February

Brightness Temperature of the Mid Troposphere

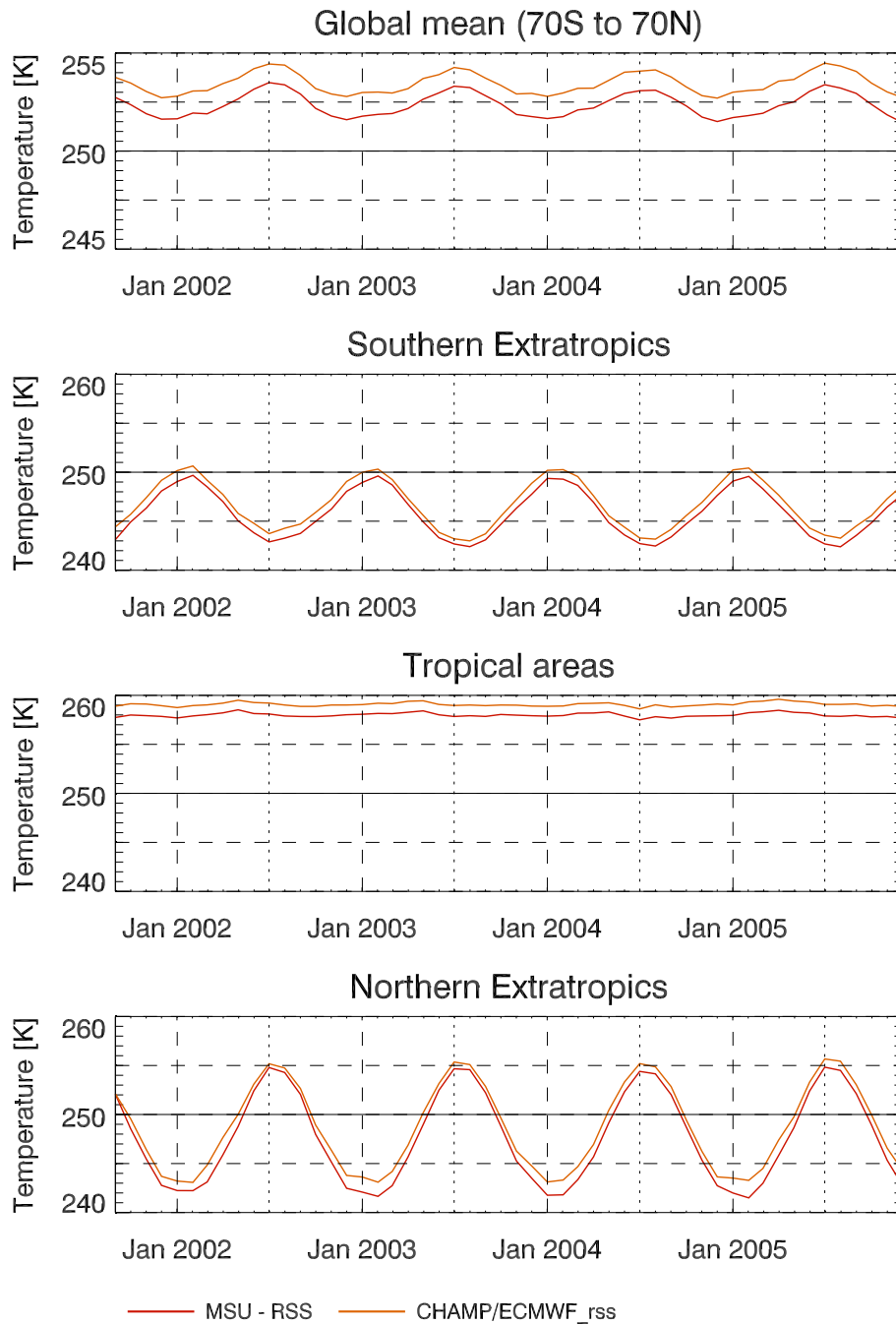


Figure 6.2: Brightness temperature of the mid troposphere from CHAMP/ECMWF ("CHAMP/ECMWF-RSS") and RSS ("MSU-RSS") for September 2001 - December 2005.

Bright. Temp. of the Troposphere and Stratosphere

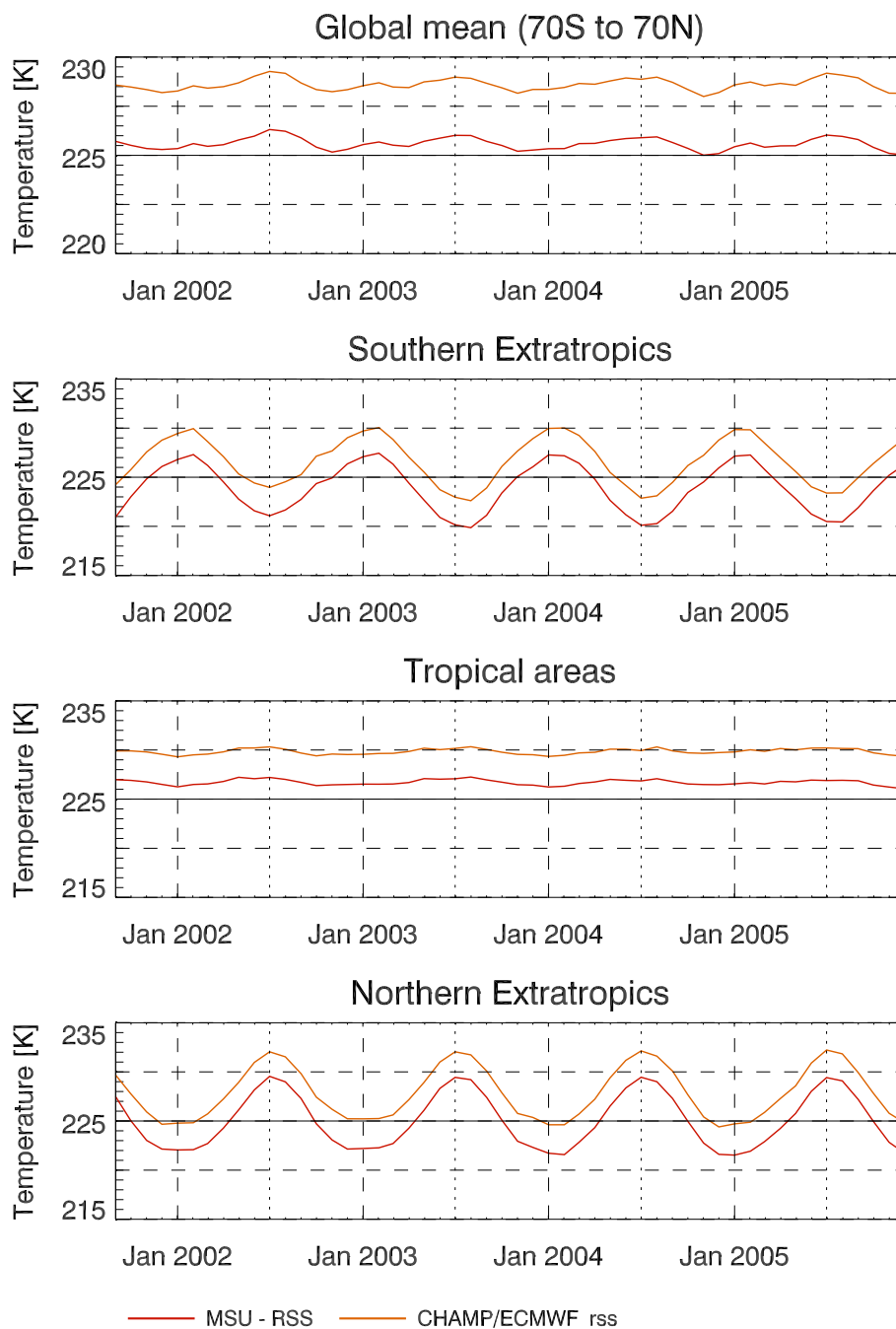


Figure 6.3: Brightness temperature of the troposphere and stratosphere from CHAMP ("CHAMP/ECMWF-RSS") and RSS ("MSU-RSS") for September 2001 - December 2005.

Brightness Temperature of the Lower Stratosphere

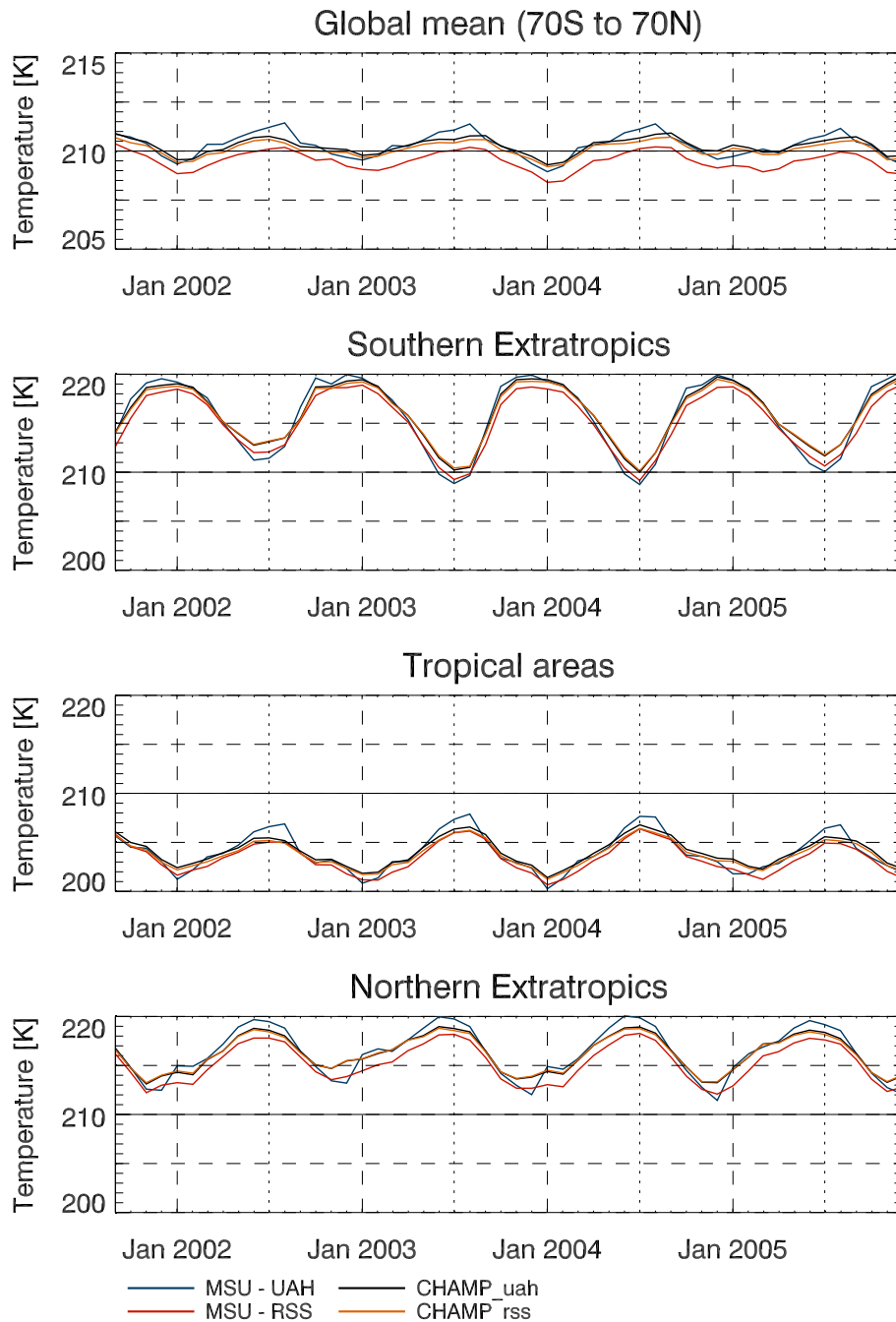


Figure 6.4: Brightness temperature of the lower stratosphere from CHAMP ("CHAMP-UAH", "CHAMP-RSS"), UAH ("MSU-UAH"), and RSS ("MSU-RSS") for September 2001 - December.

Brightness Temperature relative to the Reference

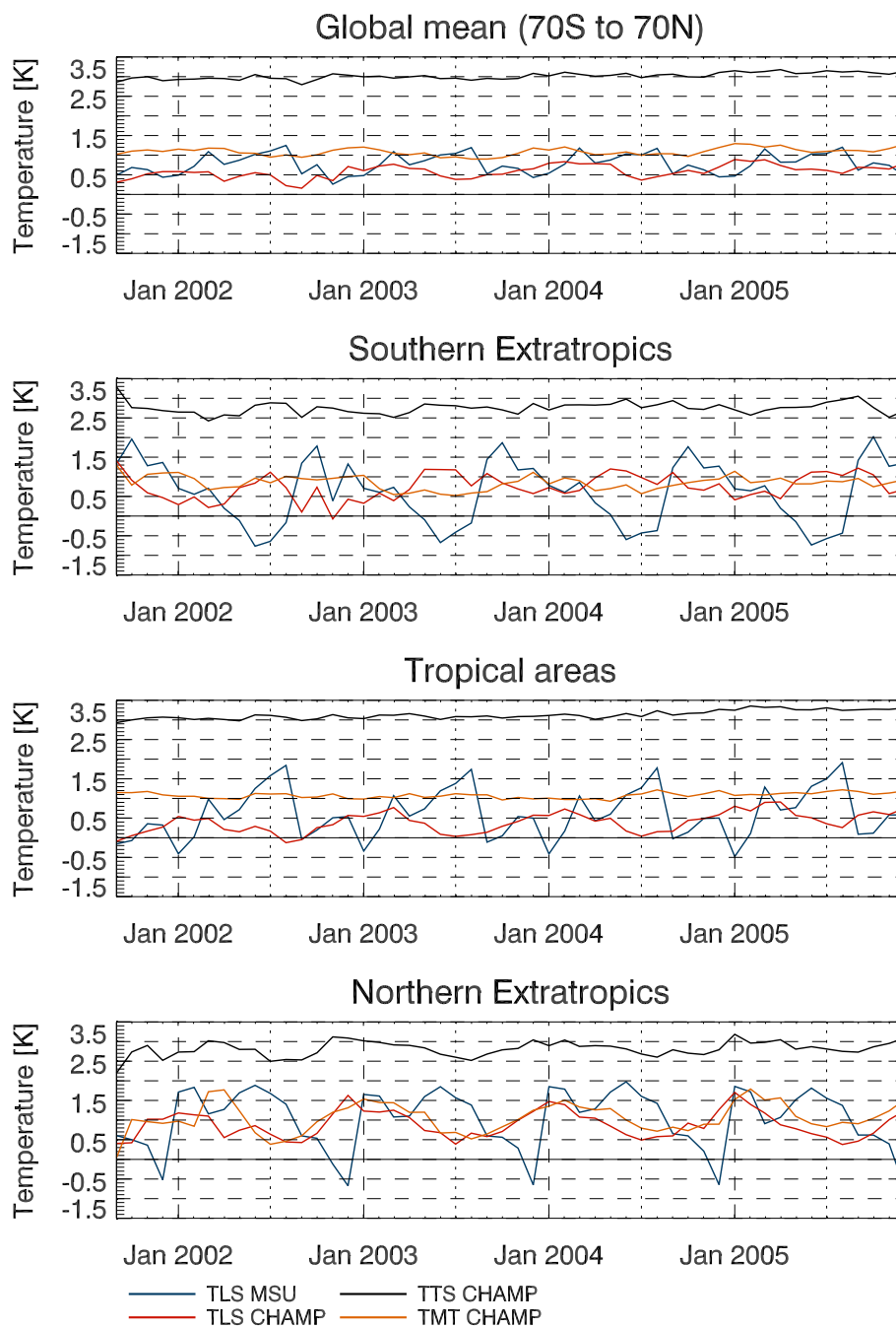


Figure 6.5: The difference between the observed brightness temperature from MSU-UAH and CHAMP/ECMWF-RSS relative the MSU-RSS values (the reference data set) for the layers TLS, TTS, and TMT for September 2001 - December 2005.

and the maximum in August, while UAH retrieved a slightly higher maximum. The inter-annual variability is much larger in the southern hemisphere than in the northern one and it is smallest between 30° and 40° . At 65°N , the temperature ranges between 212 K and 225 K, and in 65°S between 199 K and 227 K¹ with the minimum in November and in August, respectively and the maximum in August and in February, respectively. The sharp decrease in the SET winter troposphere has its origin in the reduction of the ozone layer. In February 2005, this is also visible in 65°N , but with a much smaller magnitude. On the global scale, the TLS MSU UAH climatologies show a systematic difference to TLS MSU RSS, as shown in Figure 6.5. Globally, the discrepancy is highest in August (+1.2 K) and smallest in November (+0.5 K) (Figure 6.4). In the SET the variability of the difference time series is much larger. There, it ranges between -0.6 K in June and +1.9 K in October. Similar behaviors can also be found in the NET (1.9 K in June and -0.6 K in December) and in the Tropics (-0.4 K in January and 1.8 K in August), as visualized in Figure 6.5. The difference time series between MSU RSS and MSU UAH shows a systematic inter-annual variability. The reason for this is, that the MSU processing centers applied different temperature retrieval mechanisms, as described in Section 3.3 and 3.6. Furthermore, the absolute MSU temperatures were gained by summing up the monthly mean and the anomaly time series. Therefore, one can assume, that the "error" characteristics are the same for the monthly mean temperature (Figure 6.12).

The TLS weighting functions from RSS and UAH are very similar to each other, leading to almost identical CHAMP brightness temperatures. On the global scale, the difference between the RSS weighted and the UAH weighted CHAMP profiles is with 0.3 K quite small (not shown here). In the SET and in the NET, the difference is even smaller, but it has a maximum during summer.

The difference between MSU RSS and CHAMP RSS is larger. It ranges between +0.4 K (July) and +0.7 K (January) globally and increases slightly over the observation period like the tropical one. The largest difference can be found in the NET (+1.5 K in January and +0.5 K in July) and the smallest one in the Tropics (0.0 K in August and +0.6 K in February). Generally the smallest difference relative to MSU RSS was measured in September-November 2002.

6.2 Monthly Mean Reference Temperatures

The monthly mean reference temperatures were computed for the CHAMP observation period (September 2001 - December 2005) in order to calculate temperature anomalies and to compare them with respect to the same time period. The difference between the provided (January 1979 - December 1998) and recalculated (September 2001 - December 2005) MSU monthly mean reference temperatures will be discussed at first (Figure 6.6).

¹Results from the MSU RSS climatologies

6.2.1 Comparison between the MSU Means

The TMT results show a higher inter-annual temperature cycle in the northern hemisphere² than in the southern hemisphere³. The oceanic influence is very strong in the SET, where the minimum and maximum are in August and February, in comparison to the NET, where minimum and maximum are in January and July. Due to its high heat capacity, water damps the annual temperature cycle and shifts the maximum.

The difference between the 1979-1998 monthly mean and the 2002-2005 one during the CHAMP observation period is shown in Figure 6.6 and 6.7. Globally, the TMT difference ranges between 0.2 K and ≥ 0.3 K. It is higher in the NET than in the SET. There is a large difference between December and January in the NET, which probably arose due to the different number of these months the data sets comprise. The SET warmed in September and October more (0.3 K) than in the other months, while the monthly mean remained the same in November and December. In the Tropics the difference is highest February (0.5 K) and smaller in the north hemispheric summer. The largest increase is visible in the NET (between 0.5 K and 0.3 K with no seasonal variability). Nevertheless, the plot confirms approximately the difference between the north hemispheric and the south hemispheric surface warming (Table 2.3) and that the trend penetrates up into the mid troposphere.

In the "upper" troposphere (TTS channel), the difference between the two MSU RSS means is smaller than in that in the mid troposphere. It ranges between 0.2 K (April) and ≥ 0.0 K (June to December) in the global mean and is slightly higher in the Tropics. The SET experienced a warming of 0.3 K in October but a cooling of a similar magnitude from November until January. The NET show no warming from July to December and a warming of about 0.35 K in January and in spring. But TTS is largely affected by the stratosphere especially in the mid and high latitudes. This means, that a stratospheric cooling can overlay a tropospheric warming. Figure 6.19 shows the development of the troposphere in the mid latitudes throughout a year. The tropopause is highest in summer and lowest in winter. Interesting is in Figure 6.7, that TTS always develops in a range between TMT and TLS except in the SET winter, where TLS has increased from July until September (between 0.3 K and 0.5 K). This increase is even larger than the TMT one. The unusual stratospheric warming⁴ may be an indication of a recover of the ozone layer.

Similar to TMT, the inter-annual variability of the monthly mean of TTS increases polewards. It is 4 K at 30°N and 12 K at 65°N respectively ≤ 1 K at 30°S and 17 K at 65°S. The variability has slightly decreased relative to the standard MSU RSS TTS mean by 2 K. In the NET the temperature maximum and minimum are in July and January. But that is different to the SET, where a slight temperature maximum is visible in February and a strong minimum between June and August (depending on the latitude). As explained before the highest temperature can be found at 65°N in July (230 K), which is about 4 K higher than in the Tropics.

²65°N: 17 K; 30°N: 8 K

³65°S: 10 K; 30°S: 5 K

⁴contrary to the greenhouse effect and the development in other regions and months

6.2 Monthly Mean Reference Temperatures

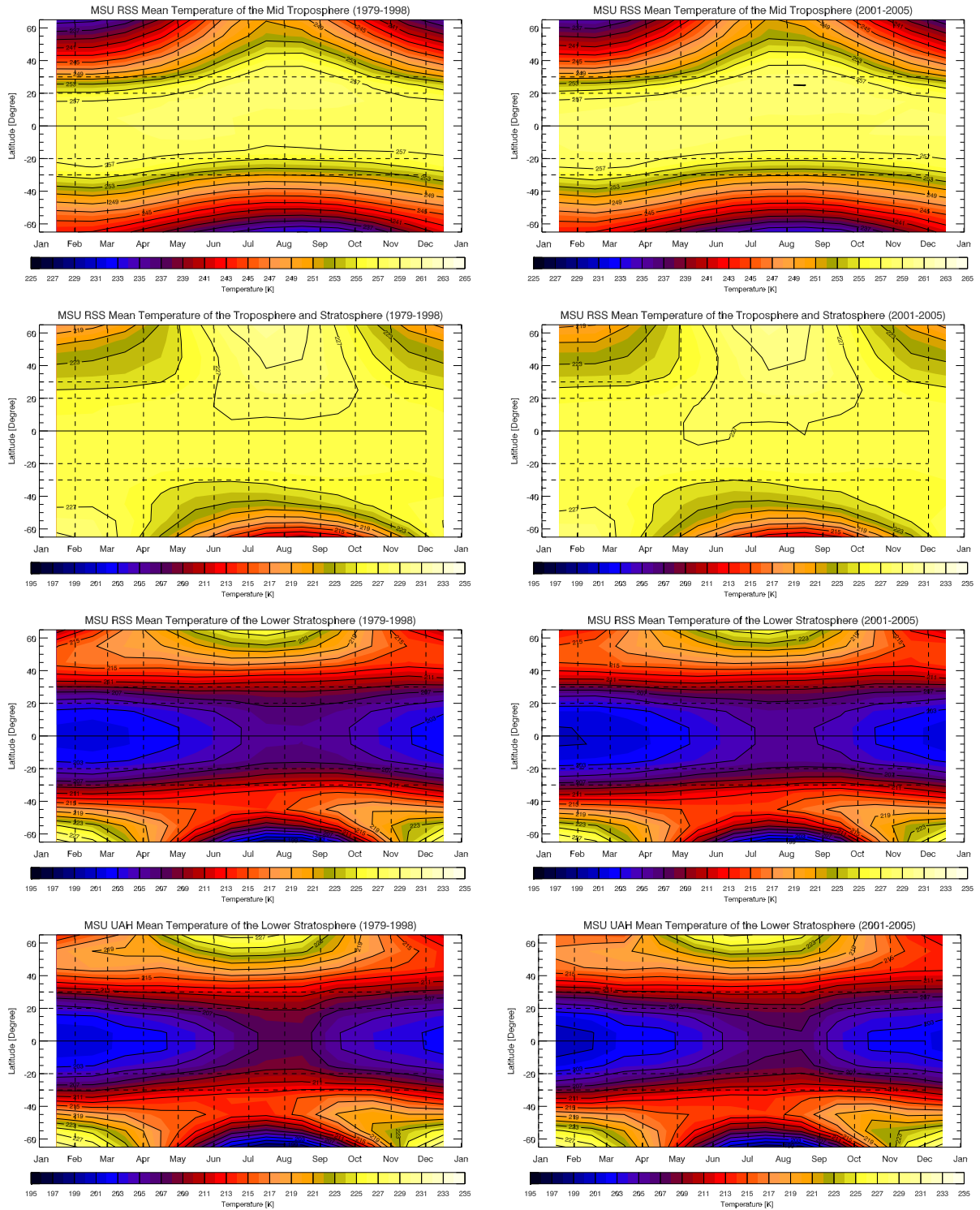


Figure 6.6: Monthly mean brightness temperature of the period January 1979 - December 1998 (left column) and September 2001 - December 2005 (right column). From top to bottom the rows visualize the RSS TMT, RSS TTS, RSS TLS, and UAH TLS.

MSU Monthly Mean: 2001-2005 vs 1979-1998

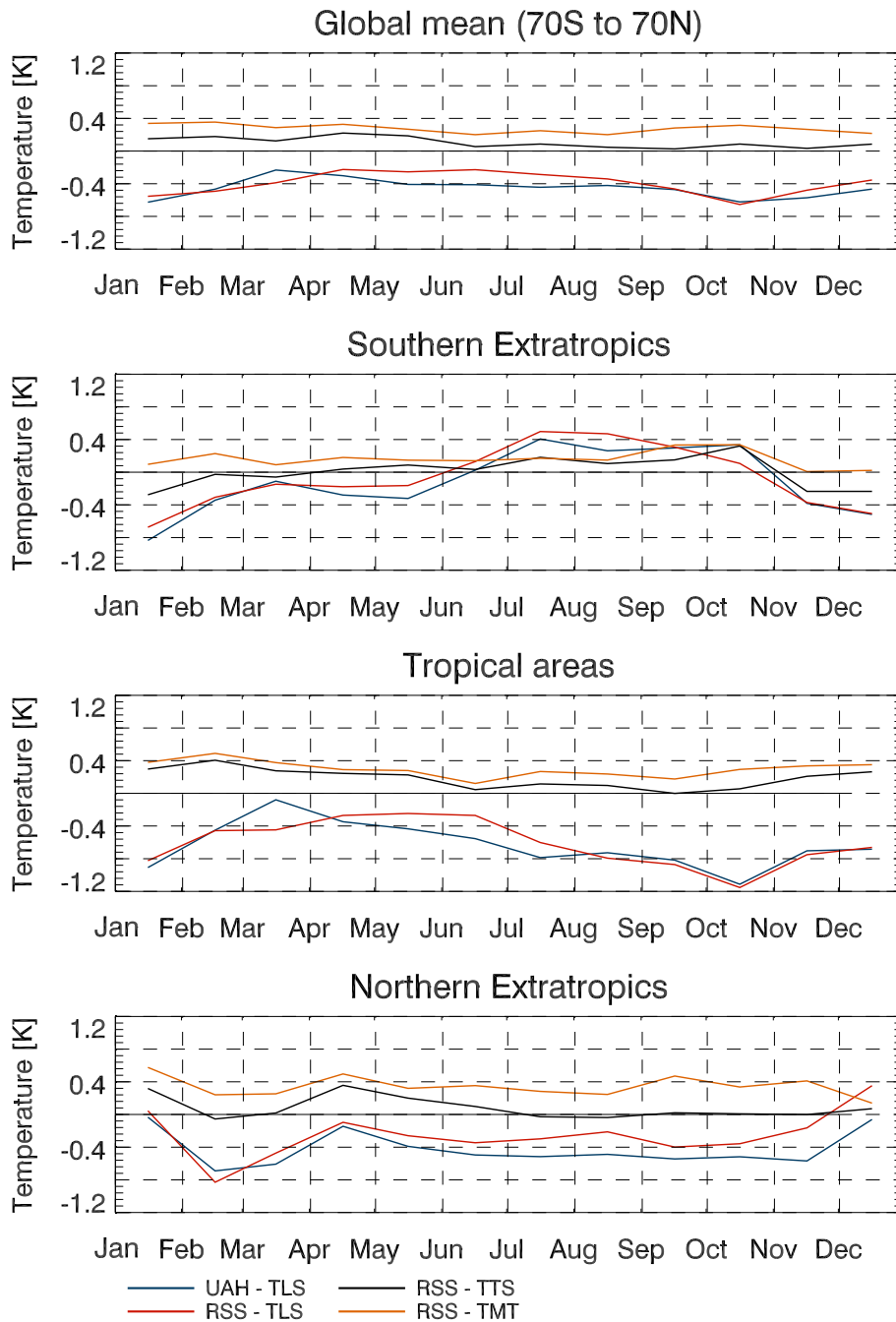


Figure 6.7: The difference between the MSU monthly means of the period January 1979 - December 1998 and of the period September 2001 - December 2005 for TLS, TTS, and TMT.

The standard MSU RSS monthly mean shows a much larger inter-annual temperature cycle in lower stratosphere than in the "upper" troposphere, which is lowest in the subtropical regions and largest in the southern high latitudes. The coldest (197.7 K) and also the warmest (229.8 K) temperature was observed at 65°S. This results in a variability of 32 K. Contrary to the lower altitudes, in the Tropics exists an inter-annual temperature cycle too (4 K), with the minimum in February (202.0 K) and the maximum in August (206.2 K). In the NET at 65°N, the monthly mean ranges between 210.1 K in January and 226.2 K in July. This variability is much smaller than in the SET, where the minimum develops in July and the maximum in January.

The recalculated RSS monthly mean (2001 and 2005) shows the same variability in the Tropics (201.4-205.6 K). The summer maximum decreased to 229.1 K at 65°S and to 225.9 K at 65°N, while the winter minimum became larger (198.8 K respectively 211.1 K). Very clear visible is the crossing between the tropical maximum in July-August and southern high latitude maximum in January.

Principally, UAH and RSS show an global average cooling of 0.3-0.4 K between March and August and 0.6 K in October and January, while the UAH result is lower than the RSS one. The difference is largest in the NET, where RSS observes less cooling in summer and fall (0.2 K more than UAH) and even a warming in December and January (0.4 K higher than UAH), while they are quite similar in the other months. In the Tropics, RSS measures a slightly larger cooling than UAH. Between August and January the monthly mean decreased between 0.8 K and 1.2 K. The drop was smaller in the other months (0.3-0.4 K) (Figure 6.7).

6.2.2 Comparison between CHAMP and MSU

All in all, MSU observed a warming in the mid troposphere and cooling in the lower stratosphere. But there is a difference between the MSU and the CHAMP/ECMWF brightness temperature time series (Section 6.1), which is much larger than the deviation between the 1979-1998 MSU monthly mean and the 2002-2005 one. The CHAMP/ECMWF monthly mean is shown in Figure 6.8, which also pictures the difference between MSU and CHAMP/ECMWF. The Figures 6.9, 6.10 and 6.11 show the observed monthly mean of MSU in comparison to CHAMP/ECMWF on a zonal scale, which also visualize the standard MSU means (dashed curve).

In the mid troposphere, CHAMP/ECMWF has systematically observed 1-1.2 K more than MSU RSS during the same period. While the difference increases slightly from 1 K up to about 1.1 K in the Tropics between July and September, it varies much more in the NET, where it ranges between 1.5 K during winter and about 0.6 K between July and September. This behavior arises due to the increasing cold bias in the higher altitudes during summer. The limited CHAMP profiles are always extended by the ECMWF ones up to the same height throughout a year, which is known as the cut-off height. Figure 6.19 shows the ECMWF profiles below the cut-off height of 6 km and the CHAMP ones above that height. Visible is the leap between CHAMP and ECMWF, which is largest during summer, when

6 Results and Discussion

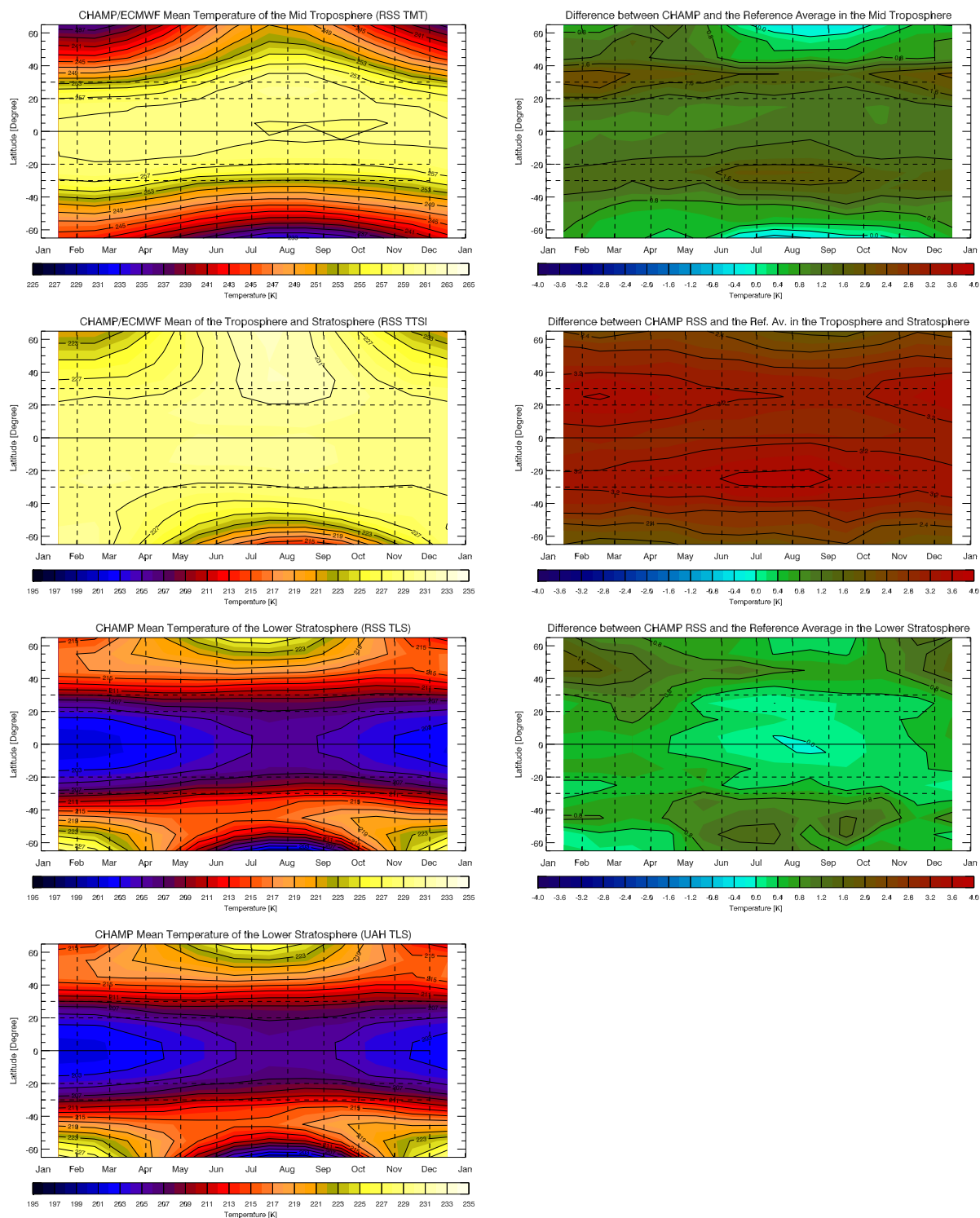


Figure 6.8: The left panel shows the CHAMP/ECMWF monthly mean brightness temperature, weighted with the MSU weighting functions, of TMT (RSS), TTS (RSS), TLS (RSS), and TLS (UAH) and the right one visualizes the difference between CHAMP (RSS) and MSU RSS

Mean Temperature of the Mid Troposphere

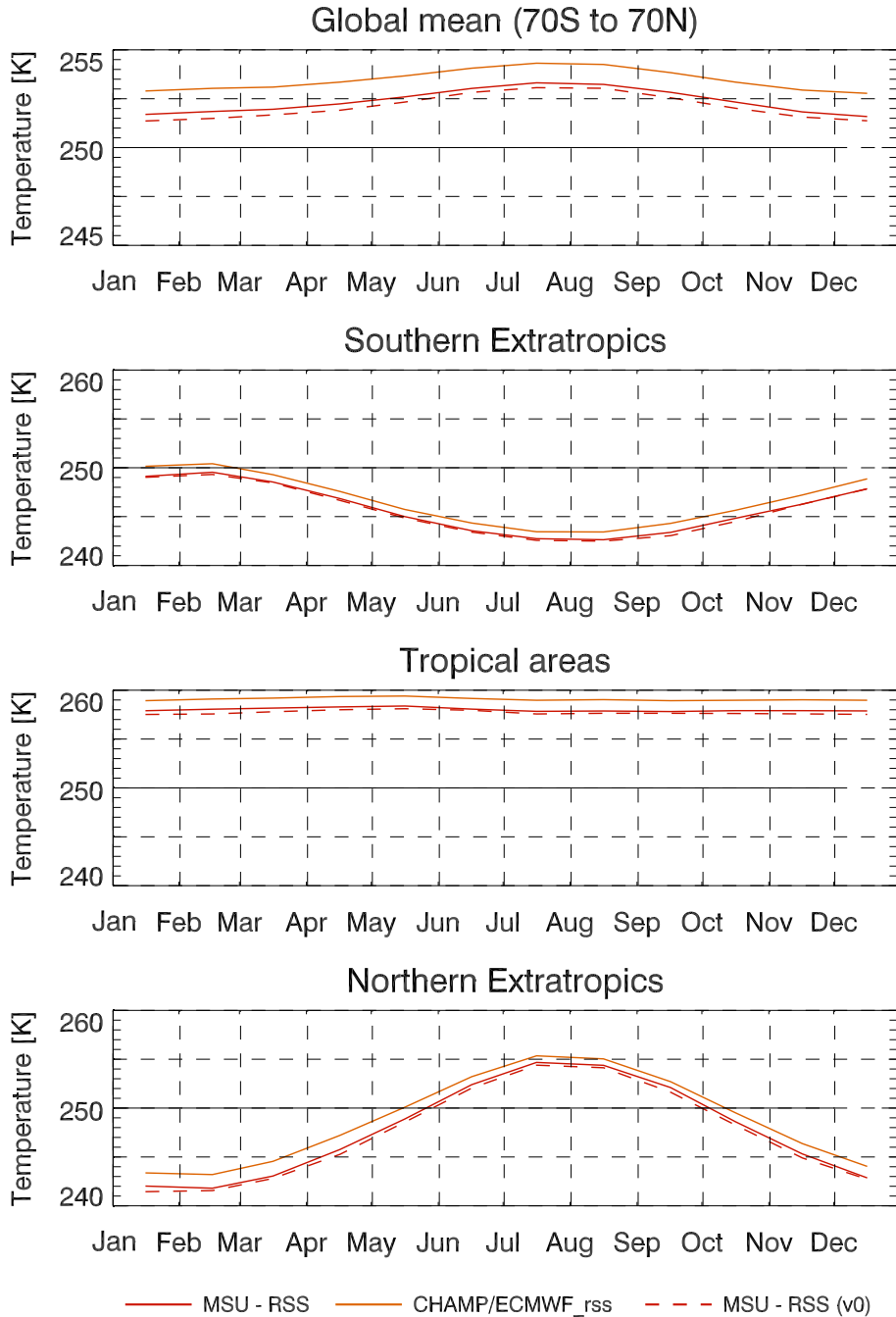


Figure 6.9: Temperature average of the mid troposphere from CHAMP/ECMWF ("CHAMP/ECMWF-RSS") and RSS ("MSU-RSS"). The MSU means are shown for Jan 1979 - Dec 1998 ("MSU-RSS (v0)") and for Sep 2001 - Dec 2005.

Mean Temperature of the Troposphere and Stratosphere

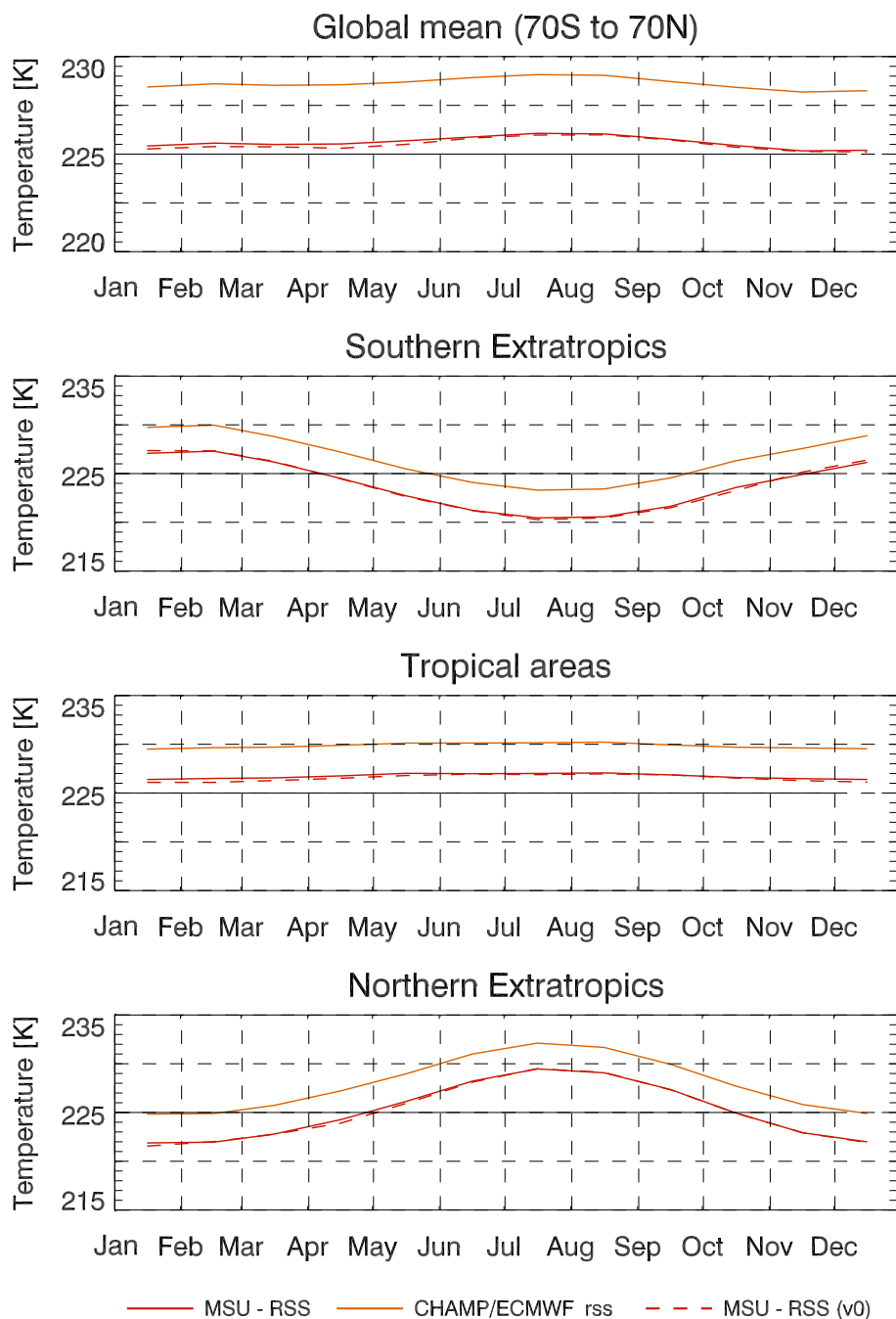


Figure 6.10: Temperature average of the troposphere and stratosphere from CHAMP/ECMWF ("CHAMP/ECMWF-RSS") and RSS. The MSU means are shown for Jan 1979 - Dec 1998 ("MSU-RSS (v0)") and for Sep 2001 - Dec 2005 ("MSU-RSS").

Mean Temperature of the Lower Stratosphere

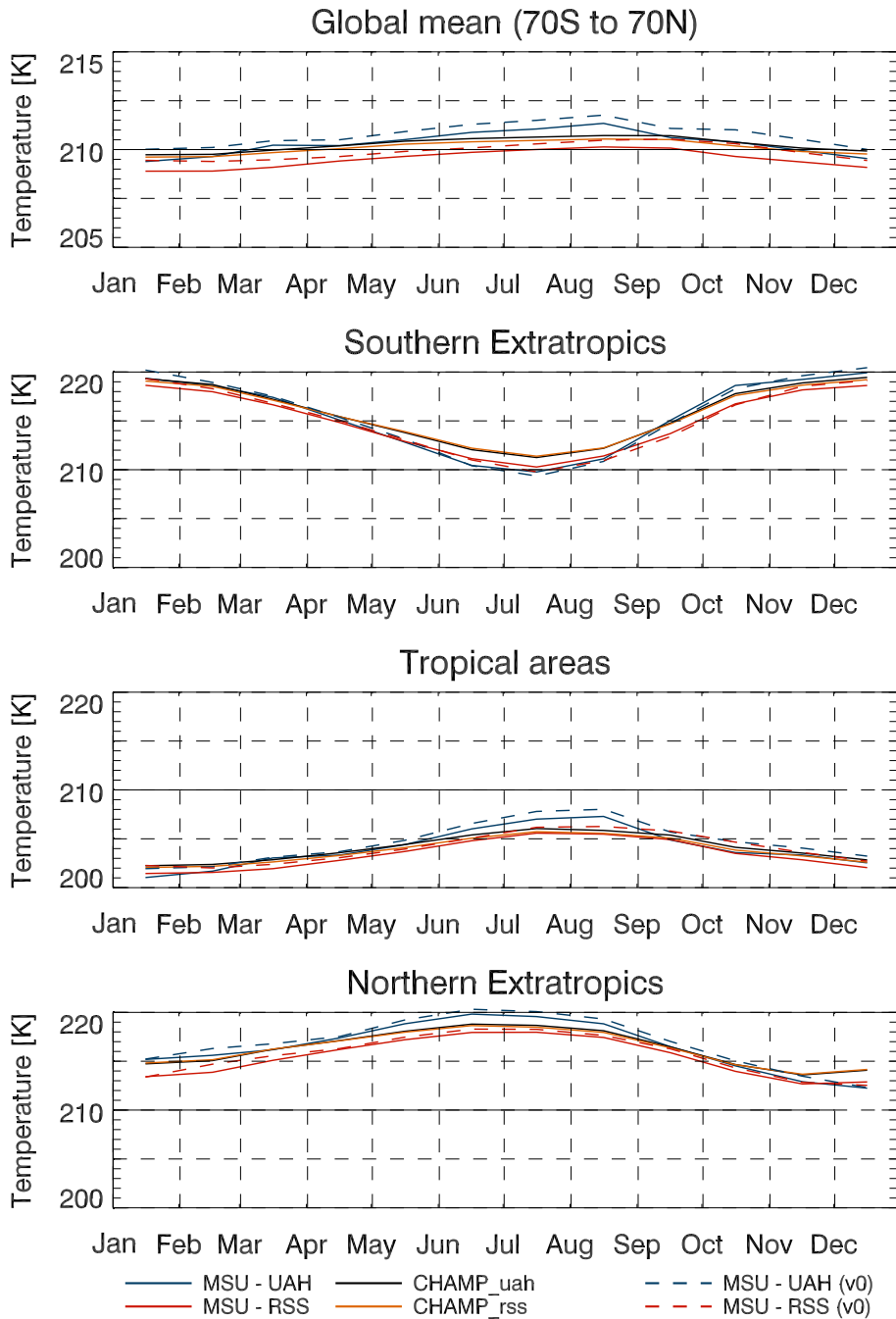


Figure 6.11: Temperature average of the lower stratosphere from CHAMP ("CHAMP-RSS" and "CHAMP-UAH"), UAH and RSS. The MSU means are shown for Jan 1979 - Dec 1998 ("MSU-RSS (v0)" and "MSU-UAH (v0)") and for Sep 2001 - Dec 2005 ("MSU-RSS", "MSU-UAH").

Monthly Mean Temperature relative to the Reference

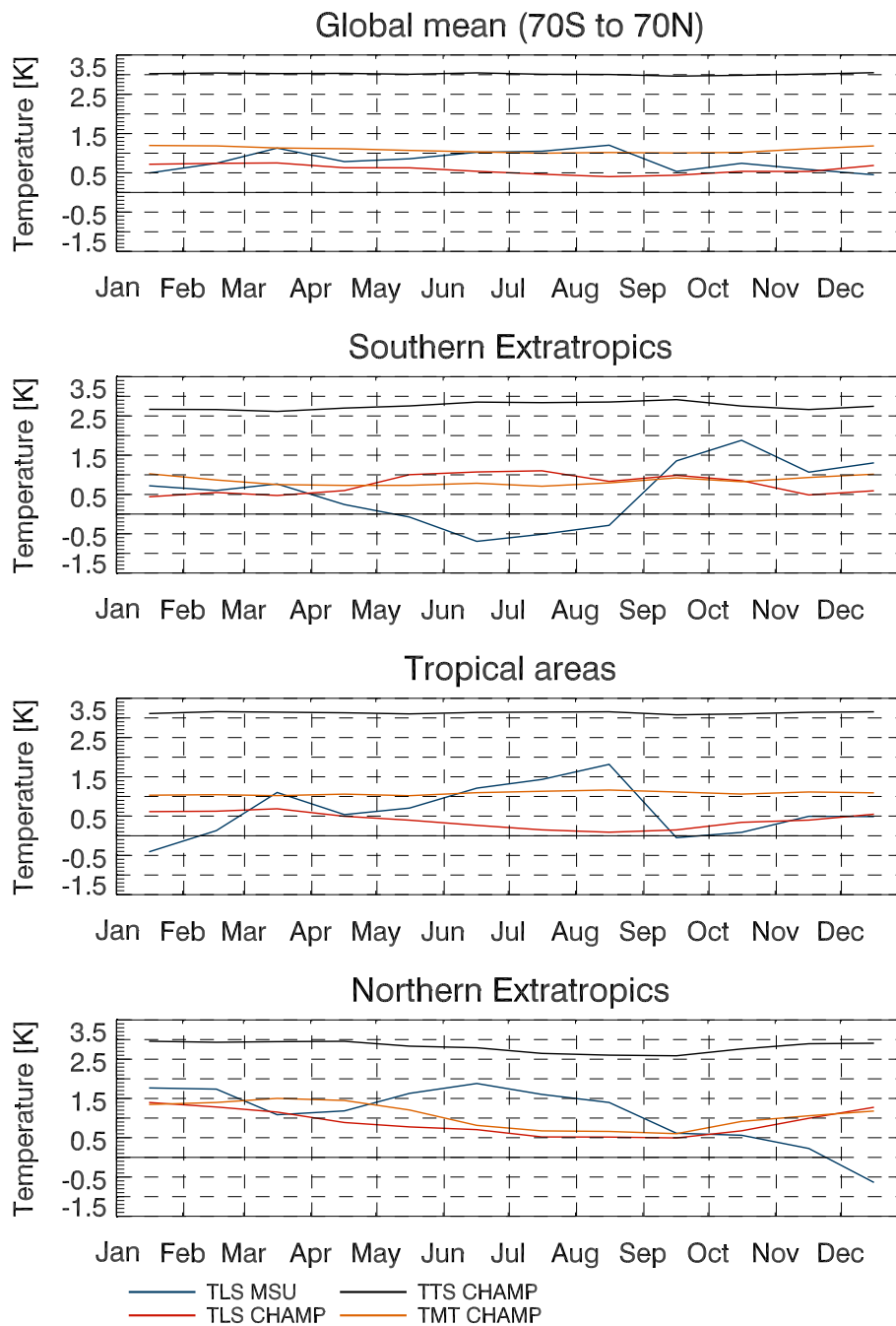


Figure 6.12: The difference between the observed monthly mean from MSU-UAH and CHAMP/ECMWF-RSS and from MSU RSS (the reference data set) for the layers TLS, TTS, and TMT for September 2001 - December 2005.

Monthly Mean Temperature relative to the Reference

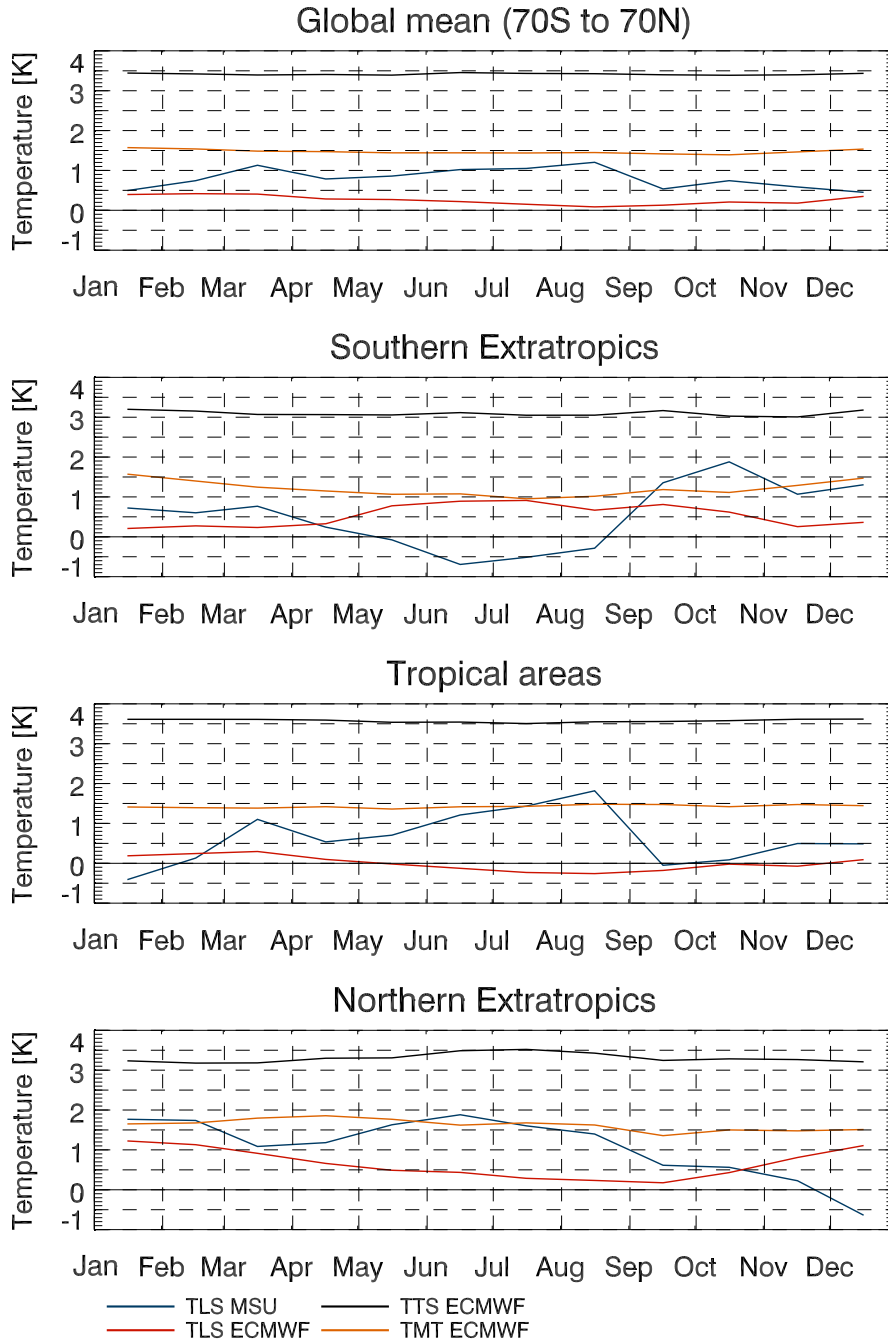


Figure 6.13: The difference between RSS weighted ECMWF profiles and MSU RSS (reference data set) for TLS, TTS, and TMT and between MSU UAH and MSU RSS for the period September 2001 - December 2005.

it is about 5 K. In fact, after applying the ECMWF profiles only and not the CHAMP climatologies, the difference relative to MSU increased, especially during summer and ranged between 1.9 K in April and 1.4 K in September (Figure 6.13).

In the SET, the difference between CHAMP/ECMWF and MSU ranges between 1 K during summer and 0.7 K between April and August. This difference increases up to 1.5-1.0 K, while using the ECMWF profiles only. Compare Figure 6.12 with Figure 6.13

The difference between CHAMP/ECMWF and MSU is about 3 K in the "upper" troposphere (Figure 6.10). The difference between MSU and ECMWF is a bit larger (3.4 K). Combined with CHAMP, the discrepancy ranges between almost 3 K (winter) and about 2.55 K (September) in the NET and between 2.9 K (winter) and 2.6 K (March) in the SET. The difference between MSU and ECMWF increases up to 3.2 K during winter and about 3.5 K in July in the NET and up to 3 K during winter and 3.2 K in January in the SET. Generally, the maximum of the CHAMP/ECMWF difference time series is located in winter and that of ECMWF in summer.

Also the TLS temperature difference relative to MSU RSS changes, if one considers the CHAMP profiles on the one hand and the ECMWF profiles only on the other hand (Figure 6.12, Figure 6.13). Globally, it ranges between 0.7 K in January and 0.4 K in August (CHAMP/ECMWF) and between 0.4 K in January and almost zero in August (ECMWF). The reason for the decrease of the monthly mean difference relative to MSU, might result from the error characteristics of ECMWF relative to CHAMP. Analyses have found a systematic cold bias in the tropical tropopause and also, with a less magnitude, in higher latitudes. For closer details apply e.g., [Borsche *et al.*, 2007]. In spring 2006, ECMWF improved the vertical resolution, with the result that the error became much smaller, but this happened after the analysis period of this study (September 2001 - December 2005).

The MSU processing centers show a systematic difference characteristic, which is comparable with that of the brightness temperature (Section 6.1). Relative to the recalculated MSU RSS monthly mean, the CHAMP result differs by 0.7 K in January and 0.4 K in August on the global average. In the tropics, the difference is slightly smaller and ranges between 0.6 K from January until March and by 0.1 K in August. Again, the inter-annual variability becomes much larger in the NET (1.4 K in January and 0.5 K between July and September) and in the SET (1.1 K in July and about 0.5 K between November and March).

6.3 Comparison of Temperature Anomalies

This section focuses on the temperature anomalies calculated by subtraction of the monthly mean (September 2001 - December 2005) reference from the absolute temperature. It is supposed to provide information about unusual warm or cold seasons and months.

In the mid troposphere, CHAMP/ECMWF measured the smallest differences from the monthly mean in the Tropics, where the anomalies ranged between +0.2 K and -0.2 K (Figure 6.14). This is quite similar to MSU RSS measurements, which have warmer anomalies than CHAMP/ECMWF before December 2004 and colder ones since then (≤ 0.1 K) (Figure

6.3 Comparison of Temperature Anomalies

6.15). But the magnitude of the difference time series is very small and ranges generally between ± 0.1 K (Figure 6.18).

On the global scale the anomalies were quite similar to the tropical ones. For both, July 2004 was the coldest month, while the warmest one is not clear, because for CHAMP/ECMWF the year 2005 was much warmer than the years before. For MSU the warmest month has been December 2003 and for CHAMP/ECMWF it has been September 2005. The CHAMP/ECMWF anomalies were warmer than the MSU ones in October 2001 and in the whole year 2005 (about 0.1 K) and colder in December 2001, April, August, and September 2003, and in April 2004 (-0.1 K).

Generally, the anomaly increased with latitude, while the CHAMP/ECMWF results showed a much higher variability than the MSU RSS ones. For instance, September 2002 was the warmest month in the SET especially at 65° S (CHAMP: 1.8 K, MSU: 1.2 K), as visible in Figure 6.20 and 6.15. Some more examples are as follows. In October 2002 at 55° N (contrary to the SET a relative cool month): CHAMP/ECMWF -1.0 K, MSU -0.6 K; in February 2004 at 65° N: CHAMP/ECMWF +1.0 K, MSU +0.6 K; in December 2004 at 65° N: CHAMP/ECMWF -1.4 K, MSU -0.9 K. The different variability is also visible on zonal scale. In the year 2005, the CHAMP anomaly was about 0.2 K higher than the MSU one, while it was colder in the years before. The behavior was actually the same in the Tropics, but with a smaller magnitude. Probably a trend exists in the difference time series between CHAMP/ECMWF and MSU (Figure 6.20).

In the NET, warm months were for MSU February 2002 (MSU: 0.4 K), December 2003 (MSU and CHAMP: 0.7 K) and April 2002 and the months August, September, and October 2005 (CHAMP/ECMWF: 0.4 K). During the last three mentioned months CHAMP/ECMWF measured about 0.3 K warmer anomalies than MSU. Rather cold months were October 2002 (CHAMP/ECMWF and MSU: -0.6 K) and December 2004 (CHAMP/ECMWF: 0.4 K). The CHAMP/ECMWF anomaly was about 0.25-0.4 K warmer than MSU in March and April 2002 and in February, August, and September 2005 (Figure 6.18) and colder than MSU in DJF 2001/02 (-0.3- -0.5 K), in July 2002 (-0.3 K), and between October and December 2004 (-0.2- -0.3 K).

In the SET warm anomalies were observed in December 2001 (CHAMP/ECMWF: 0.3 K) and June 2002 - September 2002 (CHAMP/ECMWF and MSU: 0.4-0.8 K) and rather cold months were June, August, and September 2003 (CHAMP/ECMWF: -0.4- -0.6 K) and November and December 2004 (CHAMP/ECMWF and MSU: -0.3 K). CHAMP/ECMWF observed warmer anomalies than MSU in JJA 2002 and in March, April, and July 2005 (+0.2 K) and colder ones from June 2003 until September 2003 (-0.2- -0.3 K).

In the "upper" troposphere, there were measured approximately the same anomalies as in the mid troposphere (Figure 6.14), while the sign was still the same for CHAMP/ECMWF and MSU in the most months. But globally, the year 2005 was a rather warm one for CHAMP/ECMWF and a rather cool one for MSU (Figure 6.16). During the total observation time period (Sep 2001 - Dec 2005) the difference between CHAMP/ECMWF and MSU RSS increases from -0.1 K (December 2001 - May 2002, September 2002) up to about 0.15 K in the year 2005 (Figure 6.18). In the Tropics, the anomalies ranged between -0.2 K and +0.2 K. They reached their maximum in the highest latitudes, while the CHAM-

6 Results and Discussion

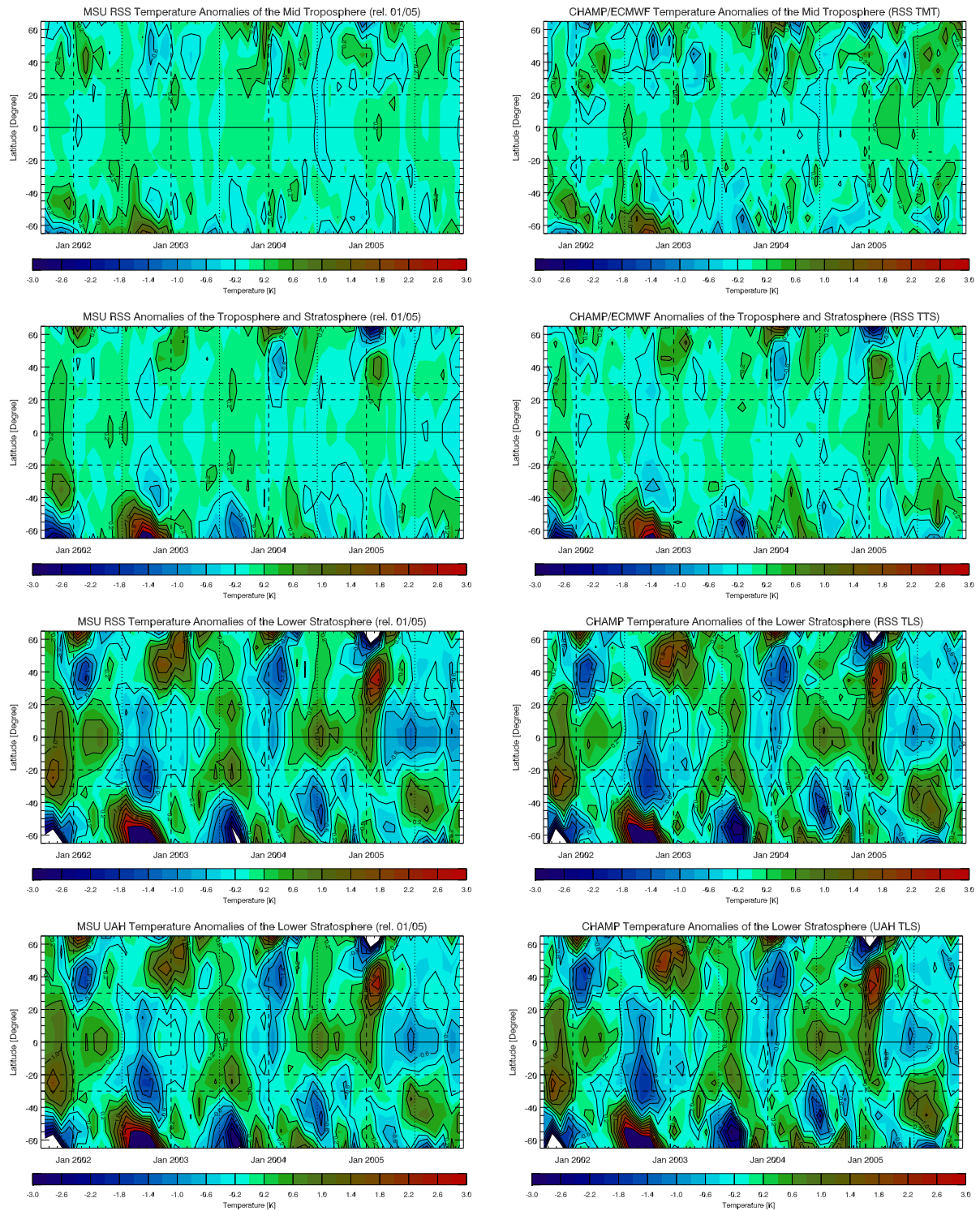


Figure 6.14: The temperature anomalies with respect to the averaged monthly mean brightness temperatures of the period September 2001 - December 2005. The layout follows mainly Figure 6.1.

Temperature Anomalies of the Mid Troposphere

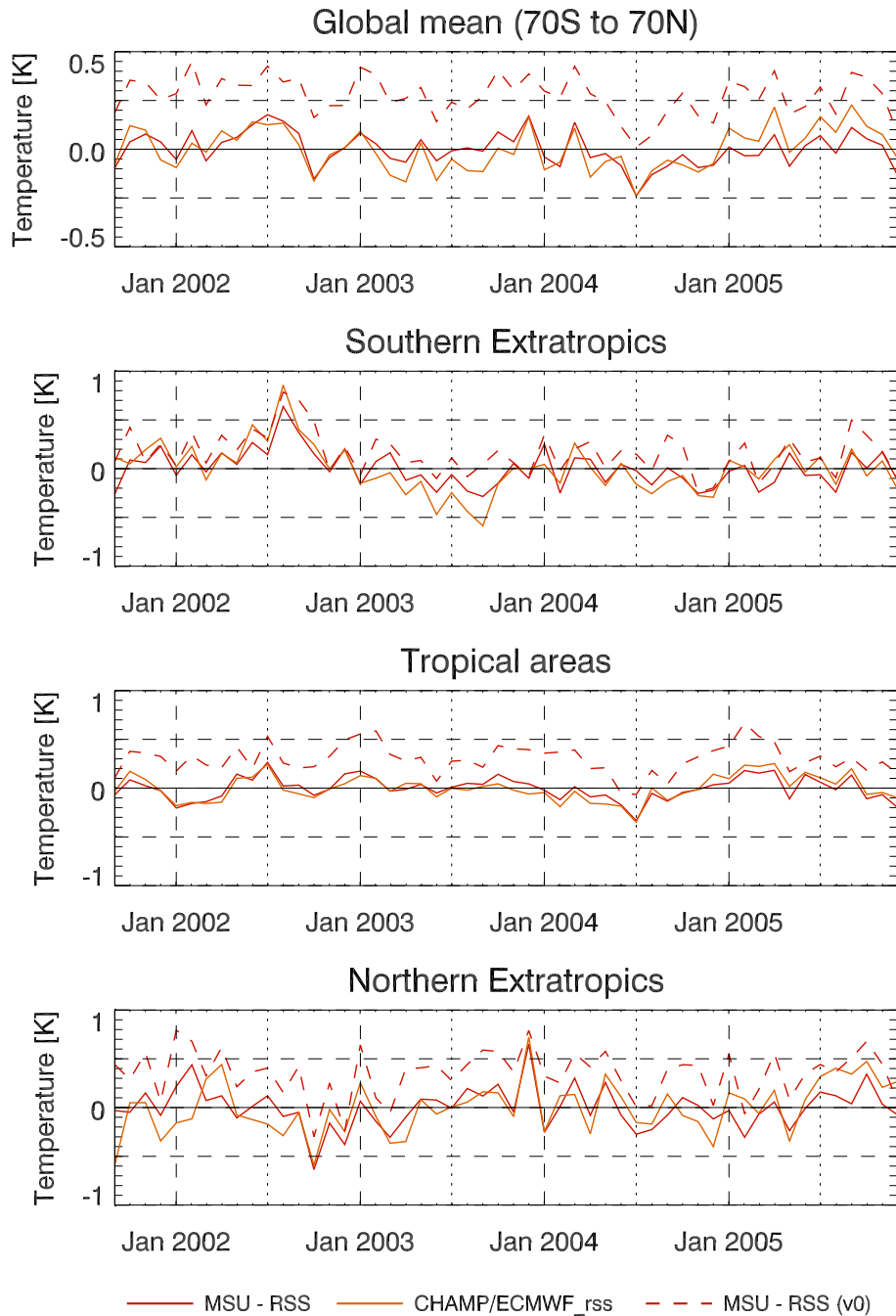


Figure 6.15: Temperature anomalies of the mid troposphere for CHAMP/ECMWF ("CHAMP/ECMWF-RSS") and RSS ("MSU-RSS") relative to the average of the period Jan 1979 - Dec 1998 ("MSU-RSS (v0)") and of Sep 2001 - Dec 2005.

Temp. Anom. of the Troposphere and Stratosphere

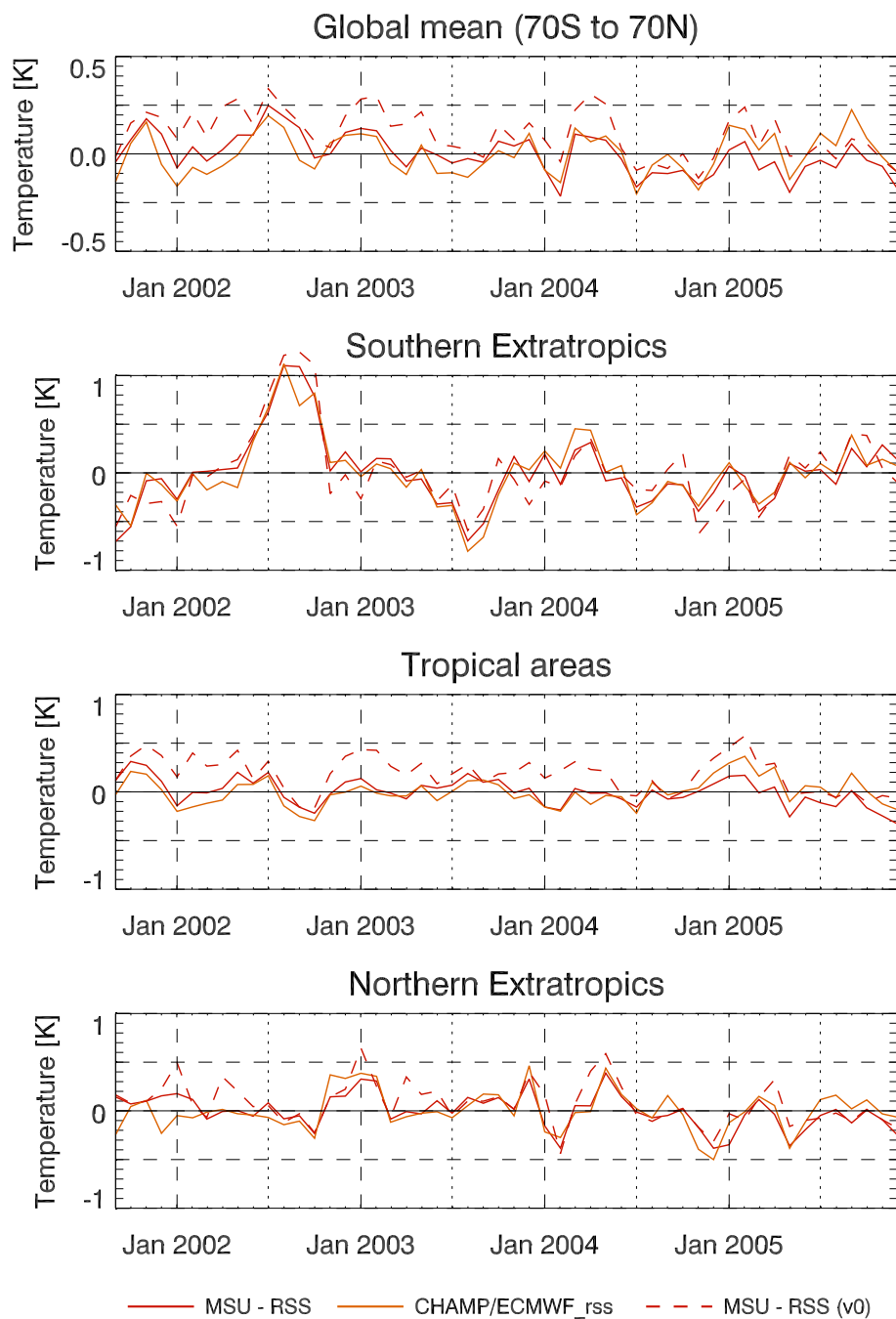


Figure 6.16: Temperature anomalies of the troposphere and stratosphere for CHAMP/ECMWF ("CHAMP/ECMWF-RSS") and RSS ("MSU-RSS") relative to the average of the period Jan 1979 - Dec 1998 ("MSU-RSS (v0)") and of Sep 2001 - Dec 2005.

6.3 Comparison of Temperature Anomalies

P/ECMWF anomalies were still larger than the MSU ones. For instance, in February 2005 at 15°N, CHAMP/ECMWF measured +0.4 K more than the monthly mean and MSU slightly more than zero. Generally this month was in the period with the largest anomaly discrepancy between CHAMP/ECMWF and MSU in the Tropics (December 2004 until December 2005), with about 0.2 K (Figure 6.18). Before December 2004, the anomalies were almost the same on the tropical scale. But CHAMP/ECMWF measured about 0.1 K colder anomalies than MSU RSS between September 2001 and May 2002. An important point is, that the difference time series seems to have a trend in the tropics.

In the NET, the CHAMP/ECMWF anomalies were quite large between November 2002 and February 2003 (+0.4 K), December 2003 (+0.45 K) and May 2004 (+0.4 K) and quite small in February, November and December 2004 (between -0.4 K and -0.5 K). At 65°N, the anomalies ranged between +1.0 K (MSU), 1.6 K (CHAMP/ECMWF) in January 2004 and -2.5 K (MSU), -2.6 K (CHAMP/ECMWF) in January 2005. These months showed quite large and transversed anomalies in the northern mid latitudes, while again the CHAMP/ECMWF ones were larger than those of MSU RSS. In the NET, the difference between the anomalies was quite large in November and December 2002 (0.2 K), September 2004 and January 2005 (0.2 K), and between June and September 2005 (about 0.15 K). Between November 2001 and February 2002 and in November 2004, it fell below -0.2 K. Generally, the differences developed similar to the TMT ones (Figure 6.16 and 6.18).

The period June 2002 - September 2002 has been the warmest one in the SET, with anomalies ranging between +0.8 K and +1.2 K (Figure 6.16). Then at 65°S, the temperature anomaly became even larger than 3 K. This is larger than in the mid troposphere but still smaller than in the lower stratosphere (Figure 6.14). Warm TTS anomalies were also measured in March and April 2003 (about 0.3 K) and after September 2005 and cold ones were observed until October 2001, in July, August and November 2004, in March and April 2005 (-0.3 K-0.4 K), and between June and September 2003 with a minimum of -0.6 K in August.

CHAMP/ECMWF measured colder anomalies than MSU between March 2002 and May 2002 (-0.2 K), in September 2002 (-0.4 K), and in August and September 2003 (≤ -0.1 K) and warmer anomalies than MSU between February and May 2004 and in August and September 2005 (about 0.1 K). Generally, CHAMP/ECMWF measured a higher variability than MSU in the SET and NET and in sum an almost similar variability in the Tropics (Figure 6.20). Generally, the anomalies were not the same in the mid troposphere and in the "upper" troposphere and showed an independent development of these layers.

In the lower stratosphere, the anomalies were about a factor two higher than in the layers below. On global scale they ranged between +0.6 K and -0.5 K and in the Tropics between +1.2 K and -1.2 K. The variability was larger in the NET and largest in the SET (± 1.6 K), which was dominated by the warm period July 2002 - September 2002 (1.5 K) and the relative cold period July 2003 - September 2003 (-1--1.5 K) (Figure 6.17).

Compared to MSU RSS, CHAMP showed colder anomalies in the first twelve months and warmer ones since April 2004 (on the global scale). Principally, the MSU anomalies of UAH and RSS agree quite well and also the differently weighted CHAMP temperature profiles agree to each other (either with the UAH or the RSS weighting function).

Temperature Anomalies of the Lower Stratosphere

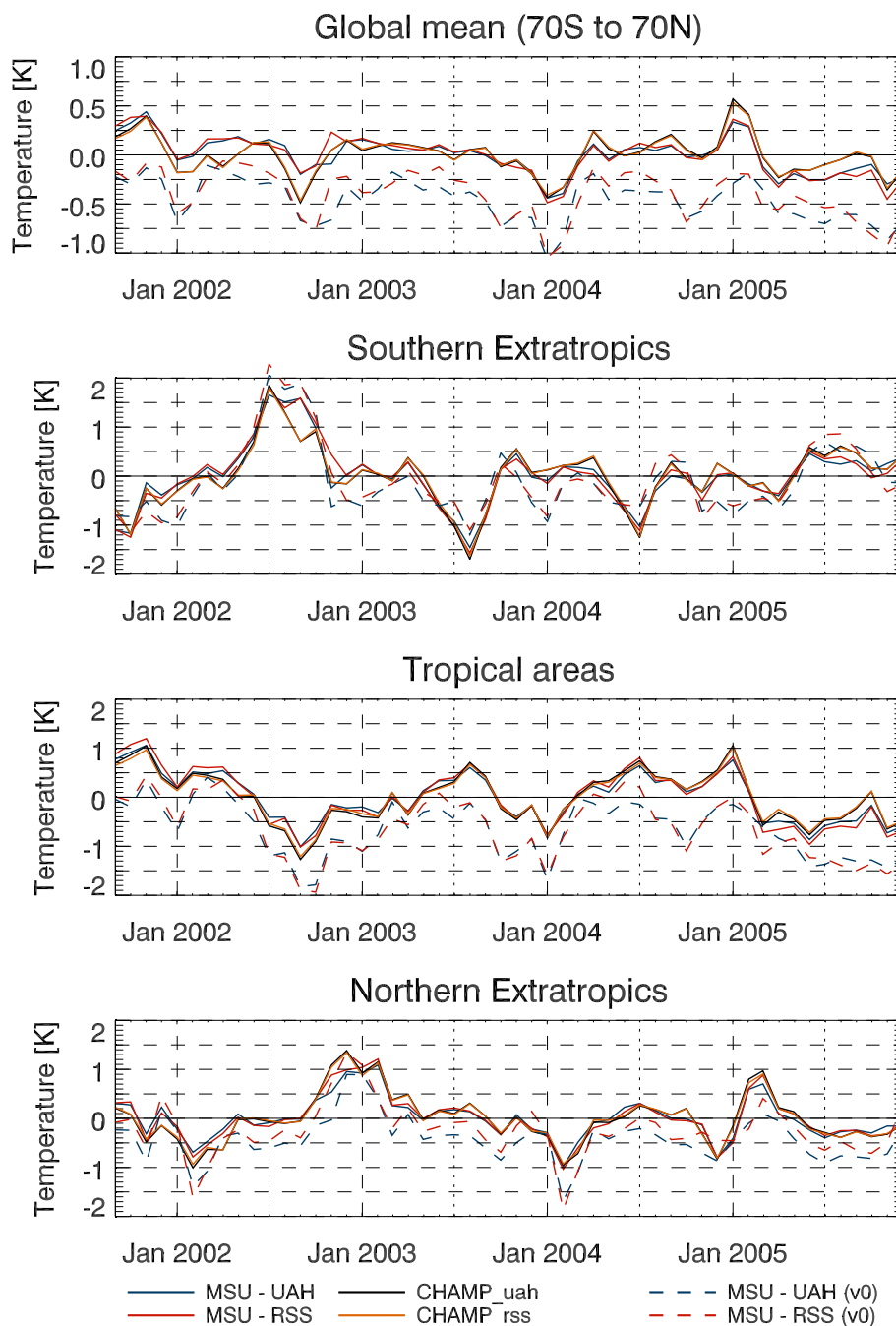


Figure 6.17: TLS anomalies for CHAMP, UAH and RSS relative to the average of the period Jan 1979 - Dec 1998 ("MSU-RSS (v0)" and "MSU-UAH (v0)") and of Sep 2001 - Dec 2005 ("MSU-RSS", "MSU-UAH", "CHAMP-RSS" and "CHAMP-UAH").

Temperature Anomalies relative to the Reference

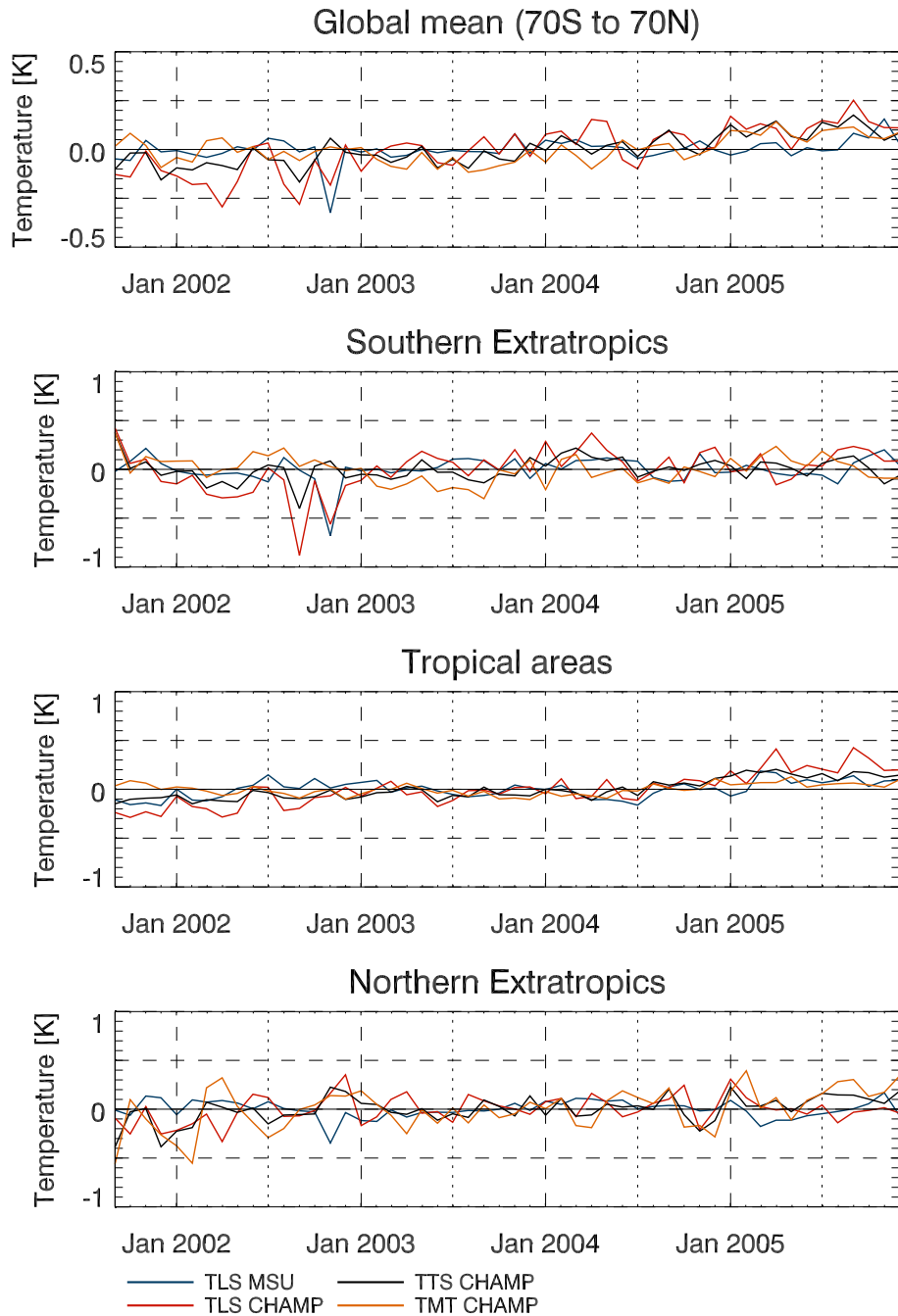


Figure 6.18: The difference of the temperature anomalies from MSU-UAH and CHAMP/ECMWF-RSS minus MSU RSS. For the layers TLS, TTS and TMT the anomalies relate to the period September 2001 - December 2005.

6 Results and Discussion

Differences existed between GPS RO and MSU as two ways to observe the atmospheric temperature with satellites, as shown in Figure 6.17. The temperature anomaly differences were smallest in the tropics, especially from October 2002 until December 2004 with less than 0.2 K (Figure 6.18). Before that period, (except January 2002) the difference fell continuously below -0.2 K and after that period, it raised up to 0.4 K in April and October 2005. In the SET, the difference was not large as well, but reached a minimum of -0.9 K in September 2002 and of -0.5 K two months later. Generally, the difference ranged between ± 0.2 K and reached -0.3 K from March until June 2002, +0.3 K in January and April 2004, and 0.25 K from August until October 2005 (Figure 6.18). MSU and CHAMP agreed well in the NET, where the difference exceeded +0.3 K in December 2002, October 2004, and January 2005 and fell below -0.3 K in April 2002. On the global scale, CHAMP measured colder anomalies than RSS from September 2001 until May 2002 (about -0.15 K with a maximum of -0.3 K in April) and warmer ones since January 2005 (about 0.15 K with a maximum of 0.25 K in September 2005). Between June 2002 and December 2004 the difference was very small. It ranged between ± 0.1 K and reached -0.2- -0.3 K in August and September 2002 and 0.15 K in April and May 2005. Generally, the difference time series seems to have a trend from negative to positive values in the lower stratosphere. Globally, the warmest months were January and February 2005, November 2001 and the coldest ones September 2002, January and February 2004, and November 2005. Strange is that during the relative cold and warm months, the higher latitudes of the SET or of the NET often showed strong anomalies of opposite sign. For instance in the southern hemispheric winter 2003, a very strong cold anomaly canceled the warm one of the other latitudes. Considering TMT, TTS, and TLS, the sign of the anomaly was mostly the same, only the magnitude increased with altitude.

In the SET relative cold months were October 2001 (-1.1 K), July, August, and September 2003 (between -1.0 K and -1.5 K) and July 2004 (-1.0 K). The warm winter 2002 is only visible on the SET mean with between +1.5 K and +2 K. The tropics experienced a warm TLS temperature in November 2001 (dominating the global sign) and January 2005. After September 2002 and January 2004, cold anomalies of larger than 0.5 K occurred only after March 2005, a period with the largest difference between CHAMP and MSU (Figure 6.17 and 6.18).

In the NET CHAMP measured quite warm anomalies during November 2002 and February 2003 (+1.0-1.4 K) and in February and March 2005 (+0.85 K). Interesting is here, that in January and February 2005 the anomaly dropped below -3 K in 65 °N. Relatively cold were February 2002 (-1.0 K), February 2004 (-0.9 K), and December 2004 (-0.8 K).

6.3 Comparison of Temperature Anomalies

CHAMP/ECMWF profiles (40N–50N): Several Months, 2005

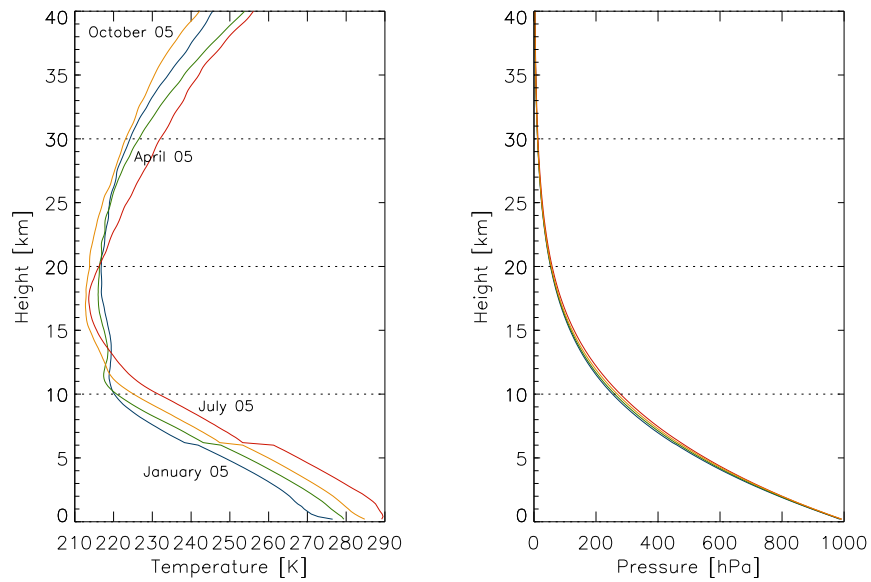


Figure 6.19: Exemplary CHAMP/ECMWF temperature (left) and pressure (right) observations for January (blue), April (green), July (red), and October (orange) to represent the main seasons for mid-latitudes (40°N - 50°N zonal mean).

6 Results and Discussion

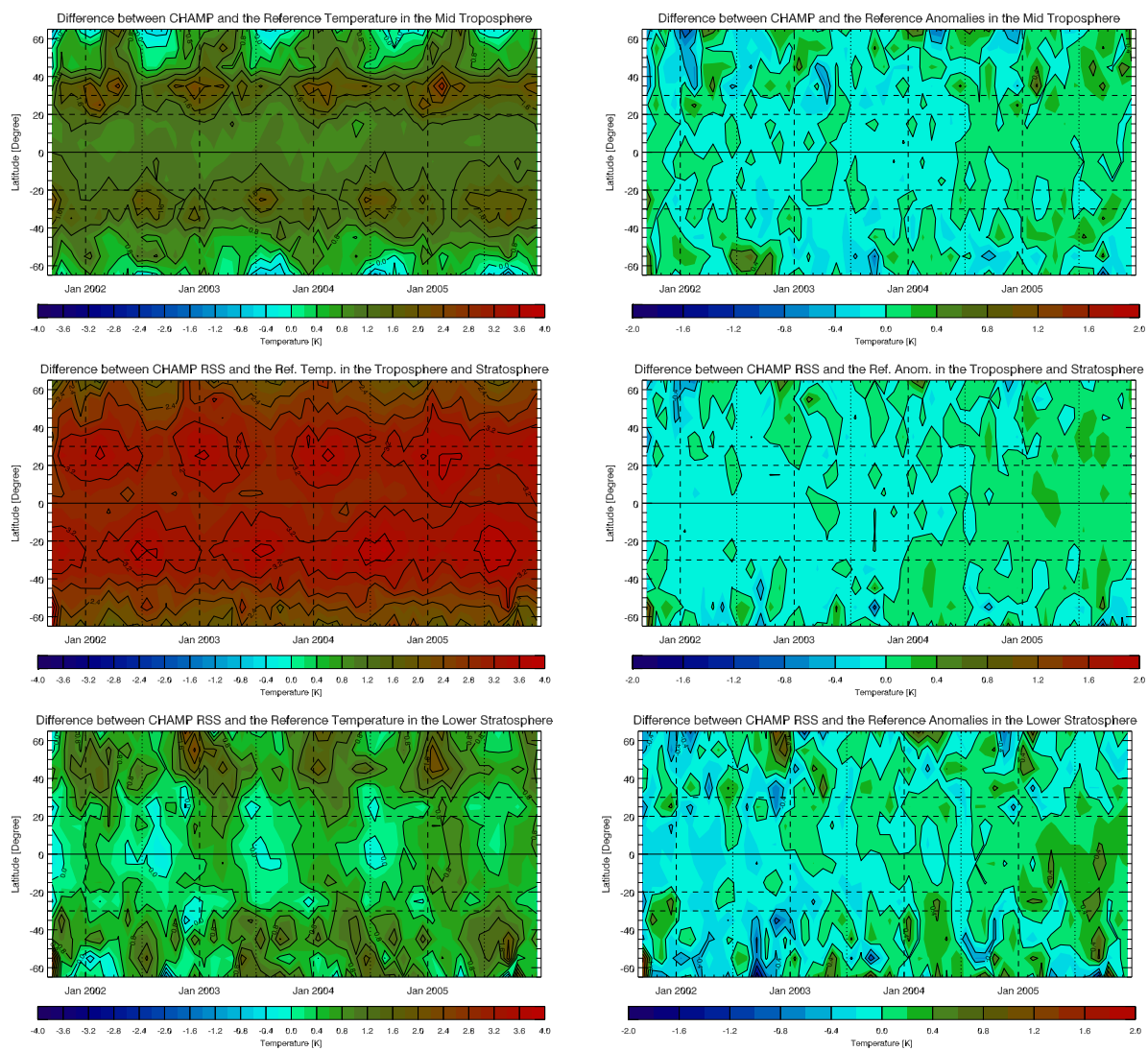


Figure 6.20: This figure shows the difference between CHAMP brightness temperature and MSU RSS (TMT, TTS, and TLS) in terms of absolute temperatures (left) and of anomalies (right).

7 Summary and Conclusions

In this thesis, microwave sounding unit (MSU) observations were validated and compared with radio occultation (RO) measurements. Monthly mean zonal mean temperature climatologies were investigated for three atmospheric bulk layers for the period September 2001 to December 2005.

Since September 2001 the CHAMP satellite makes RO observations of the atmosphere. It is managed by the GFZ Potsdam, which provides phase delay measurements and orbital data. The Wegener Center, University of Graz, uses them to retrieve atmospheric parameters like dry temperature and pressure profiles. In the moist layers of the atmosphere, the RO climatologies were additionally replaced by ECMWF analysis data in this thesis. The MSU data stem primary from the processing centers RSS (Remote Sensing System, Santa Rosa, California, USA) and UAH (University of Alabama, Huntsville, USA), which provided them in terms of temperature anomalies relative to the monthly mean of the period January 1979 to December 1998 for the lower stratosphere (TLS), the "upper" troposphere (troposphere stratosphere, TTS), and the mid troposphere (TMT).

Since the data are of completely different format¹, they were brought to the same basic resolution of 10° zonal means at three height layers. In this context, global MSU weighting functions were applied to compute synthetic CHAMP TLS and CHAMP/ECMWF TTS and TMT zonal mean monthly mean temperatures. From UAH, I used the TLS weighting function as a static function of pressure and from RSS the TLS, TTS, and TMT weighting functions as instantaneous values at given heights. The MSU time series were recalculated to temperature anomalies with respect to the monthly mean of the CHAMP observation period September 2001 - December 2005.

Then, a quasi-global mean between 70°S and 70°N and three larger zonal means were calculated representing the southern extratropics or SET (70°S - 30°S), the tropics (20°S - 20°N), and the northern extratropics or NET (30°N - 70°N). Finally, difference time series were computed relative to a reference, which was MSU RSS, to visualize the differences in the observed brightness temperature, temperature variability and temperature anomalies. Generally, the observed brightness temperatures range between 198 K and 227 K in the lower stratosphere, between 211 K and 230 K in the "upper" troposphere, and between 234 K and 258 K in the mid troposphere. The smallest inter-annual temperature variabilities are visible as expected on the global and the tropical scale. Globally the average annual cycle of the reference time series (MSU RSS) ranges between 208.9 K and 210.1 K

¹Zonal means of 10° latitudinal width at 200 m vertical resolution for CHAMP/ECMWF and a horizontal resolution of 2.5° × 2.5° at 3 vertical bulk layers for MSU

7 Summary and Conclusions

Data Source	Global	SET	Tropics	NET
<i>MSU UAH (TLS)</i>	0.5-1.8 K	-0.7-1.9 K	-0.4-1.8 K	-0.6-1.2 K
<i>CHAMP (TLS)</i>	0.4-0.8 K	0.4-1.1 K	0.1-0.7 K	0.5-1.4 K
<i>CHAMP/ECMWF (TTS)</i>	3.0-3.1 K	2.6-2.9 K	3.1-3.2 K	2.6-3.0 K
<i>CHAMP/ECMWF (TMT)</i>	1.0-1.2 K	0.7-1.0 K	1.0-1.2 K	0.6-1.5 K

Table 7.1: Overview of the difference between the observed annual cycle of the Sep 2001 - Dec 2005 averaged monthly mean temperatures of MSU UAH, CHAMP, and CHAMP/ECMWF from MSU RSS, which is the reference, for the layers TLS, TTS, and TMT (e.g., CHAMP/ECMWF minus MSU RSS).

for TLS, between 225.2 K and 226.1 K for TTS, and between 251.6 K and 253.3 K for TMT. The tropical variability is highest in the lower stratosphere (201.4 K - 205.6 K) and much smaller below (227.1 K - 226.4 K for TTS and 257.8 K - 258.4 K for TMT). The variability is much higher in the extratropics, which is as follows for TLS: 210.3 K - 218.6 K (SET) respectively 218.0 K - 212.7 K (NET), for TTS: 220.5 K - 227.3 K (SET) respectively 221.9 K - 229.5 K (NET), and for TMT: 242.6 K - 249.5 K (SET) respectively 241.8 K - 254.7 K (NET).

The difference of absolute temperature between CHAMP/ECMWF and the reference is smallest for TLS (0.4-1.4 K). It is higher for TMT (0.6-1.5 K) and highest for TTS (2.6-3.1 K), as listed in Table 7.1. Interesting is the inter-annual cycle of the CHAMP(/ECMWF) - MSU RSS difference time series in the extratropics, which have the minimum in summer and the maximum in winter (except TMT of the SET). As a test, we used ECMWF only (no CHAMP) climatologies with the result, that the TLS difference series decreased, while TTS and TMT increased, especially during the summer months.

The difference between the absolute temperatures may arise due to an offset in the MSU absolute temperatures (referenced to the NOAA-6 temperatures) and that the weighting functions are supposed to be better applied on the anomaly time series (recommendation from John Christy, UAH). Furthermore, the RSS weighting functions were provided as instantaneous values of height and not as static functions of pressure, as it is expected from the physical concept of the microwave sounding. *Steiner et al.* [2007] compared synthetic TLS temperatures from CHAMP calculated either with a global weighting function or with the radiative transfer model RTTOV. They found that for the TLS temperature the difference is below 0.2 K for larger zonal means. Thus, the global weighting functions are adequate for the calculation of synthetic TLS temperatures but seem to introduce an offset of about 3 K in case of TTS (Figure 6.3). As a test RTTOV was used to calculate TTS temperatures for one exemplary month (January 2006) with the result that the offset disappeared.

The anomalies between MSU RSS and CHAMP/ECMWF agree best in the tropical mid troposphere (Table 7.2). The CHAMP TLS and CHAMP/ECMWF TTS anomalies are colder in the beginning of the investigated period and warmer at the end, which is also visible on the global scale. Globally the difference between the TMT anomalies ranges between

Data Source	Global	SET	Tropics	NET
<i>MSU UAH (TLS)</i>	-0.32–0.16	-0.68–0.21	-0.17–0.19	-0.35–0.17
<i>CHAMP (TLS)</i>	-0.29–0.25	-0.88–0.42	-0.29–0.43	-0.33–0.35
<i>CHAMP/ECMWF (TTS)</i>	-0.17–0.18	-0.40–0.38	-0.15–0.20	-0.39–0.23
<i>CHAMP/ECMWF (TMT)</i>	-0.12–0.14	-0.30–0.38	-0.10–0.13	-0.56–0.39

Table 7.2: Overview of the difference between the observed temperature anomalies of MSU UAH, CHAMP, and CHAMP/ECMWF against MSU RSS, which is the reference, for the layers TLS, TTS, and TMT (e.g., CHAMP/ECMWF minus MSU RSS).

-0.12 K and 0.14 K. CHAMP/ECMWF TMT shows warmer anomalies during relative warm months and colder ones during relative cold months. In other words the variability of the TMT anomalies is higher than that of MSU, which is visible in e.g., April 2003, December 2003, December 2004, and October 2005 for the NET and in, e.g., June 2002, August 2002, June 2003, and September 2003 for the SET (Figure 6.15).

The difference of the TTS anomalies is of similar magnitude and ranges between -0.17 K and 0.18 K on the global scale. The change of the difference over time is quite well visible in Figure 6.16 and 6.18. The best agreements are again found in the tropics especially in the years 2003 and 2004. The agreement between the CHAMP/ECMWF and MSU RSS TTS anomalies is about the same as for TMT. Relative warm and cold months were, e.g., December 2003, February 2004, May 2004, and December 2004 for the NET and, e.g., August 2002, September 2002, August, 2003, September 2003, and March 2004 for the SET (Figure 6.16).

In the lower stratosphere the difference of the anomalies between CHAMP and MSU is larger than in the layers below and ranges between -0.29 K and 0.25 K. Generally the anomalies are much higher there than in the mid or in the "upper" troposphere and range between about ± 1 K in all regions with a few exceptions (Figure 6.17). Relative warm and cold months were, e.g., February 2002, December 2002, February 2003, February 2004, and March 2005 for NET and, e.g., September 2002, July 2004, January 2005, and June 2005 for the Tropics and, e.g., July 2002, September 2002, August 2003, and July 2004 for SET. Overall, representative brightness temperature results were derived for TLS. But in the case of TTS and TMT temperatures, the results have to be interpreted with caution since CHAMP dry temperatures are combined with ECMWF physical temperatures (Figure 6.19). Furthermore it is preferable to use a radiative transfer model instead of global weighting functions to calculate TTS and TMT temperatures for future applications.

7 Summary and Conclusions

List of Symbols

a	...	Impact parameter [m]
a_0, a_1, a_2	...	Coefficients of the quadratic approximation
\mathbf{B}	...	Magnetic induction [T]
B	...	Intensity of light [W m^{-2}]
B_{par}	...	Earth's magnetic field parallel to the EM wave propagation [T]
C	...	Constant in the reduced Appelton-Hartree formula [$40.3 \text{ m}^3 \text{ s}^{-2}$]
$C_{\text{raw}}, C_{\text{earth}}$...	Measured and corrected number of counts of the footprint
$C_{\text{space}}, C_{\text{target}}$...	Received number of counts from the space and from the hot target
c	...	Velocity of electromagnetic waves [m s^{-1}]
c_0	...	The speed of light in vacuum [$299792458 \text{ m s}^{-1}$]
\mathbf{D}	...	Dielectric displacement [C m^{-2}]
E	...	Energy [J]
\mathbf{E}	...	Electric field strength [V m^{-1}]
e	...	Water vapor pressure [hPa]
g	...	Terrestrial gravity [9.81 m s^{-2}]
g_0, g_s	...	Weight of the highest pressure level and of the sealevel [hPa^{-1}]
\mathbf{H}	...	Magnetic field strength [A m^{-1}]
\hbar	...	Planck's Constant [$1.055 \times 10^{-34} \text{ J s}$]
\mathbf{j}	...	Current density [A m^{-2}]
K	...	Const. in the Appelton-Hartree formula [$1.13 \times 10^{-12} \text{ m}^3 \text{ T}^{-1} \text{ s}^{-3}$]
k	...	Boltzmann Constant [$1.381 \times 10^{-23} \text{ J K}^{-1}$]
k_1, k_2, k_3, k_4	...	Pseudo constants in the Smith-Weintraub refractivity formula
L_c	...	Ionosphere corrected optical path [m]
L_k	...	Optical path of signal k , while k is either 1 or 2 (L_1, L_2) [m]
\mathbf{M}	...	Magnetic polarization
M_d	...	Molar mass of dry air [$0.02897 \text{ kg mol}^{-1}$]
N	...	Refractivity [1]
N_e	...	Electron density [m^{-3}]
N_k^{IO}	...	Refractivity of the ionosphere for signal L_k [1]
N^{NE}	...	Refractivity of the neutral atmosphere [1]
n	...	Refractive index of a medium [1]
\mathbf{P}	...	Mean electric dipole moment per volume
p, p_{dry}	...	Pressure of moist and dry air [Pa]
p_s	...	Pressure at the sealevel [$\text{bar} \equiv 10^5 \text{ Pa}$] or [N m^{-2}]
R_{mol}	...	Molar gas constant [$8.3145 \text{ J mol}^{-1} \text{ K}^{-1}$]
R	...	Universal gas constant of dry air [$287 \text{ J kg}^{-1} \text{ K}^{-1}$]
r	...	The Earth's Radius [6371 m]
\mathbf{r}	...	Position vector relative to the center of refraction
r_1, r_2	...	Distance of the refraction points R_1, R_2 from the Earth's center
r_G, r_L	...	Distance of the GPS and LEO sat. from the center of refraction [m]
r_k	...	Extra optical path of signal L_k due to receiver noise [m]

7 Summary and Conclusions

S_0	...	Solar Constant [1367 W m^{-2}]
S_k	...	Ray path of signal L_k [m]
\mathbf{s}	...	Unit vector in ray direction
T, T_{dry}	...	Temperature of moist and dry air [K]
$T_{850-300}$...	Free atmospheric temperature between 850 hPa and 300 hPa
T_a, T_b	...	Atmosphere and brightness temperature [K]
T_{bias}	...	Temperature bias [K]
T_e, T_s	...	Emission and surface temperature [K]
T_s	...	Temperature at the sealevel [K]
$T_{\text{space}}, T_{\text{target}}$...	Temperature of the space and of the MSU Hot Target [K]
t	...	Time [s]
V	...	Volume [m^3]
v_G^t, v_G^r	...	Tangential and radial velocity of the GPS satellite [m s^{-1}]
v_L^t, v_L^r	...	Tangential and radial velocity of the LEO satellite [m s^{-1}]
W	...	Weighting function [hPa^{-1}]
Z	...	Geopotential height above sealevel [m]
z	...	Altitude above sealevel [m]
α, α_c	...	Universal and Ionospheric corrected (c) bending angle [rad]
α_1, α_2	...	Angle of reflection at the refraction points R_1 and R_2 [rad]
α_k	...	Total bending angle of signal L_k [rad]
α_p	...	Planetary Albedo [1]
β_1, β_2	...	Angle of incidence at the refraction points R_1 and R_2 [rad]
χ_e, χ_m	...	Electric and magnetic susceptibility [1]
ϵ_0, ϵ_r	...	Permittivity of vacuum [$\text{A s V}^{-1} \text{ m}^{-1}$] and of medium r [1]
Φ	...	Angle between the ray direction \mathbf{s} and the \mathbf{r} -axis [rad]
Φ_k	...	Recorded phase of signal L_k in number of cycles [1]
ϕ	...	Latitude [deg]
Γ	...	Lapse Rate [K m^{-1}]
γ	...	Spherical angle between the GPS and the LEO satellite [rad]
γ_k^I	...	Extra optical path of signal L_k due to refraction in the ionosphere [m]
γ_k^N	...	Extra optical path due to refraction in the neutral atmosphere [m]
γ^V	...	Vacuum path between GPS and LEO (i.e. CHAMP) [m]
λ	...	Wavelength [m]
μ_0, μ_r	...	Permeability of vacuum [$\text{V s A}^{-1} \text{ m}^{-1}$] and medium r [1]
ν	...	Frequency [Hz]
ν_0	...	Atomic clock frequency [10.23 MHz]
ν_d	...	Doppler shift of the frequency [Hz]
ν_k	...	Frequency of signal L_k , while k is either 1 or 2 [hPa]
ρ, ρ_{dry}	...	Density of "wet" and dry air [kg m^{-3}]
$\rho_{\text{bound}}, \rho_{\text{el}}$...	Number of bounded and free charges
ρ_{total}	...	Total charge density of a material [C m^{-3}]
σ	...	Stefan-Boltzmann-Constant [$5.67 \times 10^{-8} \text{ W m}^{-2} \text{ K}^{-4}$]
$\hat{\sigma}$...	Conductivity [$\Omega \text{ m}^{-1}$]
Θ_G	...	Angle between ray direction and the center to GPS-satellite line [rad]
Θ_L	...	Angle between ray direction and the center to LEO-satellite line [rad]
τ	...	Optical Thickness

List of Abbreviations

AMSU	...	Advanced Microwave Sounding Unit
CA	...	Coarse Acquisition
CHAMP	...	Challenging Mini-satellite Payload
COSMIC	...	Constellation Observing System for Meteorology
ECMWF	...	European Center for Medium-range Weather Forecast
EM	...	Electro-Magnetic
EQUARS	...	Brazilian Equatorial Atmosphere Research Satellite
EUMESAT	...	European Meteorological Satellite Organization
GCM	...	Global Circulation Model
GFZ	...	GeoforschungsZentrum Potsdam, Germany
GLONASS	...	Global Navigation Satellite System, Russian GNSS
GNSS	...	Global Navigation Satellite Systems
GPS	...	Global Positioning System, US GNSS
GRACE	...	Gravity Recovery and Climate Experiment
GRAS	...	GNSS Receiver for Atmospheric Sounding
IGAM	...	Institute for Geophysics, Astrophysics and Meteorology University of Graz, Austria
ITOS	...	Improved TIROS Operational System
JPL	...	Jet Propulsion Laboratory
LEO	...	Low Earth Orbiter
MRIR	...	Medium Resolution Infrared Radiometer
MSU	...	Microwave Sounding Unit
NASA	...	National Aeronautics and Space Administration, USA
NET	...	Northern Extratropics (30°N-70°N)
NOAA	...	National Oceanographic and Atmospheric Administration, USA
NWP	...	Numerical Weather Prediction model
PCM	...	Parallel Climate Model, NCAR, Boulder, Colorado, USA
PRN	...	Pseudo Random Noise
RO	...	Radio Occultation
RSS	...	Remote Sensing System, Santa Rosa, California, USA
SET	...	Southern Extratropics (30°S-70°S)
SIRS	...	Infrared Spectrometer
TIROS	...	Television and Infrared Observation Satellite
TMT	...	Temperature of the Mid Troposphere
TLS	...	Temperature of the Lower Stratosphere
TLT	...	Temperature of the Low Troposphere
TTS	...	Temperature of the Troposphere and Stratosphere
UAH	...	University of Alabama, Huntsville, USA

7 Summary and Conclusions

List of Figures

2.1	The climate system	3
2.2	Annual mean radiation balance	5
2.3	Zonal mean radiation balance	6
2.4	Longwave absorption spectrum	7
2.5	The structure of the atmosphere	8
2.6	Zonal mean temperature for January, July, and the total year	9
2.7	Anthropogenic greenhouse gas emitters	15
2.8	Observed temperature trends in the free atmosphere and at the surface . .	21
2.9	Observed temperature of the free atmosphere and the surface since 1958 .	22
3.1	Microwave absorption spectrum of O ₂	24
3.2	All temperature weighting functions	28
3.3	Image from Tiros-1 and the AMSU-A1 instrument	29
3.4	NOAA satellite in space and the MSU/AMSU weighting functions	30
3.5	Orbital path of a single NOAA satellite	31
3.6	MSU cross track scan	32
3.7	The equator crossing local time of all NOAA satellites	33
3.8	Orbital subtrack from a single NOAA satellite	34
3.9	MSU RSS temperature trends of TLS, TTS, and TMT	38
3.10	The zonal mean and global mean TMT trends from UAH and RSS	39
3.11	Difference between the UAH and the RSS TMT trend	41
4.1	The CHAMP satellite in space	43
4.2	Construction of the GFZ RO measurement system and the data output . .	45
4.3	The geographical distribution of occultation events per day and per month	46
4.4	The construction of the CHAMP satellite	47
4.5	The main components of the CHAMP RO infrastructure	48
4.6	Geometry of an occultation event	54
5.1	CHAMP and ECMWF temperature and pressure profiles	64
5.2	CHAMP/ECMWF climatology retrieved for July 2005	66
5.3	MSU TLS brightness temperature from RSS	67
5.4	MSU RSS and MSU UAH weighting functions for TLS, TTS, TMT, and TLT	69
5.5	The regridded UAH and RSS weighting functions	71
5.6	CHAMP/ECMWF temperature profiles as a function of pressure	73

List of Figures

5.7	Global distribution of land and ocean	74
6.1	Brightness temperature from MSU and CHAMP/ECMWF	80
6.2	TMT brightness temperature	83
6.3	TTS brightness temperature	84
6.4	TLS brightness temperature	85
6.5	The difference between the observed brightness temperatures	86
6.6	Monthly mean temperature from MSU	89
6.7	The difference between the MSU monthly means	90
6.8	Monthly mean temperature from CHAMP in comparison to MSU RSS	92
6.9	TMT monthly mean temperature	93
6.10	TTS monthly mean temperature	94
6.11	TLS monthly mean temperature	95
6.12	The difference between the observed monthly means	96
6.13	The difference between the ECMWF and MSU RSS monthly means	97
6.14	Temperature anomalies from MSU and CHAMP/ECMWF	100
6.15	TMT temperature anomalies	101
6.16	TTS temperature anomalies	102
6.17	TLS temperature anomalies	104
6.18	The difference between the observed temperature anomalies	105
6.19	CHAMP/ECMWF temperature and pressure profiles for four months	107
6.20	CHAMP/ECMWF temperature and anomalies in comparison to MSU RSS	108

List of Tables

2.1	Composition of the atmosphere	8
2.2	Concentration of the most important greenhouse gases	17
2.3	Surface temperature trends in the 20 th century	18
3.1	Global RSS and UAH TMT trends	42
5.1	The relative distribution of land and ocean	74
7.1	Overview of the difference between the observed monthly means	110
7.2	Overview of the difference between the observed temperature anomalies . .	111

List of Tables

Bibliography

- Ao, C., T. Meehan, G. Hajj, A. Mannucci, and G. Beyerle (2003), Lower troposphere-refractivity bias in GPS occultation retrievals, *J. Geophys. Res.*, *108*(D18), 4577, doi:10.1029/2002JD003216.
- Baede, A., E. Ahlonsou, Y. Ding, D. Schimel, B. Bolin, and S. Pollonais (2001), *Climate Change 2001: The Scientific Basis, Contribution of Working Group 1 to the Third Assessment Report of the Intergovernmental Panel of Climate Change*, chap. The Climate System: An Overview, pp. 87–98, Cambridge University Press.
- Bassiri, S., and G. Hajj (1993), Higher-order ionospheric effects on the GPS observables and means of modeling them, *Manuscr. Geod.*, *18*, 280–289.
- Bevis, M., S. Businger, S. Chriswell, T. Herring, R. Anthes, C. Rocken, and R. Ware (1994), GPS meteorology: Mapping zenith wet delays onto precipitable water vapour, *J. Appl. Met.*, *33*, 379–386.
- Beyerle, G., J. Wickert, T. Schmidt, and C. Reigber (2004), Atmospheric sounding by GNSS radio occultation: An analysis of the negative refractivity bias using CHAMP observations, *J. Geophys. Res.*, *109*(D01106), doi:10.1029/2003JD003922.
- Born, M., and E. Wolf (1999), *Principles of optics*, 7 ed., Cambridge University Press, Cambridge, U.K.
- Borsche, M., A. Gobiet, A. Steiner, U. Foelsche, G. Kirchengast, T. Schmidt, and J. Wickert (2006), Pre-operational retrieval of radio occultation based climatologies, in *Atmosphere and Climate: Studies by Occultation Methods*, edited by U. Foelsche, G. Kirchengast, and A. Steiner, pp. 315–323, Springer Verlag, Berlin, Heidelberg, doi: 10.1007/3-540-34121-8_26.
- Borsche, M., G. Kirchengast, and U. Foelsche (2007), Tropical tropopause climatology as observed with radio occultation measurements from CHAMP compared to ECMWF and NCEP, *Geophys. Res. Lett.*, *34*(L03702), doi:10.1029/2006GL027918.
- Budden, K. (1985), *The propagation of radio waves*, Cambridge University Press, Cambridge, U.K.
- Chahine, M. (1983), Interaction mechanisms within the atmosphere, *Manual of Remote Sensing*, *1*(2), 888–896.

Bibliography

- Christy, J., and R. Spencer (2003), Reliability of satellite data sets, *Science*, *301*, 1046–1049.
- Christy, J., R. Spencer, and R. McNider (1995), Reducing noise in the MSU daily lower-tropospheric global temperature dataset, *J. Climate*, *8*, 888–896.
- Christy, J., R. Spencer, and S. Lobl (1998), Analysis of the merging procedure for the MSU daily temperature time series, *J. Climate*, *11*, 2016–2041.
- Christy, J., R. Spencer, W. Norris, and W. Braswell (2003), Error estimates of version 5.0 of MSU-AMSU bulk atmospheric temperatures, *J. Atmos. Ocean. Technol.*, *20*, 613–629.
- Demtröder, W. (1999), *Elektrizität und Optik, Experimentalphysik*, vol. 2, 2 ed., Springer, Berlin, Heidelberg, New York, Germany, 3-540-65196-9.
- ECMWF (2004), IFS Documentation CY28r1, *Tech. rep.*, ECMWF, Reading, UK, available at: <http://www.ecmwf.int/research/ifsdocs/CY28r1/index.html> (August 2007).
- Elachi, C. (1987), *Introduction to the Physics and Techniques of Remote Sensing*, Wiley Series in Remote Sensing, John Wiley and Sons Inc., New York, Chichester, Brisbane, Toronto, Singapore.
- Fjeldbo, G., and V. Eshleman (1965), The bistatic radar-occultation method for the study of planetary atmospheres, *J. Geophys. Res.*, *70*, 3217–3225.
- Fjeldbo, G., A. Kliore, and V. Eshleman (1971), The neutral atmosphere of Venus as studied with Mariner-V radio occultation experiments, *Astron. J.*, *76*, 123–140.
- Foelsche, U. (1999), Tropospheric water vapour imaging by combination of spaceborne and ground-based GNSS sounding data, Ph.D. thesis, Inst. for Geophysics, Astrophysics, and Meteorology (IGAM)/Institute for Physics, University of Graz, Graz, Austria.
- Foelsche, U., A. Gobiet, A. Loescher, G. Kirchengast, A. Steiner, J. Wickert, and T. Schmidt (2005), The CHAMPCLIM project: An overview, in *Earth Observation with CHAMP: Results from Three Years in Orbit*, edited by C. Reigber, H. Luehr, P. Schwintzer, and J. Wickert, pp. 615–619, Springer Verlag, Berlin, doi: 10.1007/3-540-34121-8_3.
- Fu, Q., C. Johnson, S. Warren, and D. Seidel (2004), Contribution of stratospheric cooling to satellite-inferred tropospheric temperature trends, *Nature*, *429*, 55–58.
- Gleick, P. (1996), Water resources, in *Encyclopedia of Climate and Weather*, edited by S. Schneider, 2 ed., pp. 817–823, Oxford University Press.

- Gobiet, A. (2005), Radio occultation data analysis for climate change monitoring and first climatologies from CHAMP, Ph.D. thesis, Wegener Center for Climate and Global Change and Inst. for Geophysics, Astrophysics, and Meteorology (IGAM)/Institute for Physics, University of Graz, Graz, Austria.
- Gobiet, A., U. Foelsche, A. Steiner, M. Borsche, G. Kirchengast, and J. Wickert (2005), Climatological validation of stratospheric temperatures in ECMWF operational analyses with CHAMP radio occultation data, *Geophys. Res. Lett.*, *32*(L12806), doi:10.1029/2005GL022617.
- Gorbunov, M., A. Gurvich, and L. Kornbluh (2003), Comparative analysis of radiographic methods of processing radio occultation data, *Radio Sci.*, *35*(4), 1025–1034.
- Grody, N. (1983), Severe storm observations with microwave sounding unit, *J. Clim. Appl. Meteor.*, *22*, 609–625.
- Gurvich, A., and T. Krasil'nikova (1990), Navigation satellites for radio sensing of the Earth's atmosphere, *Sov. J. Remote Sensing*, *7*(6), 1124–1131.
- Hajj, G., E. Kursinski, L. Romans, W. Bertinger, and S. Leroy (2002), A technical description of atmospheric sounding by GPS occultation, *J. Atmos. Sol-Terr. Phys.*, *64*, 451–469.
- Hansen, J., et al. (2002), Climate forcings in Goddard Institute for Space Studies SI2000 simulations, *J. Geophys. Res.*, *107*, doi:10.1029/2001JD001143.
- Hartmann, D. (1994), *Global Physical Climatology, International Geophysics Series*, vol. 56, 411 pp., Academic Press, San Diego, New York, Boston, London, Sydney, Tokyo, Toronto.
- Hedin, A. (1991), Extension of the MSIS thermosphere model into the middle and lower atmosphere, *J. Geophys. Res.*, *96*, 1159–1172.
- Hegerl, G., and J. Wallace (2002), Influence of patterns of climate variability on the difference between satellite and surface temperature trends, *J. Climate*, *15*, 2412–2428.
- Hocke, K., K. Igrashi, and T. Tsuda (2003), High-resolution profiling of layered structures in the lower stratosphere by GPS occultation, *Geophys. Res. Lett.*, *30*(8), 1426, doi:10.1029/2002GL016566.
- Hofmann-Wellenhof, B., H. Lichtenegger, and J. Collins (1992), *GPS: Theory and Practice*, Springer, Berlin.
- Houghton, J., Y. Ding, D. Giggs, M. Noguer, P. van der Linden, K. M. X. Dai, and C. Johnson (Eds.) (2001), *Climate Change: The Scientific Basis. Contribution of Working Group 1 to the Third Assessment Report of the Intergovernmental Panel of Climate Change*, 881 pp., Cambridge University Press, Cambridge.

Bibliography

- Jackson, J. (1983), *Klassische Elektrodynamik*, Walter de Gruyter, Berlin, New York.
- Jensen, A., M. Lohmann, H.-H. Benzon, and A. Nielsen (2003), Full spectrum inversion of radio occultation signals, *Radio Sci.*, *38*(3), 1040, doi:10.1029/2002RS002763.
- Jones, P., and A. Moberg (2003), Hemispheric and large-scale surface air temperature variations: An extensive revision and an update to 2001, *J. Climate*, *16*, 206–223.
- Kennedy, J., and W. Nordberg (1967), Circulation features of the stratospheric derived from radiometric temperature measurements with the TIROS- 7 satellite, *J. Atmos. Sci.*, *24*, 711–719.
- Kiehl, J., and K. E. Trenberth (1997), Earth’s annual global mean energy budget, *Bull. Amer. Meteor. Soc.*, *78*, 197–208.
- Kiehl, J., J. Hack, G. Bonan, B. Boville, B. Briegleb, D. Williamson, and P. Rasch (1996), Description of the NCAR Community Climate Model (CCM3), *Tech. rep.*, National Center for Atmospheric Research, Boulder.
- Kirchengast, G., and P. Hoeg (2004), The ACE+ mission: An atmosphere and climate explorer based on GPS, GALILEO and LEO-LEO radio occultation, in *Occultations for probing atmosphere and climate*, edited by G. Kirchengast, U. Foelsche, and A. Steiner, pp. 201–220, Springer.
- Kliore, A., G. Fjeldbo, B. Seidel, D. Sweetman, T. Sesplaukis, P. Woiceshyn, and S. Rasool (1975), The atmosphere of Io from Pioneer-10 radio occultation measurements, *Icarus*, *24*, 407–410.
- König, R., S. Zhu, C. Reigber, K.-H. Neumeyer, H. Meixner, R. Galas, G. Bausiert, and P. Schwintzer (2002), CHAMP rapid orbit determination for GPS atmospheric limb sounding, *Adv. Space Res.*, *30*(2), 289–293.
- Kursinski, E., and G. Hajj (2001), A comparison of water vapor derived from GPS occultations and global weather analyses, *J. Geophys. Res.*, *106*, 1113–1138.
- Kursinski, E., G. Hajj, W. Bertiger, S. Leroy, T. Meehan, L. Romans, J. Schofield, D. McCleese, W. Melbourne, G. Thornton, T. Yunck, J. Eyre, and R. Nagatani (1996), Initial results of radio occultation observations of Earth’s atmosphere using the Global Positioning System, *Science*, *271*, 1107–1110.
- Kursinski, E., G. Hajj, J. Schofield, R. Linfield, and K. Hardy (1997), Observing Earth’s atmosphere with radio occultation measurements using the global positioning system, *J. Geophys. Res.*, *102*, 23,429–23,465.
- Kursinski, E., G. Hajj, S. Leroy, and B. Herman (2000), The GPS RO Technique, *Terr., Atmos. and Oceanic Sci.*, *11*(1), 53–114.

- Lenoir, W. (1968), Microwave spectrum of molecular oxygen in the Mesosphere, *J. Geophys. Res., Space Physics*, *73*, 361–376.
- Liljequist, G., and K. Cihak (1984), *Allgemeine Meteorologie*, vol. 3, Vieweg, Wiesbaden.
- Lindal, G., G. Wood, H. Hotz, D. Sweetman, V. Eshleman, and G. Tyler (1983), The atmosphere of Titan: An analysis of the Voyager-1 radio occultation measurements, *Icarus*, *53*, 348–363.
- Lindal, G., D. Sweetman, and V. Eshleman (1985), The atmosphere of Saturn: An analysis of the Voyager radio occultation measurements, *Astron. J.*, *90*, 1136–1146.
- Malberg, H. (1997), *Meteorologie und Klimatologie: Eine Einführung*, 354 pp., Springer, Berlin, Heidelberg, Germany.
- McIlveen, J. (1998), *Fundamentals of Weather and Climate*, 497 pp., Stanley Thornes Ltd., Cheltenham, Unuited Kingdom.
- Mears, C., M. Schabel, and F. Wentz (2003), A Reanalysis of the MSU Channel 2 Tropospheric Temperature Record (unpublished), *J. Climate*, *16*, 3650–3664.
- Meeks, M., and A. Lilley (1963), The microwave spectrum of oxygen in the Earth’s atmosphere, *J. Geophys. Research*, *68*, 1683–1703.
- NASA/NOAA (2004), NOAA-N, Available at: http://goespoes.gsfc.nasa.gov/poes/spacecraft/noaa_n_booklet.pdf, by National Oceanic and Atmospheric Administration (NOAA) and National Aeronautics and Space Administration (NASA).
- Neu, U. (2005), Widersprüche zwischen Satellitendaten und bodennahen Temperaturmessungen sind weitgehend ausgeräumt, *Climate-Press*, *21*.
- Peixoto, J., and A. Oort (1992), *Physics of climate*, 520 pp., American Institute of Physics, Woodbury, NY.
- Peixoto, J., and A. Oort (1996), The climatology of relative humidity in the atmosphere, *J. Climate*, *9*, 3443–3463.
- Phinney, R., and D. Anderson (1968), On the radio occultation method for studying planetary atmospheres, *J. Geophys. Res.*, *73*, 1819–1827.
- Pirscher, B., U. Foelsche, B. C. Lackner, and G. Kirchengast (2007), Local time influence in single-satellite radio occultation climatologies from Sun-synchronous and non-Sun-synchronous satellites, *J. Geophys. Res.*, *112*, D11,119, doi:10.1029/2006JD007934.
- Reigber, C., P. Schwintzer, and A. Kohlhasse (1995), CHAMP - A challenging micro-satellite payload for geophysical research and application, *Feasibility study for DARA final report*, GFZ, Potsdam, Potsdam, Germany.

Bibliography

- Salby, M. (1995), *Fundamentals of Atmospheric Physics*, Academic Press Inc, USA.
- Santer, B., T. Wigles, G. Meehl, M. Wehner, C. Mears, M. Schabel, F. Wentz, C. Ammann, J. Arblaster, T. Bettge, W. Washington, K. Taylor, J. Boyle, W. Brüggemann, and C. Doutriaux (2003), , *Science*, *301*, 1047–1049.
- Smith, E., and S. Weintraub (1953), The constants in the equation for atmospheric refractive index at radio frequencies, *Proceedings of the I.R.E*, *41*, 1035–1037.
- Solomon, S., D. Qin, M. Manning, Z. Chen, M. Marquis, K. B. Averyt, M. Tignor, and H. L. Miller (Eds.) (2007), *Climate Change 2007: The Physical Science Basis. Contribution of Working Group I to the Fourth Assessment Report of the Intergovernmental Panel on Climate Change*, 996 pp., Cambridge University Press, Cambridge, United Kingdom and New York, NY, USA.
- Spencer, R., and J. Christy (1992), Precision and Radiosonde Validation of Satellite Grid-point Temperature Anomalies. Part 1: MSU Channel 2, *J. Climate*, *5*, 847–857.
- Spencer, R., J. Christy, and N. Grody (1990), Global Atmospheric Temperature Monitoring with Satellite Microwave Measurements: Method and Results 1979-84, *J. Climate*, *3*, 1111–1128.
- Spencer, R. W., J. R. Christy, W. D. Braswell, and W. B. Norris (2006), Estimation of Tropospheric Temperature Trends from MSU Channels 2 and 4, *J. Atmos. Oceanic Technol.*, *23*(3), 417–423, 10.1175/JTECH1840.1.
- Spilker, J. (1980), Signal structure and performance characteristics, in *Global Positioning System: Papers published in Navigation*, vol. 1, edited by P. Janiczek, pp. 29–54, Institute of Navigation.
- Steiner, A. (1998), High resolution sounding of key climate variables using the radio occultation technique, Ph.D. thesis, Inst. for Geophysics, Astrophysics, and Meteorology (IGAM)/Institute for Physics, University of Graz, Graz, Austria.
- Steiner, A., G. Kirchengast, M. Borsche, U. Foelsche, and T. Schöngäßner (2007), A multi-year comparison of lower stratospheric temperatures from CHAMP radio occultation data with MSU/AMSU records, *J. Geophys. Res.*, *112*, D22,110, doi:10.1029/2006JD008283.
- Syndergaard, S. (1998), Modeling the impact of Earth’s oblateness on the retrieval of temperature and pressure profiles from limb sounding, *J. Atmos. Sol-Terr. Phys.*, *60*(2), 171–180.
- Syndergaard, S. (1999), Retrieval Analysis and Methodologies in Atmospheric Limb Sounding Using the GNSS Radio Occultation Technique, Ph.D. thesis, Danish Meteorological Institute, Copenhagen, Denmark.

- Thorne, P., D. Parker, S. Tett, P. Jones, M. McCarthy, H. Coleman, and P. Brohan (2005), Revisiting radiosonde upper air temperatures from 1958 to 2002, *J. Geophys. Res.*, *110*(D18105), doi:10.1029/2004JD005753.
- Untch, A., M. Miller, M. Hortal, R. Buizza, and P. Janssen (2006), Towards a global meso-scale model: The high-resolution system T799L91 and T399L62 EPS, *Newsletter*, *108*.
- Vinnikov, K., and N. Grody (2003), Global warming trend of mean tropospheric temperature observed by satellites, *Science*, *302*, 269–272.
- Vorob'ev, V., and T. Krasil'nikova (1994), Estimation of the accuracy of the atmospheric refractive index recovery from Doppler shift measurements at frequencies used in the NAVSTAR system, *Phys. Atmos. Ocean*, *29*, 602–609.
- Ware, R., M. Exner, D. Feng, M. Gorbunov, K. Hardy, B. Herman, Y.-H. Kuo, T. Meehan, W. Melbourne, C. Rocke, W. Schreiner, S. Sokolovskiy, F. Solheim, X. Zou, R. Anthes, S. Businger, and K. Trenberth (1996), GPS sounding of the atmosphere from low Earth orbit: Preliminary results, *Bull. Am. Meteorol. Soc.*, *77*, 19–40.
- Warnek, P. (1988), *Chemistry of the Natural Atmosphere*, 757 pp., Academic Press.
- Waters, J. (1973), Ground-based measurement of millimetre-wavelength emission by upper stratospheric O₂, *Nature*, *242*, 506–508.
- Wentz, F., and M. Schabel (1998), Effects of satellite orbital decay on MSU lower tropospheric temperature trends, *Nature*, *394*, 661–664.
- Wickert, J. (2002), Das CHAMP Radiookkultationsexperiment: Algorithmen, Prozessierungssystem und erste Ergebnisse, Ph.D. thesis, GFZ Potsdam, Potsdam, Germany.
- Wickert, J., T. Schmidt, G. Beyerle, R. König, C. Reigber, and N. Jakowski (2004), The radio occultation experiment aboard CHAMP: Operational data analysis and validation of vertical atmospheric profiles, *J. Meteorol. Soc. Japan*, *82*, 381–395.
- Wickert, J., G. Beyerle, R. König, S. Heise, L. Grunwaldt, G. Michalak, C. Reigber, and T. Schmidt (2005), GPS radio occultation with CHAMP and GRACE: A first look at a new and promising satellite configuration for global atmospheric sounding, *Ann. Geophys.*, *23*, 653–658.

Abstract:

Since 1979 weather satellites are used to observe the atmosphere. As part of their observables they measure the atmospheric microwave radiation at several frequencies with a Microwave Sounding Unit (MSU), which is the basis for retrieving global homogeneously distributed temperature information in several atmospheric layers. But different climate trends resulted from different analysis groups, due to difficulties of calibration, moving satellite orbit planes and multi-satellite merging procedures. In this context, the Global Positioning System (GPS) radio occultation (RO) technique provides a good alternative because of its high-resolution vertical temperature profiles and the long-term stable calibration from atomic clocks. In this work the MSU-based temperature observations are validated against the GPS RO observations of the CHALLENGING Minisatellite Payload (CHAMP) satellite between September 2001 and December 2005.

In the troposphere in moist regions, the CHAMP RO profiles were complemented by profiles from operational analyses of the European Centre for Medium-Range Weather Forecasts (ECMWF). The RO profiles were weighted to synthetic-MSU RO records, with global MSU weighting functions, and monthly-mean zonal-mean records were compared to MSU data from University of Alabama at Huntsville (UAH) and Remote Sensing Systems (RSS). The work introduces both the MSU and RO techniques and describes the inter-comparison results in detail.

Zusammenfassung:

Seit 1979 werden Wettersatelliten zur Beobachtung der Atmosphäre verwendet. Teil ihrer Daten sind Strahlungsmessungen in mehreren Mikrowellen-Frequenzkanälen mit einer Microwave Sounding Unit (MSU), woraus sich die Temperatur mehrerer atmosphärischer Schichten ableiten lässt. Jedoch ist die langzeitliche Datenkalibrierung sehr schwierig, weshalb verschiedene Forschergruppen zu unterschiedlichen Klimatrends gelangten. In diesem Rahmen stellt die Radio-Okkultationsmethode auf Basis des Global Positioning System (GPS RO) wegen ihrer vertikal fein aufgelösten Temperaturprofile und ihrer Langzeitstabilität eine interessante Alternative dar. In dieser Arbeit werden MSU-basierte Temperaturmessungen mit GPS RO Temperaturmessungen des Satelliten CHAMP für den Zeitraum von September 2001 bis Dezember 2005 validiert.

In der feuchten Troposphäre wurden die CHAMP RO Profile mit Profilen aus operationellen Atmosphärenanalysen des Europäischen Zentrums für Mittelfrist-Wettervorhersage (EZMW) ergänzt. Es wurden mit Hilfe von globalen MSU Gewichtungsfunktionen synthetische MSU Zeitreihen aus den RO Daten erstellt und mit den MSU Zeitreihen der University of Alabama at Huntsville (UAH) und von Remote Sensing Systems (RSS) verglichen. Die Arbeit gibt eine Einführung in die MSU und RO Beobachtungstechniken und beschreibt die Validierungsergebnisse im Detail.